Universität Zürich
Physik-Institut
Winterthurerstr. 190
8057 Zurich

HS 2008

Master Thesis

A fast online and triggerless signal reconstruction based on cross-correlation

Author: Arno Gadola, agadola@physik.uzh.ch

Prof. Dr. Ulrich Straumann, strauman@physik.uzh.ch
Dr. Achim Vollhardt, avollhar@physik.uzh.ch

Winter 2008

"I do not think there is any thrill that can go through the human heart like that felt by the inventor as he sees some creation of the brain unfolding to success... Such emotions make a man forget food, sleep, friends, love, everything."
Nikola Tesla.

Dedicated to my parents.

Abstract

This thesis examines as a case study for the Cherenkov telescope array CTA, the possibility of a fast triggerless and online reconstruction method based on the second derivative of the cross-correlation with a template function for the reconstruction of shower signals. The algorithm was tested on measured and emulated data samples. The measurements were gained with a test setup consisting of a light pulser and a Geiger mode Avalanche Photo Diode (GAPD). The emulated samples were produced with realistic parameters for night sky background frequency (40 - 3000 MHz), shower pulse amplitudes (1 - 100 photons) and ADC values (1 - 4 ns sampling time and 8, 10, 11, 12 bits resolution). The performance of the algorithm is shown by its reconstruction efficiency, its noise rate and the amplitude and time resolution.

Contents

1 Introduction

An important issue for detectors that measure very high particle flows or other non periodic high-rate processes, is the error caused by the pile up of detected particles. These piled-up events can cause a wrong estimation of energy and particle numbers. Most present detectors make use of triggering systems, which set a threshold on the signal amplitude. These systems do not analyze the shape of the incoming signal and are therefore not able to discriminate pile up.
Due to significant improvements in electronics fast processing at low power consumption and low prices are achievable, it comes feasible now to study triggerless readout systems based on an online signal shape analysis. Such a system consists of a soft and a hardware part. This thesis will cover mainly the software part.

This thesis is realized in the framework of the astroparticle project CTA, which aims the detection of high energetic gamma-rays with a ground-based Cherenkov telescope array. A new type of photon detector, the Geiger mode Avalanche Photo Diode (GAPD), is being considered for the telescope camera.
A test setup with a photon source and a GAPD was assembled to gain first experiences with the GAPD and to collect detector signals. For the signal analysis, the cross-correlation and other methods, which were not further investigated, were studied and tested on these measured GAPD signals. To be independent of the measurements, a test signal generator (Monte Carlo emulation with realistic parameters that are expected in the application of CTA) was implemented in the same environment as the reconstruction algorithm (MATLAB software). The reconstruction algorithm was tuned on its reconstruction power with the analysis of the generated test signals. It turned out, that the cross-correlation itself would not lead to suitable results for piled-up pulses with very small differences in time in the test signals. Therefore the second derivative of the cross-correlation was introduced, which let to very good results in the reconstruction.

This thesis is organized as follows:
A short introduction into gamma-ray astronomy is given in chapter 2. Gamma-rays and their sources are described and a brief introduction in the detection of gamma-rays is given. Chapter 3 describes the operation principal of the GAPD and the test setup to work with them. Measurements with the test setup are also presented in this chapter. The chapter 4 is dedicated to the reconstruction algorithm, the core of this thesis. After a definition of the cross-correlation function and its behavior, the code of the algorithm is presented and discussed in detail. Finally, in chapter 5, the main results and the quality of the reconstruction algorithm like efficiency, noise rate and resolution are presented and discussed in detail, followed by a conclusion in chapter 6. In the appendix A, a GAPD prototype camera is discussed. The most important figures of the reconstruction are shown in appendix B.

2 Gamma-ray astronomy

Experimental gamma-ray astronomy is a rather young research field. It began in the 1960s with the first observations of extraterrestrial gamma-rays and developed to a very interesting field for both, astronomers and particle physicists. For a common understanding, a proper definition of gamma-rays is necessary followed by a short introduction into gamma-ray sources and the imaging Cherenkov detection technique.

2.1 Definition of gamma rays

The spectrum of electromagnetic radiation which covers about 22 orders of magnitude is probably the largest spectrum known. Astronomy explores a huge part of this spectrum with space and ground-based telescopes. For ground based telescopes, the detection environment is mainly determined by the transparency of the atmosphere shown in figure 2.1. A very interesting part of the spectrum is the gamma-ray part which will be partially investigated with the proposed ground-based Cherenkov Telescope Array (CTA). Gamma-rays should thereby not be confused with the generic term cosmic rays which include the gamma-rays but also particles like high energy protons, heavier nuclei, electrons and positrons.
The term 'gamma-rays' is a generic one and is used to describe photons of energies from 100 keV (10^5 eV) to $>$ 100 EeV (10^{20} eV). The most popular range from 30 MeV to 100 TeV is divided into further sub-bands which are defined somewhat arbitrarily in this research field. Here they shall be defined by their interaction phenomena and by the techniques of detection rather by the physics of their production. Table 2.1 lists the different energy-bands.
Mainly two types of interaction phenomena are dominant, the inverse Compton process which is dominant below 30 MeV and is studied with Compton telescopes and pair-production. The electron pair of a HE gamma-ray is identified in balloon or satellite-borne telescopes and the VHE gamma-ray electron pair produced in the earth's atmosphere which results in an electromagnetic cascade (Cherenkov radiation) is identified by ground-based imaging atmospheric Cherenkov telescopes (IACT). Further information about IACTs and gamma-ray astronomy can be found in [9], [1] or on the CTA homepage [2].

Band	Low/Medium	High	Very High	Ultra High
Shorthand	LE/ME	HE	VHE	UHE
Range	0.1-30 MeV	30 MeV-100 GeV	100 GeV-100 TeV	$>$ 100 TeV
Typical energy	keV-MeV	MeV-GeV	TeV	PeV-EeV
Environment	Space	Space	Ground-based	Ground-based

Table 2.1: Definition of gamma-ray bands after T.C. Weekes [9].

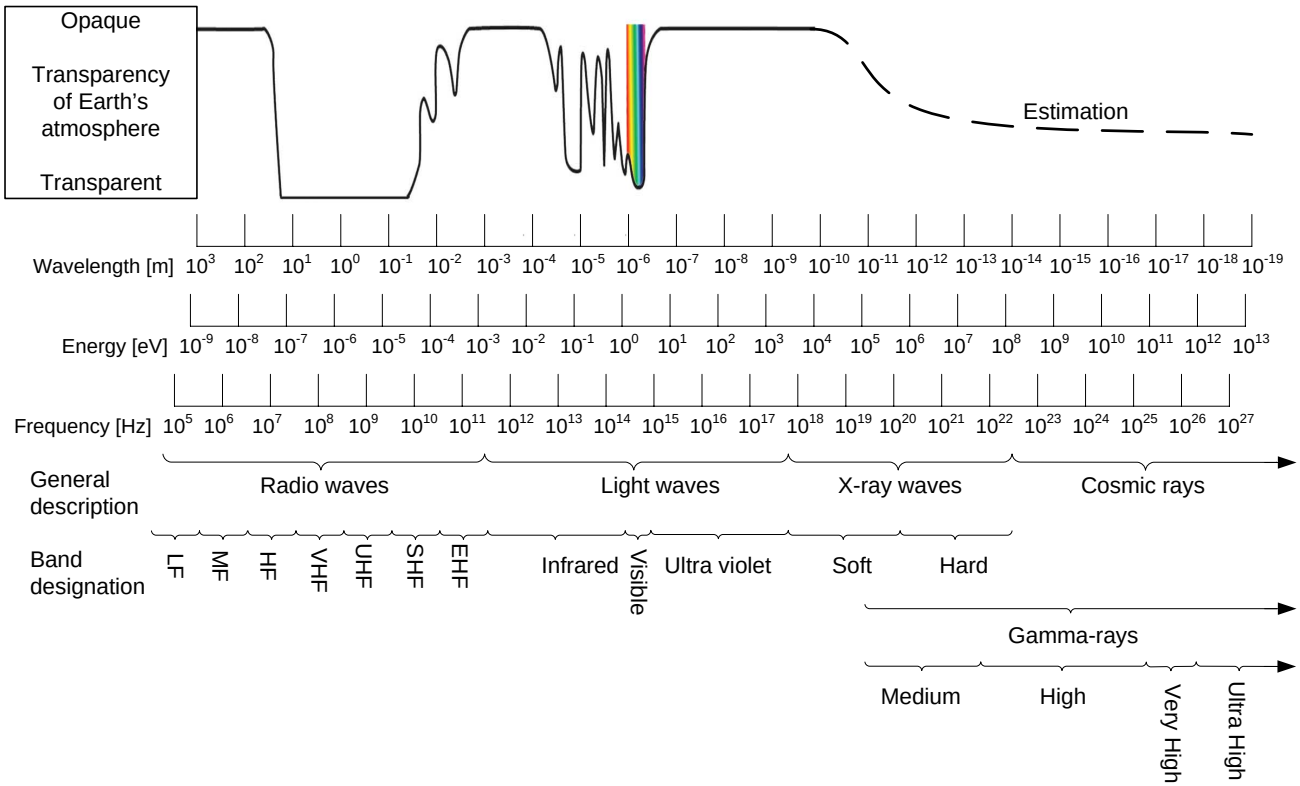

Figure 2.1: Electromagnetic spectrum. The transparency graph shows an approximative distribution.

2.2 Gamma ray sources

Because gamma-rays with energies beyond GeV cannot be generated thermally by emission from hot celestial objects (no such hot objects apart from the Big Bang are known) there need to be other production mechanisms. Basically they are: inverse Compton scattering where low energy photons gain energy by interaction with relativistic electrons ($e^{\pm}\gamma \rightarrow e^{\pm}\gamma$), electron-positron production in photon-photon interactions, pair cascades, synchrotron emission, pion production in proton-proton and proton-photon reactions ($\pi^0 \rightarrow \gamma\gamma$), decays of heavy particles such as dark matter particles. In this sense one probes the non-thermal universe with HE and VHE gamma-rays.

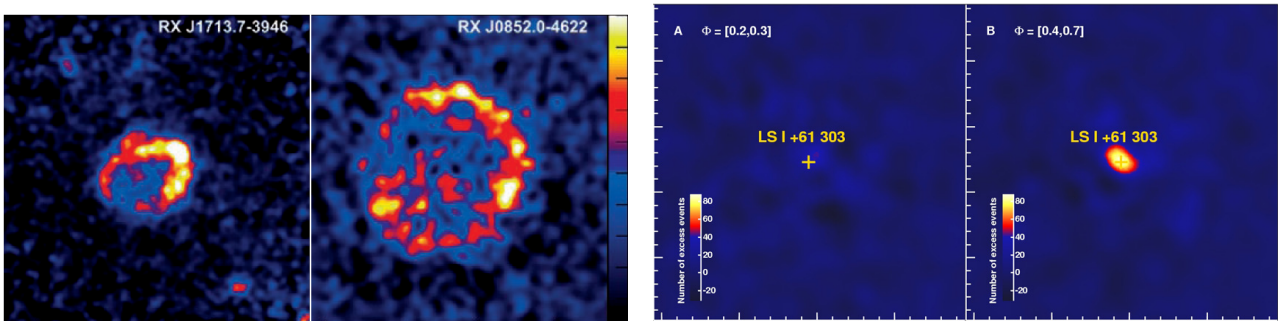

(a) (b)

Figure 2.2: (a) TeV images of shock fronts in supernova, revealing cosmic acceleration of energetic particles [1]. (b) Variable TeV signal from the x-ray binary LSI +61 303 [1].

The following galactic and extra-galactic objects have been established or suggested as possible gamma ray sources (for more details see [1], [7]):

- Supernova remnants (SNRs)
  A supernova is the explosion of a massive star (mass of 8 to 150 solar masses) at the end of its life. Cosmic-rays are accelerated in the supernova explosion shocks (see e.g. fig. 2.2 (a)) which are non thermal processes. The gamma-ray energies reach well beyond 10^{13} eV.
- Pulsars and associated nebulae
  Pulsars are rotating neutron stars with an intense magnetic field. The pulsar's magnetosphere is known to act as an efficient cosmic accelerator with gamma-ray emission in the range of 10 to 100 GeV.
  Pulsar wind nebulae are synchrotron nebulae powered by the relativistic winds of energetic pulsars. Their VHE gamma-ray emissions originate most probably from electrons accelerated in the shock formed by the interaction of the pulsar wind with the supernova ejecta. The most famous pulsar wind nebula is the Crab Nebula (fig. 2.3) which, due to its strong and steady emission of gamma-rays, is used as calibration candle for almost all VHE gamma-ray detectors.
- Binary systems
  A binary system contains a compact object like a neutron star or a black hole orbiting a massive star. Such objects emit mostly VHE gamma-rays (see e.g. fig. 2.2 (b)).
- The Galactic Center
  The center of our galaxy hosts the nearest supermassive black hole (mass of 3.6 solar masses), as well as a variety of other objects likely to generate high energy radiation, including hypothetical dark matter particles which may pair-annihilate and produce gamma-rays.
- Active galactic nuclei (AGNs)
  An AGN is a galaxy with a super massive black hole at the core. AGNs are known to produce outflows which are strong sources of high energy gamma-rays. Other possible sources of gamma-rays are synchrotron emission from populations of ultra-relativistic electrons and inverse Compton emission from soft photon scattering.
- Gamma ray bursts (GRBs)
  GRBs are still a not completely resolved phenomenon. Their pulses are extremely intensive and have a duration of about 0.1 seconds to several minutes. They are known as the most luminous electromagnetic events occurring in the universe since the Big Bang and they all originate from outside our galaxy (as known so far). Investigation of gamma-rays coming from GRBs would help to establish a reliable model for GRBs.
- Dark matter
  Dark matter particles accumulate in, and cause, wells in gravitational potential, and with high enough density they are predicted to have annihilation rates resulting in detectable fluxes of high energy gamma-rays.

For further details and evidences for some of the effects in the different sources see e.g. [8].

2.3 Detection of gamma-rays

The first significant gamma-ray emission from our galaxy was detected in 1967 by the OSO-3 satellite. OSO-3 detected 621 events attributable to cosmic gamma-rays. The real breakthrough was achieved in 1989 when the Whipple collaboration discovered TeV gamma-rays from the Crab Nebula (fig. 2.3) with a ground-based Cherenkov telescope using the imaging atmospheric Cherenkov technique that pioneered almost all ground-based gamma-ray telescopes that are used nowadays. Gamma-ray astronomy observations are limited by non-gamma-ray backgrounds at lower energies and by the small number of photons at higher energies (e.g. at energies of 100 MeV the strongest source, the Vela pulsar, gives a flux of only one photon per minute in telescopes). Therefore larger detector areas and a better background suppression are essential for progress in this research field. The proposed project CTA (section 2.3.2) will be a big step forward in both directions.

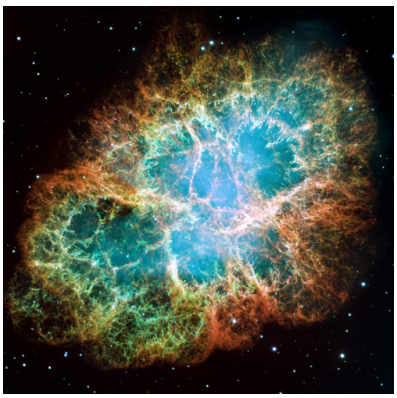

Figure 2.3: The Crab Nebula is used as calibration candle in gamma-ray astrophysics.

2.3.1 The imaging atmospheric Cherenkov technique

Very low fluxes for high energy photons require large detection areas, which cannot be provided by space-based telescopes. Fortunately such high energy photons produce extensive showers of secondary particles in the earth's atmosphere, which can be detected with ground-based telescopes.

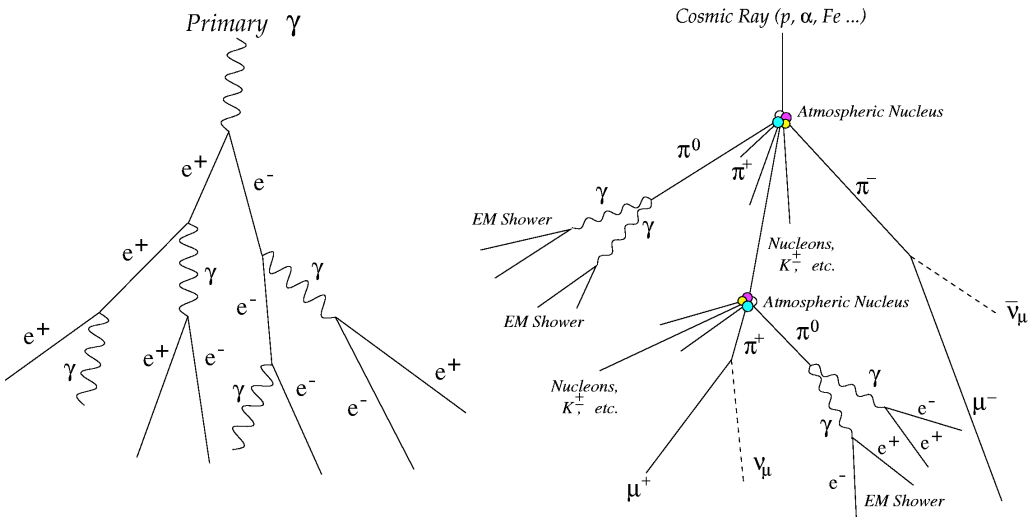

Figure 2.4: Electromagnetic shower (left) generated by an incident photon. Hadronic shower (right) produced by cosmic rays like protons, heavier nuclei, electrons, positrons.

A photon entering the atmosphere produces in the core field of gas nuclei an electron-positron pair (fig. 2.4) with $\beta \cong 1$. This means, that the $e^{\pm}$ pair travels faster than the speed of light in the atmosphere and thus sends out Cherenkov light (around 300 to 700 nm wavelength). The electrons and positrons produce further high energetic photons through bremsstrahlung, which again

produce $e^{\pm}$ pairs in the core field of gas nuclei. This cascade develops downwards to the earth until the generated bremsstrahlung photons have not enough energy to produce a further $e^{\pm}$ pair. The Cherenkov photons illuminate at ground level an area of typically 50'000 m^2 (approximately 250 m diameter) with a density of about 8 γ/m^2 for 100 GeV and 130 γ/m^2 for 1 TeV gamma-rays.
The Cherenkov light pulse emitted lasts for about 3-10 ns depending on the energy of the incident gamma-ray (a hadron induced shower lasts a bit longer). The Cherenkov emission can be detected by optical telescopes which allows then a reconstruction of the trajectory and thus a localization of the source of the gamma-ray. Building a telescope of 250 m diameter would be impossible for engineering and financial reasons so that smaller telescopes with about 10-17 m diameters are constructed in arrays. Such telescopes are e.g. MAGIC [3], situated at the Roque de los Muchachos site on the Canary island of La Palma (fig. 2.5) and H.E.S.S. [4], located in Namibia near the Gamsberg mountain, both 'stereoscopic' telescopes, CANGAROO ([5], South Australia), VERITAS ([6], Arizona, USA) and the planned CTA. These telescopes are so sensitive that they can detect the Crab Nebula in a few minutes of integration time.

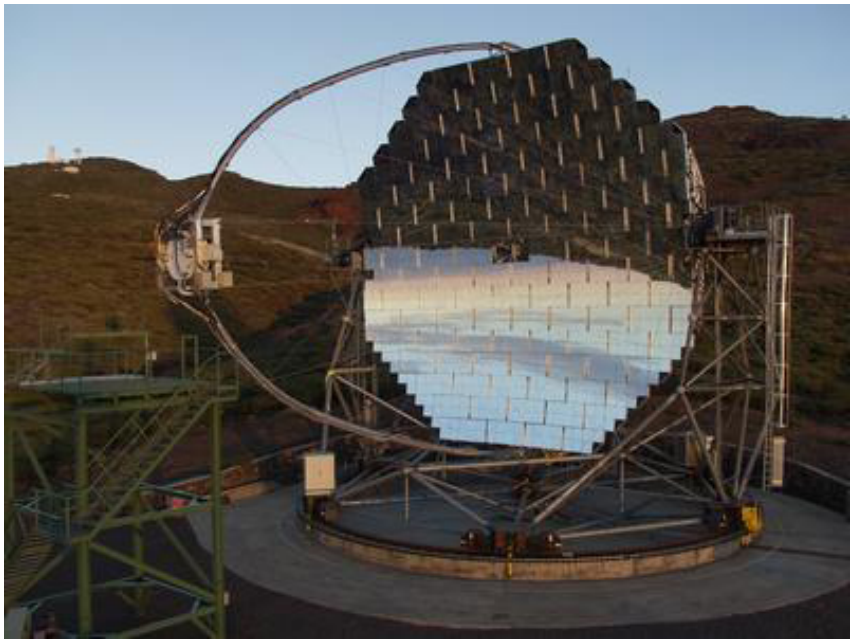

Figure 2.5: The MAGIC telescope at the Roque de los Muchachos on the Canary island of La Palma.

2.3.2 The CTA project

The CTA (**C**herenkov **T**elescope **A**rray) project will be a next-generation imaging atmospheric Cherenkov telescope built by a worldwide community. It merges the experience and techniques of the two current instruments H.E.S.S. (array of four smaller telescopes with 7 m diameter) and MAGIC (two big telescopes with 17 m diameter). It will consist of a southern and northern array of about several tens of small and a few big telescopes. The focus is on the High Energy (HE) band from 40 MeV to 100 GeV and the Very High Energy (VHE) band from 100 GeV to 100 TeV. CTA will provide increased sensitivity by one order of magnitude (fig. 2.6), as well as an expansion of the detectable gamma-ray energy range towards both lower and higher energies. Improvements in angular resolution

will reveal finer details in the sources at smaller detection rates enabling research on very short time scales.

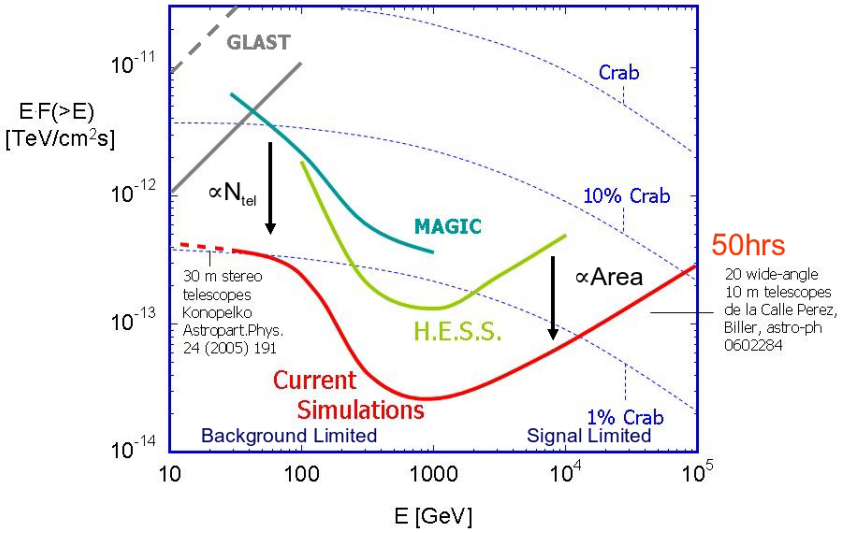

Figure 2.6: Sensitivity aimed with CTA (red curve), compared with the existing experiments and with the flux of the Crab Nebula (standard candle for Very High Energy Gamma-Ray Astronomy, 50 hours observation/integration time). The exact value will depend on the final layout of the system [1].

3 GAPDs and hardware test setup

A good time and position resolution of the telescope's camera of about 2-5 ns and 0.05° (CTA goal 0.038°) is needed for the determination of the gamma-ray's origin, its energy and for discriminating gamma-ray induced showers from muon and hadron induced showers. Due to the very low fluxes a high photon detection efficiency (quantum efficiency QE) over the wavelength range of 300 to 600 nm is mandatory. With present photomultiplier tubes a QE of about 25 to 35% is achivable whereas new semiconductor devices have QEs upto 60%.
The relatively new Geiger Mode Avalanche Photo Diode (GAPD) could be a good candidate to replace or complement photomultipliers in Cherenkov telescope cameras due to their much better quantum efficiency, the low bias voltage (<100 V) and their output with constant identical pulse shape. The later discussed reconstruction algorithm bases on the output signal shape of such GAPDs. First the GAPD itself and then a test setup for signal taking shall be discussed.
For all mentioned voltages the absolute values are taken for simplicity (e.g. $V_{bias} \geq 0$).

3.1 Geiger Mode Avalanche Photo Diode (GAPD)

The GAPD is a reversed biased pn junction with a bias voltage slightly bigger than the breakdown voltage ($V_{bias} > V_{BR}$, see fig. 3.1). The applied voltage generates across the pn junction a strong electric field which depletes the so called avalanche layer. When a photon traverses the fully depleted pn junction it can excite an electron bringing it into the conduction band and leave a hole in the valence band - an electron/hole pair is produced (fig. 3.2 a). The electron and the hole are accelerated by the high electric field and produce further electron/hole pairs (fig. 3.2 b), which are also accelerated and so on. Thus an avalanche of electron/hole pairs is produced which leads to a measurable signal. This phenomenon is known as "Geiger discharge" (in normal mode $V_{bias} < V_{BR}$, no avalanche is produced). The avalanche is stopped by a so called quenching resistor R_Q (fig. 3.2) which reduces the bias voltage over the diode and thus the electric field and the gain, respectively. In addition, there are also discharges which are not desired. These sources are due to fluctuations of non-photogenerated carriers due to thermal excitation triggering a discharge (dark count). Secondary sources are carriers trapped during a discharge and released after the recovery time (afterpulsing) and carriers generated by photons emitted during the discharge

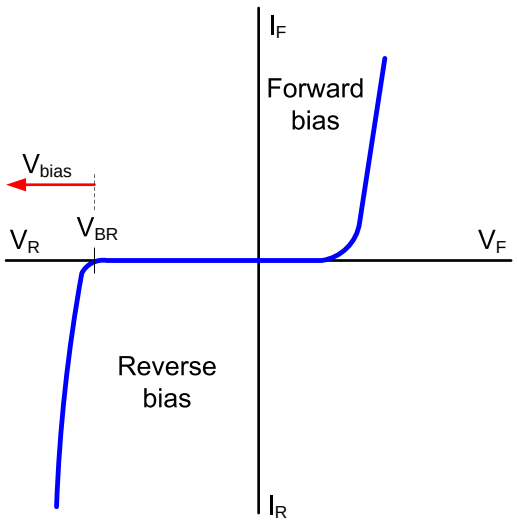

Figure 3.1: Characteristic curve of a general pn junction (diode). A normal diode works in the first quadrant with a positive bias voltage whereas a Z-diode and a GAPD in the third quadrant with a reverse bias voltage lie. The bias voltage of a GAPD is normally about $V_{bias} \approx V_{BR} + 2..3$ V

of a neighboring GAPD (optical crosstalk), [12]. Information on the reduction of these noise sources can be found in [17]. Next, a few benchmarking data of GAPD modules, which consist of several segmented pn junctions, shall be discussed before having a closer look on the functionality of a GAPD.

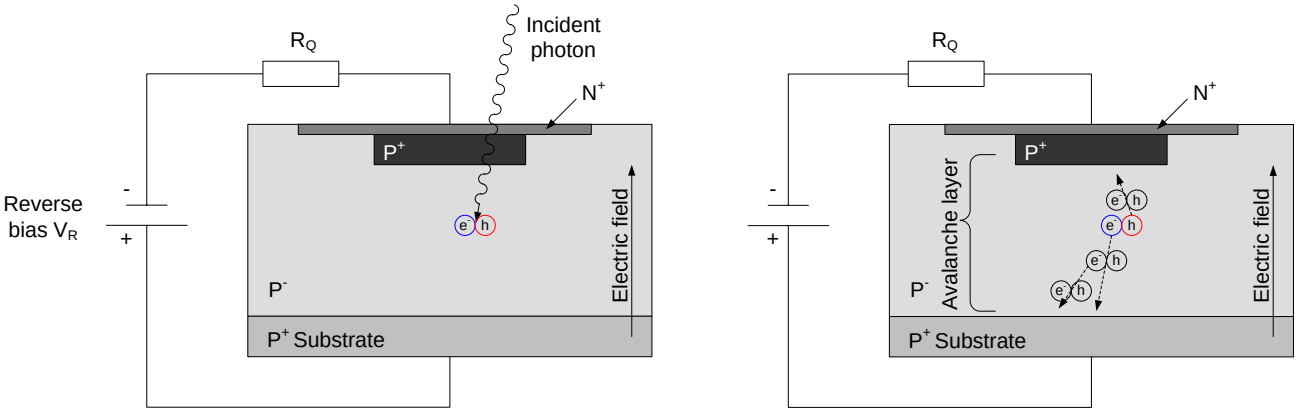

Figure 3.2: (a): Electron/hole pair (e/h) is injected into the avalanche layer by an incident photon. (b): The electron is accelerated downwards by means of the electric field whereas the hole accelerates upwards. On their way they generate new e/h pairs by ionization. The newly generated carriers are also accelerated and produce further e/h pairs. This process continuous and generates an avalanche. The gain is proportional to the applied reverse bias.

Table 3.1 characterizes a few advantages and disadvantages of GAPDs and of the well established photomultiplier tube (PMT).

GAPD	**PMT**
+ Solid state technology: robust, compact, mechanically rugged	+ High internal gain of $10^6 \div 10^7$
+ High quantum efficiency ($\approx$ 60%)	+ Very good time resolution: hundreds of ps
+ High internal gain of $10^5 \div 10^6$	+ Collection efficiency: 70$\div$90%
+ Large standardized output signal	+ Large dynamic range: 10^6
+ High sensitivity for single photons	+ Large standardized output signal
+ Excellent timing even for single photo electrons ($<<$ 1 ns)	
+ Good temperature stability	
+ Devices operate in general $<$ 100 V	
+ **GAPD Module**: 'Analog' device (two incident photons create a doubled signal amplitude)	
- **Single GAPD**: Binary device (one knows there was at least one electron/hole initiating the breakdown but not how many of them)	- High supply voltage: few kV
	- Vacuum tube technology
	- Small quantum efficiency (25 - 35%)
	- Affected by magnetic fields

Table 3.1: The table shows the most important advantages and disadvantages of GAPDs and PMTs.

One of the biggest advantages of GAPDs is their huge internal gain at a comparably small operating voltage. The supply, distribution and monitoring of voltages smaller than 100V is much easier. A big disadvantage is the small size of the active area of GAPD arrays (few mm^2). For large detection areas, this leads to a huge number of readout channels and thus to an enormous data volume. Hence a combination of several GAPD arrays with one output is necessary. The development of GAPD arrays with larger active area is in progress.

3.1.1 GAPD functionality

The equivalent circuit diagram (fig. 3.4) describes quite well the behavior of a single GAPD. In the initial state, the switch is in the OFF position and the capacitor C_D is fully loaded to the applied bias voltage. No current flows through the quenching resistor R_Q. If an incident photon initiates an electron/hole pair avalanche, the switch takes the ON position so that C_D discharges through R_S down to the breakdown voltage $V_{BR} < V_{bias}$ with a time constant $t_D = R_S C_D$. Note that initially the current is limited by the build up of the avalanche process (some hundreds of ps). This decreasing of the voltage accross C_D leads to a current through and therefore to an increasing voltage drop over the quenching resistor R_Q. The current tends to the asymptotic value of $i_a = (V_{bias} - V_{BR})/(R_Q + R_S)$. In this final state the current is so low that a statistical fluctuation brings the instantaneous number of carriers flowing through the high-field region to zero, quenching the avalanche [12]. As the avalanche process is terminated, the switch takes again the OFF position. The capacitor C_D gets recharged from V_{BR} to V_{bias} with a time constant of $t_D = R_Q C_D$ and the GAPD becomes ready to detect the arrival of a new photon. The number of carriers produced during an avalanche discharge is given by equation 3.1 where q is the electron charge ($1.6 \cdot 10^{-19} C$). Since every single GAPD in an array reacts independently in the described way, the output signal of a GAPD array for n incident photons will be n times $N_{carriers}$ (see fig. 3.3).

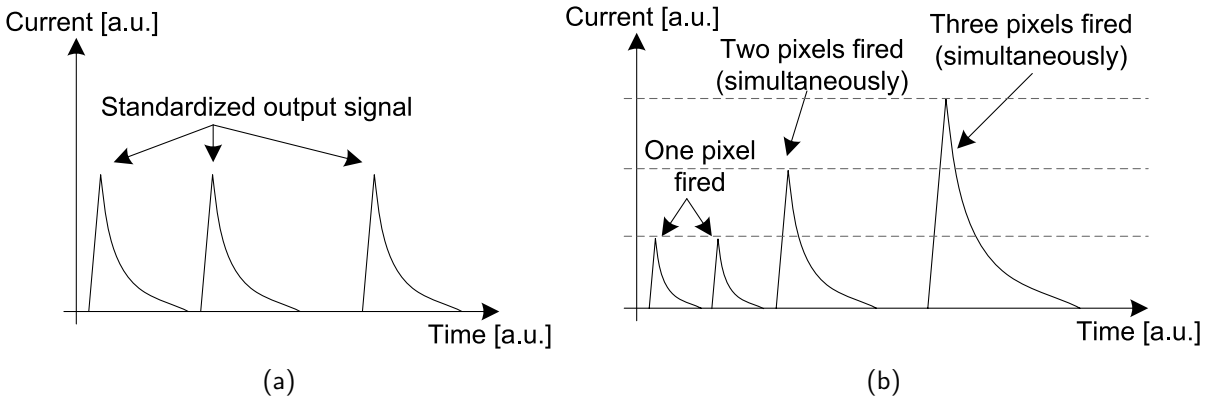

Figure 3.3: (a): Output of a single GAPD (microcell). The amplitude has a standardized shape. (b): Output of an array of GAPDs. The amplitude corresponds to the number of incident photons and is the sum of all signals form each single GAPD, respectively. Therefore the signal shape scales with the number of simultaneously incident photons.

$$N_{carriers} = \frac{1}{q}(V_{bias} - V_{BR}) \cdot C_D \tag{3.1}$$

The "quenching" capacitance C_Q comes from the vaporization of the quenching resistor on the silicon dioxide layer (see fig. 3.5). Its impact on the signal shape is characterized through

$$\tau_{fast} = R_S \cdot (C_D + C_Q) \tag{3.2}$$

$$\tau_{slow} = R_Q \cdot (C_D + C_Q) \tag{3.3}$$

where τ_{fast} describes the very fast leading edge (hundreds of ps), determined both by the avalanche spreading and by the discharge of the diode capacitance C_D through the serial resistance R_S, and τ_{slow} describes the slow exponential decay (recharging of C_D). R_S includes both the resistance of the neutral regions of the semiconductor and the space-charge of the avalanche junction. C_D can be estimated from the geometry of the microcell applying the parallel-plate capacitance equation. For a typical device area of 100x100 μm^2 and an epitaxial layer (this layer is fully depleted at operation voltage, see fig. 3.5 (a)) with a thickness of approximately 4 μm we get for C_D a capacitance of (dielectric constant for undoped and doped silicon: $\epsilon_r = 11.68$)

$$C_D = \epsilon_0 \cdot \epsilon_r \cdot \frac{A}{d} = 8.85 \cdot 10^{-12} \frac{As}{Vm} \cdot 11.68 \cdot \frac{100 \cdot 100 \cdot 10^{-6} m^2}{4 \cdot 10^{-6} m} \approx 260\ fF \tag{3.4}$$

This corresponds to a time constant of about $t_D = R_Q C_D = 34\ ns$ [1]. Typical values for single GAPDs are listed in table 3.2.

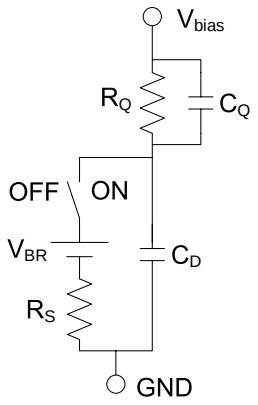

Figure 3.4: Equivalent circuit diagram of a single GAPD [12].

To increase the active surface of a GAPD and to reduce the number of output channels, several hundred or thousand single GAPDs are connected in parallel to a GAPD array (see fig. 3.5 (b) and 3.6). For the measurements presented in this thesis a Hamamatsu GAPD array with an active surface of about 3x3 mm^2 and 900 single GAPDs is used (MPPC type: S10362-33-100C, see datasheet [17] for more details).
Figure 3.7 shows typical curves for a Hamamatsu GAPD array at constant temperature. (a) shows the gain behavior in a small range around the operation voltage. It is linear in the range from 70.1 to 71.9 V and changes from 1.7$\cdot 10^5$ to 3.7 $\cdot 10^5$. The photon detection efficiency (PDE) in figure (b) shows the spectral limits of such a GAPD array. New measurements have shown that the actual PDE for the GAPD array used is shifted towards a 440 nm peak and that the lower cutoff is at about 300 nm.
In the following chapters the term GAPD will always denote GAPD arrays.

R_Q	130 kΩ
R_S [1]	few Ω ÷ 1 kΩ
C_Q [2]	0 nF
C_D	300 fF
V_{bias}	70 V
V_{BR}	V_{bias} - (1÷2) V
t_{rise}	1÷2 ns
t_{fall}	40÷70 ns

Table 3.2: [1] small values are favored by some papers and Dieter Renker whereas other papers tend to high values. [2] Hamamatsu places the quenching resistor aside of the active area to reduce its capacitance to zero and to increase the active area. All values are approximate values.

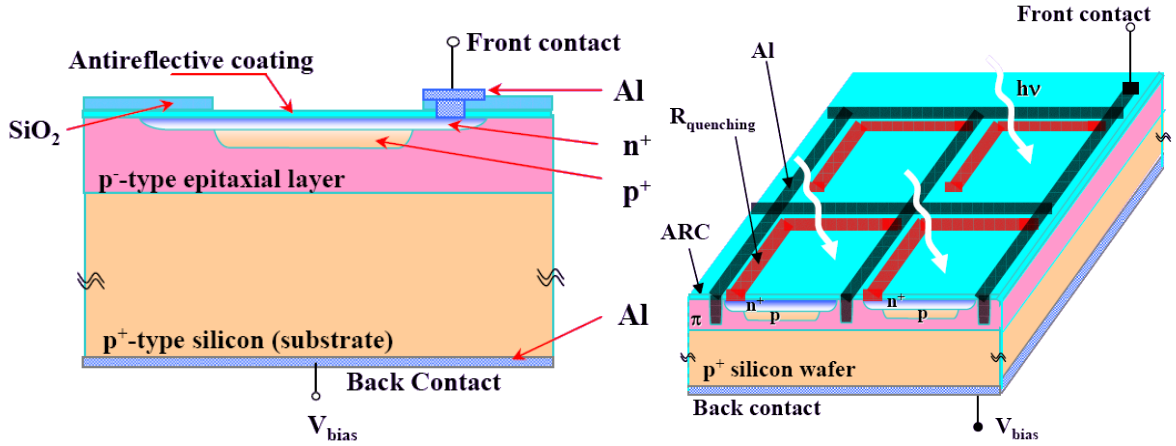

Figure 3.5: (a): Sketch of the section of a microcell (single GAPD) [10]. The epitaxial layer is fully depleted at operation voltage. This configuration corresponds not exactly to the Hamamatsu GAPD array. (b): Array of single GAPDs in a parallel circuit. The amplitude of the output signal is proportional to the number of incident photons [10].

For more details about GAPDs and their behavior see e.g. [11], [12].

[1] Measurements by Dieter Renker, PSI, 2008, gave a value of about $C_D = 310\ fF$ for the 100x100 μm^2 GAPD arrays from Hamamatsu, which corresponds to a time constant of about 40 ns.

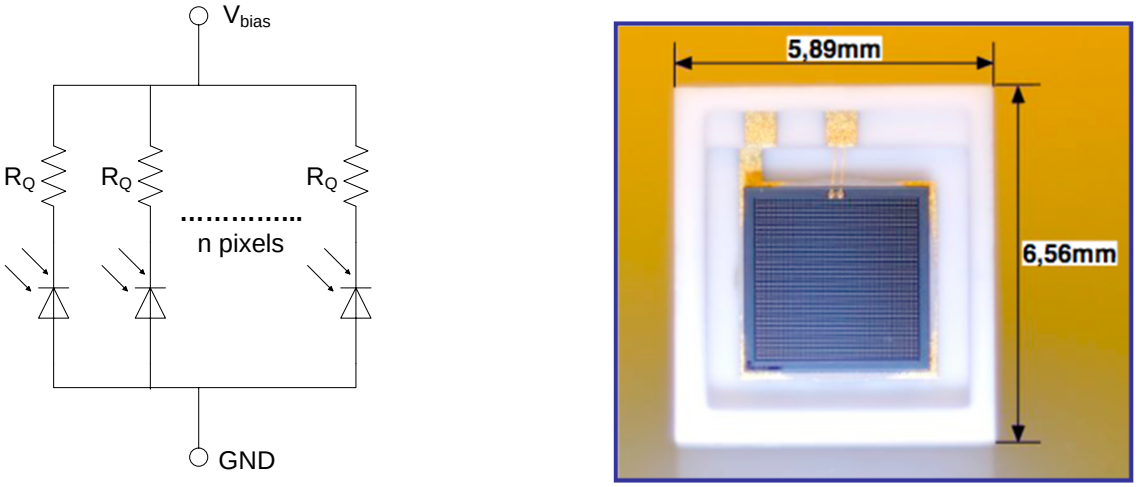

(a) (b)

Figure 3.6: (a): Array of single GAPDs in a parallel circuit. (b) Photo of the Hamamatsu GAPD array S10362-33-100C.

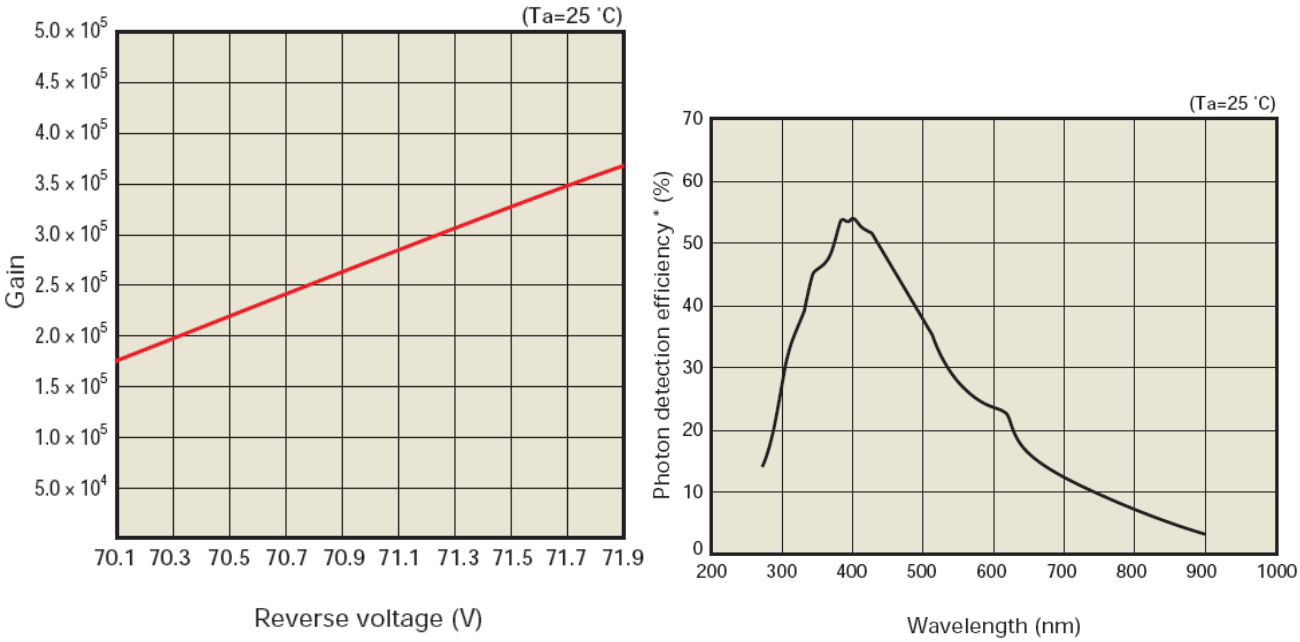

(a) (b)

Figure 3.7: (a): Typical gain behavior of a GAPD array in function of its bias voltage [17]. The gain is also temperature dependent. (b): Photon detection efficiency (PDE) of a Hamamatsu GAPD array. New measurements from Hamamatsu show a shift of the curve with a peak at about 440 nm. The PDE includes effects of optical crosstalk and afterpulses [17].

3.2 Working with GAPDs and getting real data

A test setup is designed and built to get an idea of how GAPDs work and to study their output signal shape. The measured GAPD signal shapes are used to optimize the signal reconstruction algorithm. The pulse measurements are used as input for a Monte Carlo simulation of Cherenkov showers and night sky background. These Monte Carlo data are used to test the developed reconstruction algorithm.

3.2.1 Test setup

Figure 3.8 shows a block diagram of the test setup. It consists of a pulsed photon source, which emulates a Cherenkov shower pulse, a GAPD with preamplifier, a bias source and an oscilloscope. Since no light pulse source with the needed properties was available, a suitable optical pulse generator was built (see section 3.2.2). Besides the GAPD, the preamplifier and the laser diode with driver, which will all be described in the next subsections, the following equipment is used:

Bias source	Keithley 6487 Picoammeter/Voltage Source
Oscilloscope	Le Croy WavePro 950
Pulse generator	NIM Trigger Unit DT104
Miscellaneous	Power supplies for 5 V, 8 V and 0..20 V

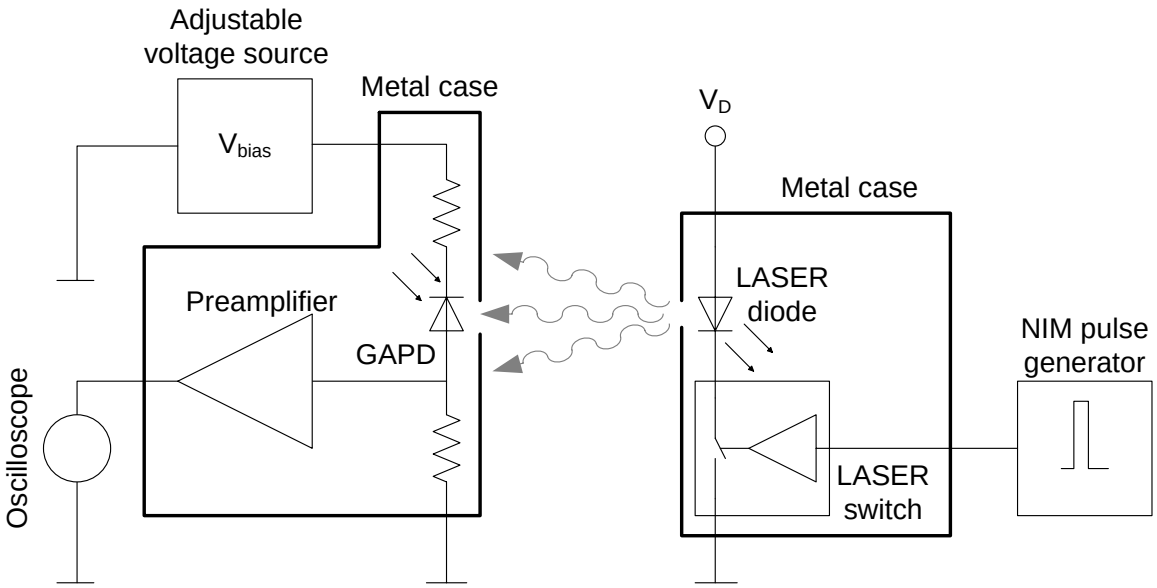

Figure 3.8: Test setup with the laser light source and a pulse generator on the right hand side and the GAPD with preamplifier, bias supply and oscilloscope on the left hand side.

3.2.2 Photon source

The photon source consists of a blue laser diode [14] with a wavelength of 406 nm. The diode is driven by a special high speed laser switch [15], which allows a pulsed operation upto 155 MHz

(corresponding to a pulse width of about 6 ns). The whole circuit is encased by a metal box for shielding purposes and the light is emitted through a small hole in the box. The complete circuit is shown in figure 3.9.

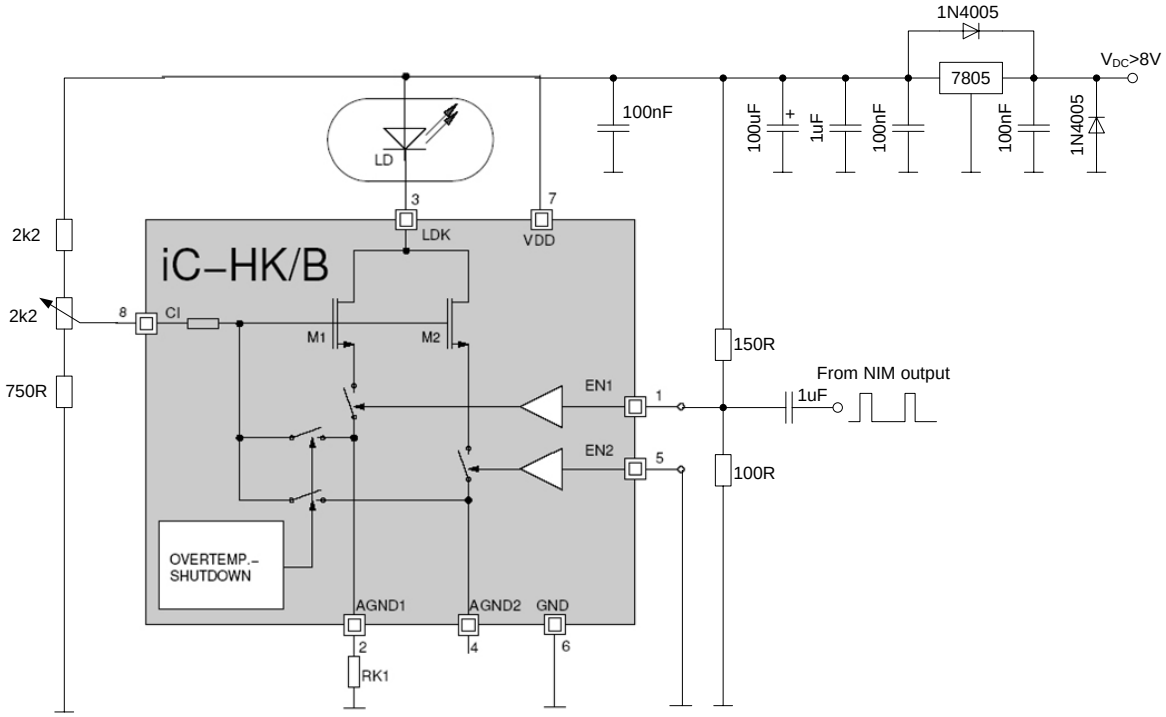

Figure 3.9: Laser driver (iC-HKB from IC-Haus [15]) with voltage regulator.

3.2.3 Preamplifier

The output signal of a GAPD is too weak (about 200 μV for a single incident photon at nominal bias) to be measured directly with the oscilloscope with reasonable signal to noise. Thus a preamplifier from Photonique [16] with an amplification of ten at 5 V is used. Figure 3.10 shows the block diagram of the preamplifier with the wiring of the GAPD and the bias source.
The GAPD, preamplifier and passive filters in the power supply wiring to suppress external noise are mounted onto a common PCB. This PCB is mounted in a metal box with a small hole in front of the GAPD. The GAPD is placed about 1.5 cm away from the hole to allow an exposure of the whole active surface. With this setup a signal of about 2 mV for an incident photon is measured.

3.2.4 Measurements with the test setup

The following measurements were performed:
- measurements of dark count to estimate the 1-photon amplitude and the dark count spectrum
- measurements with pulsed laser at different intensities and distances to simulate Cherenkov showers

All measurements shown here are performed on the GAPD with serial number 336.

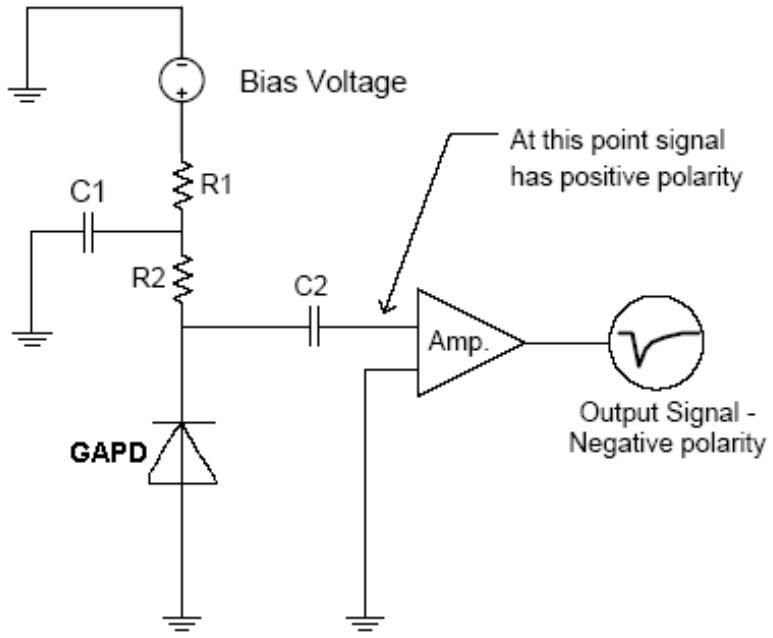

Figure 3.10: Block diagram of the Photonique preamlifier AMP_0611. The values are R1 = 2 kΩ, R2 = 1 kΩ, C1 = 10 nF and C2 = 10 nF [16].

3.2.4.1 Dark count

The dark count of a GAPD is the number of avalanche discharges that are not initiated by a photon (see also section 3.1). For this measurement, the GAPD is darkened and the whole setup is left switched on for about ten minutes for temperature stability before taking data. The expected rate of about 1 to 10 MHz of such events could be confirmed. As shown later, this rate is far below the night sky background rate (100 to 3000 MHz) and therefore negligible. Figure 3.11 shows such measurements whereas figure 3.12 displays the spectrum of the dark count. The 1-photon amplitude measured with this setup and for the applied bias voltage corresponds to about 2.5 mV.

3.2.4.2 Pulsed laser measurements

By placing the laser box at a certain distance from the GAPD box, the "intensity" of the "Cherenkov shower" pulses can be regulated. Unfortunately, the laser pulses have random intensities (between zero to fifteen photons per pulse at a given distance) thus no prediction about the difference between the emitted and the measured intensity is possible. Nevertheless, an analysis of the signals can be made where the pulse height is read out with the oscilloscope and compared with the reconstructed pulse amplitude. Figure 3.13 shows two measurements of a laser pulse. The trigger pulse from the pulse generator is shown in red (dashed line). The time delay between trigger and laser pulse arise from different cable lengths. The measured laser pulses have amplitudes that correspond to about five and three photons (assuming 2.7 mV/photon). The small 1-photon pulses are dark counts of the GAPD. The night sky background can be simulated by placing a light bulb near the GAPD box and by regulating its brightness (see fig. 3.14). The measurements show now many large pulses caused by the light coming from the bulb. The laser pulse is still visible but since it may have piled-up on background pulses, no accurate amplitude estimation is possible. The background frequency

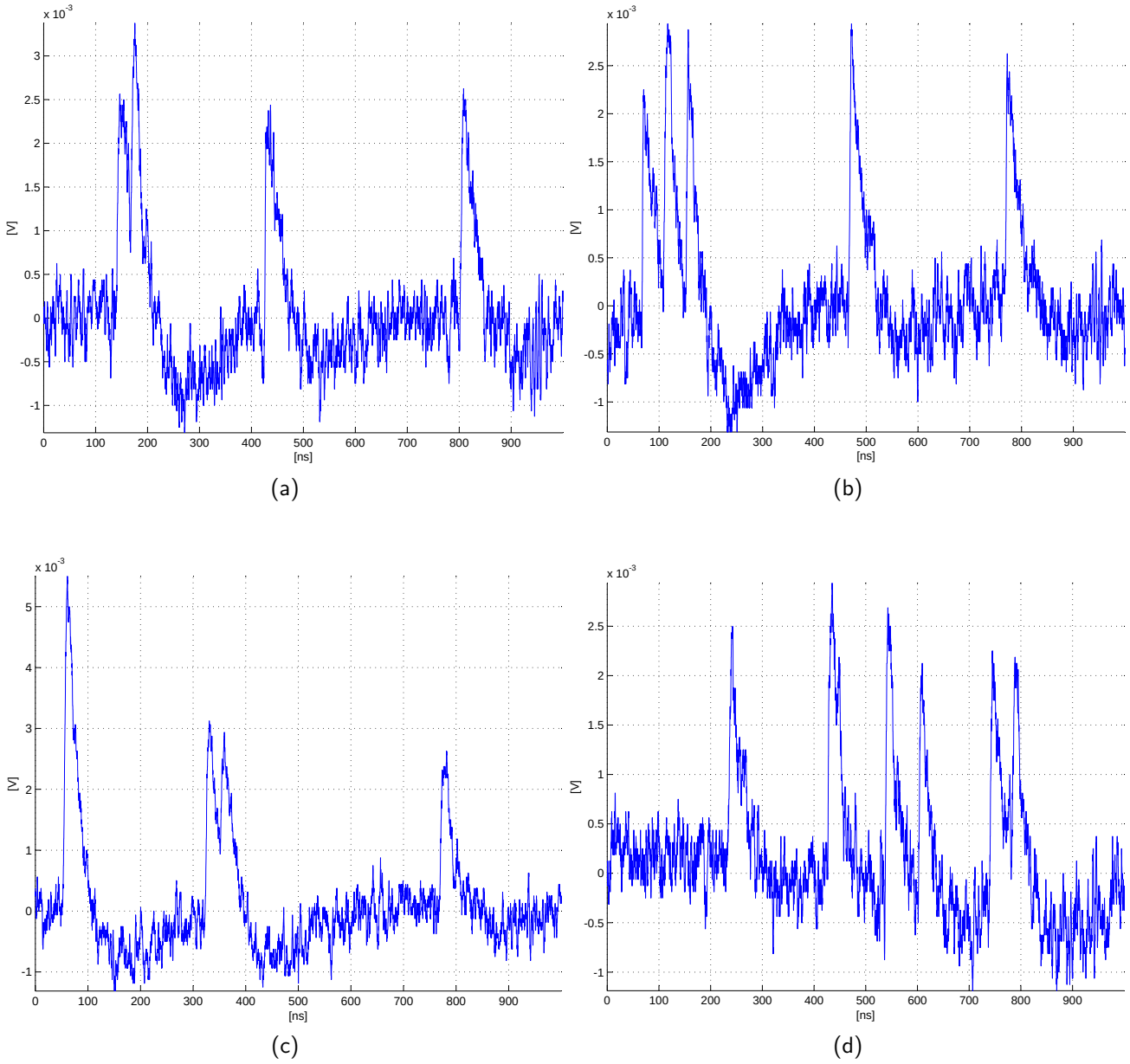

Figure 3.11: Dark count measurement at $V_{bias} = 70.1$ V and $I_{bias} = 0.8$ μA (measurements sc1.008, sc1.048, sc1.058, sc1.067 from 24.10.08). The GAPD is darkened with a black cloth. The x-axis shows a time interval of 1000 ns and the y-axis the amplitude in mV. The 1-photon amplitude corresponds to about 2.5 mV. (a) shows four 1-photon dark count pulses. (b) shows a pile up of three pulses. The first pulse in (c) is a 2-photon event. (d) shows six 1 photon events and demonstrates that the pulse amplitudes are not perfectly identical for all events due to the rather small signal to noise ratio and other GAPD internal effects.

can be estimated by counting all pulses that look like a single- or multi-photon event. Therewith a background rate of about 15 and 30 MHz is estimated for these measurements.
A measurement of a single multi-photon pulse is used in the emulation of GAPD signals (see section 4.2.1).

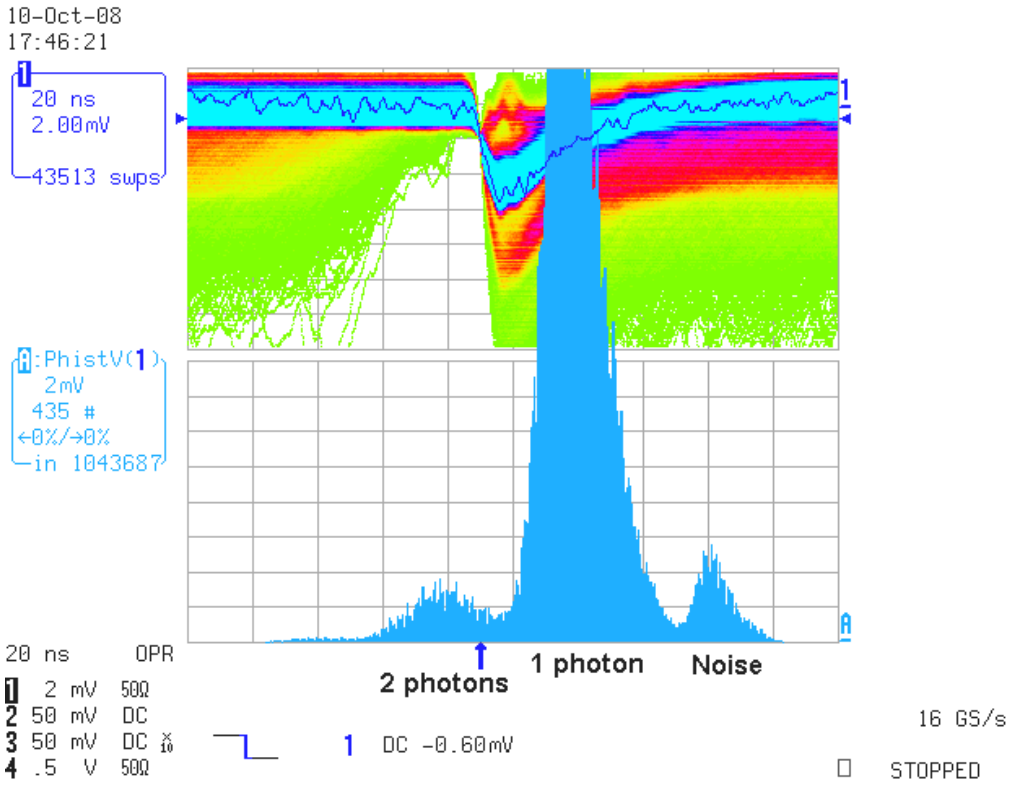

Figure 3.12: Pulse height spectrum (analog persist) at $V_{bias} = 70.4$ V and $I_{bias} = 1.4$ μA. The GAPD is completely darkened so that only dark count signals are measured. The upper part shows the overlaid GAPD output signals and the lower part shows a histogram of the signal amplitude, with a huge peak for 1 photon events which as expected are most probable and a small peak for two photon events.

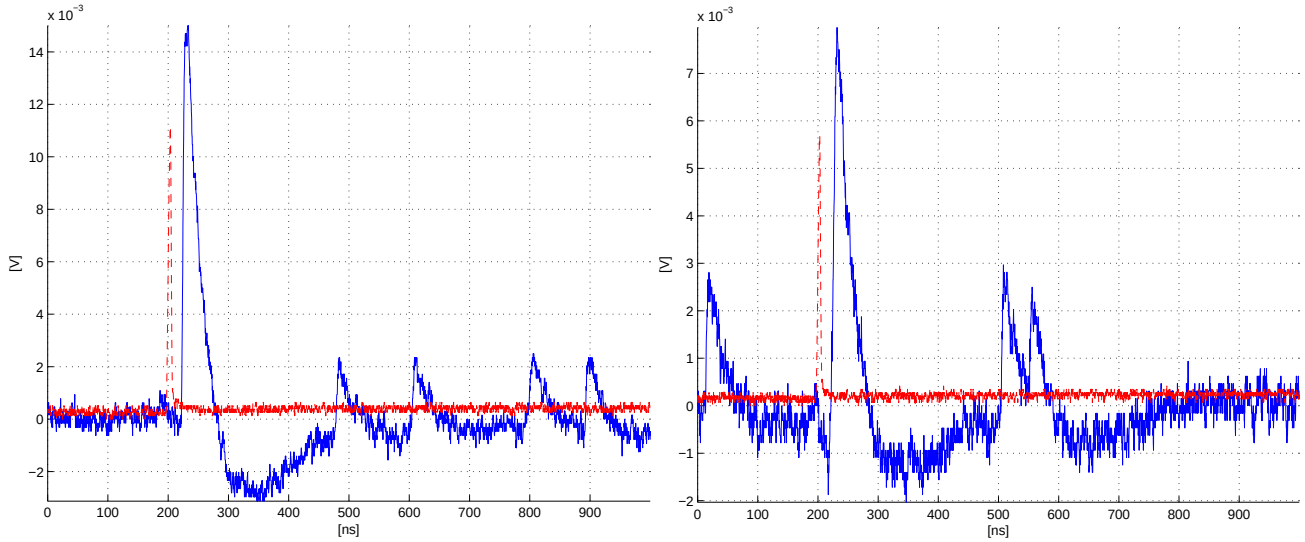

(a) (b)

Figure 3.13: Measurements of laser pulses at V_{bias} = 70.05 V and I_{bias} = 2 μA (measurements sc1.038, sc1.044 from 21.10.08). The GAPD is placed at a certain distance in front of the laser which emits a pulse of about 6 ns duration. The x-axis shows a time interval of 1000 ns and the y-axis the amplitude in mV. The 1-photon amplitude corresponds to about 2.7 mV. The red dashed line shows the laser trigger signal. (a) the first pulse is the laser pulse with an amplitude of about 5 photons. The other pulses are dark count or maybe afterpulses. (b) same as (a) but with a laser pulse amplitude of about 3 photons.

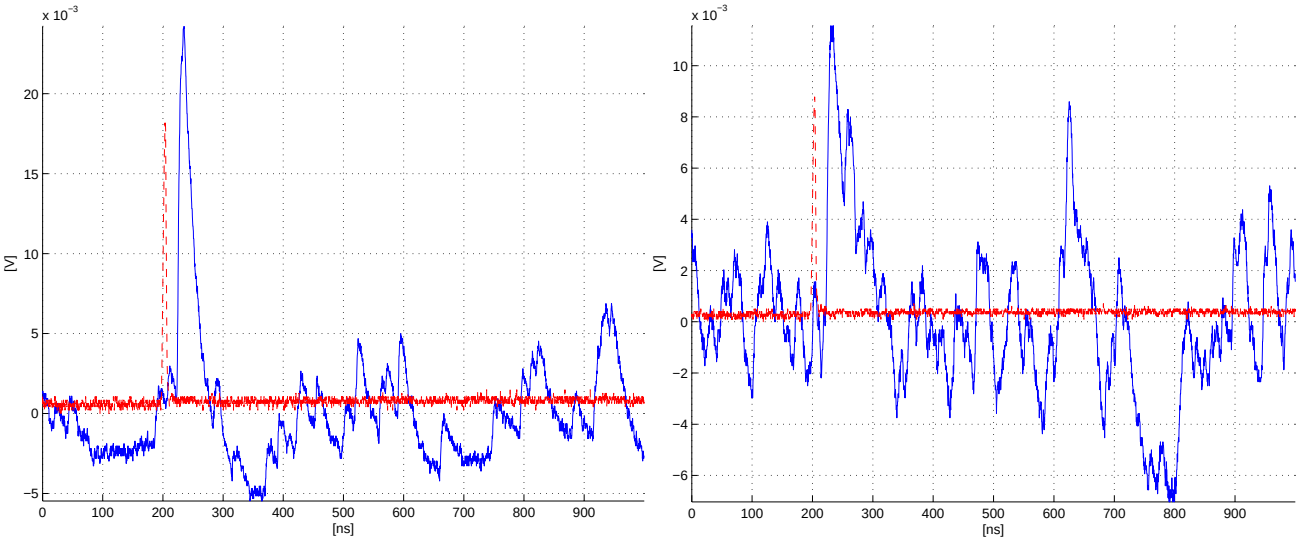

(a) (b)

Figure 3.14: Measurements at $V_{bias} = 70.05$ V (measurements sc1.079, sc1.081 from 21.10.08), with the GAPD placed at a certain distance in front of the laser, which emits a pulse of about 6 ns duration. A light bulb placed near the GAPD box simulates the night sky background. The x-axis shows a time interval of 1000 ns and the y-axis the amplitude. The 1-photon amplitude corresponds to about 2.7 mV. The red dashed line shows the laser trigger signal. (a) the first pulse is the laser pulse with an amplitude of about 8 photons. The other pulses are dark count and night sky background from the light bulb with a frequency of about 15 MHz. (b) same as (a) but with a brighter light bulb that increases the background frequency to about 30 MHz. The laser pulse has an amplitude of about 5 photons.

4 Reconstruction algorithm

The purpose of this reconstruction algorithm is to perform an online analysis of a continuous data stream from a detector (e.g. a GAPD) without applying a trigger condition. Hence no dead time occurs during processing and narrow piled-up signals should become distinguishable. The algorithm should only select promising pulses and suppress noise at first level. If the output signal is composed of superposed single pulses, like GAPD output signals, one approach is to identify each single pulse and save only a time stamp and amplitude information for each recognized pulse. A threshold on the reconstructed amplitude can reduce the amount of data considerably.
Based on an idea of Professor Dr. Ulrich Straumann and Dr. Achim Vollhardt a cross-correlation algorithm has been developed to extract single pulses and its reconstruction power was tested on measured and simulated GAPD pulses.

4.1 The cross-correlation function

The cross-correlation function is used in many different fields for image and pattern recognition, waveform analysis and more. The cross-correlation "measures" the similarity of two "shapes" (e.g. images, waveforms). Most commonly it is used to search a long duration signal for a shorter, known feature. The input to the cross-correlation is therefore a long duration signal and a template which describes the pulse shape sought.

4.1.1 Mathematical definition

For two continuous functions f and g the cross-correlation is defined as:

$$(f * g)(t) \equiv \int_{-\infty}^{\infty} f^*(\tau)\ g(t+\tau) d\tau \tag{4.1}$$

where f^* is the conjugate of f. Similarly, for discrete functions, the cross-correlation is defined as:

$$(f * g)[n] \equiv \sum_{m=-\infty}^{\infty} f^*[m]\ g[n+m] \tag{4.2}$$

The autocorrelation function corresponds to the cross-correlation of a signal with itself.
To illustrate formulae 4.1 and 4.2, consider f a template function (fig. 4.1a) which describes a demanded feature in the test signal g (fig. 4.1b). The cross-correlation formula essentially slides the test signal g along the time (or position) axis, calculating the integral (or the sum for discrete functions) of the product of f and g at each sliding step t (or n). When the two functions match, the cross-correlation value $(f * g)$ maximizes.
By inverting sign of the test signal or of the template, an anti-correlation (a minimum instead of a maximum) appears where a correlation was seen before. Changing the role of the two functions f and g only swaps the time/position of the cross-correlation output.

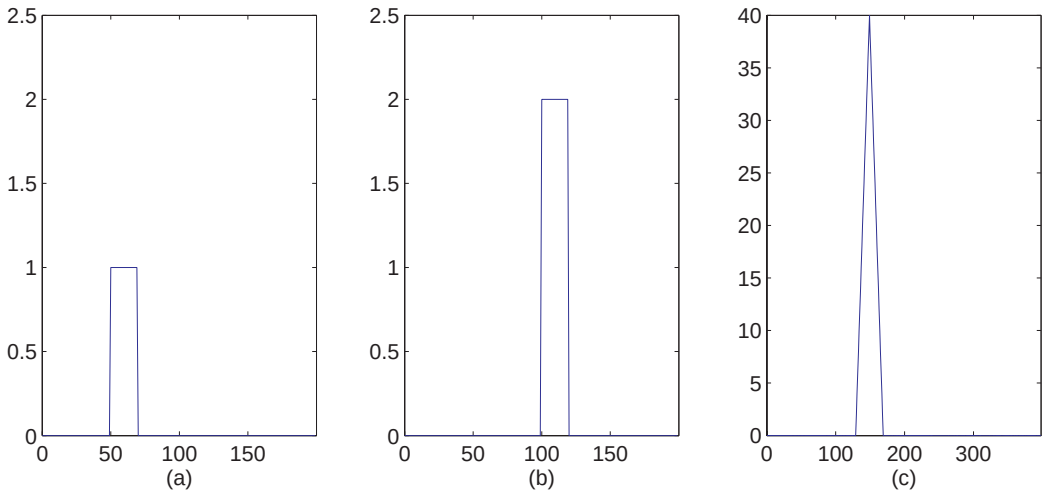

Figure 4.1: Principal of the cross-correlation function. (a) Template function f with an amplitude of 1. (b) Test function g with an amplitude of 2. (c) Cross-correlation $(f * g)$ according to equation 4.2.

4.1.2 Working with the cross-correlation function

Figures 4.2 and 4.3 show a slightly more advanced example. Figure 4.2 shows (a) the signal template function and (b), (c) and (d) show three different test functions. The first test function is simply the boosted template function, the second test function implies a sign inversion and the third test function is a composition of two succeeding template functions with different amplitudes. As the

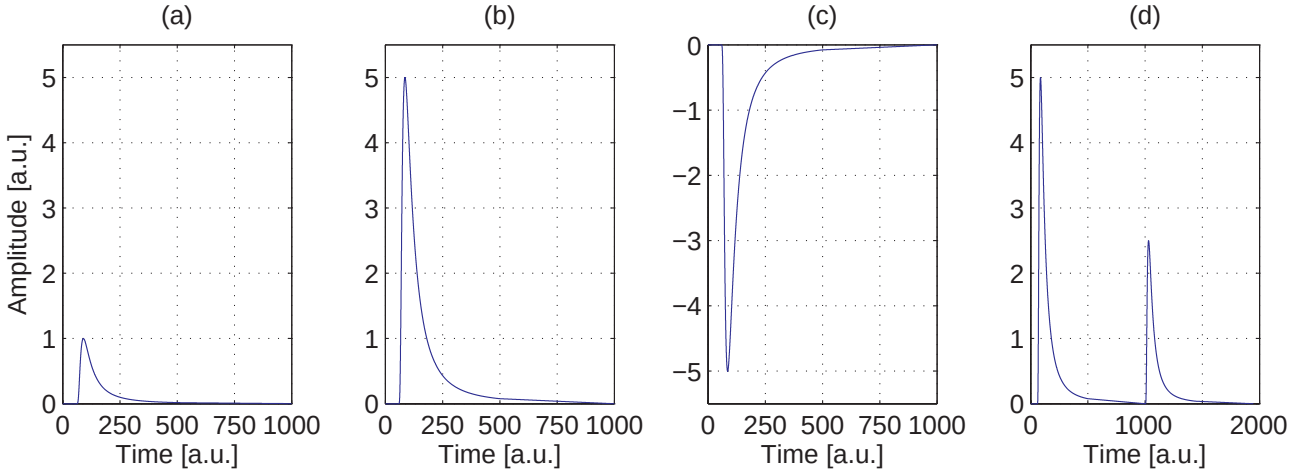

Figure 4.2: Figure (a) shows the template function. Figures (b) to (d) show arbitrarily chosen functions to show how the output of the cross-correlation with the template will look like. (b) is same as the template function with a 5 times bigger amplitude. (c) is same as (b) but inversed in sign. (d) shows two succeeding (b) pulses with amplitudes 5 and 2.5.

cross-correlation (fig. 4.3) between the template function and each test function shows, a distinct peak, either a maximum or a minimum for correlation or anti-correlation, respectively, occurs at the expected position. The amplitude of the peak is a measure for the correlation. Thus by analyzing

the peak's amplitude and position in the correlation function, the amplitude and position of the appearance of the template function in the test function can be determined. The better the correlation the better the reconstruction of each amplitude and position and the better the reconstruction of the complete signal.
No deterioration of the cross-correlation is observed even when a large white noise is superposed on the test function (fig. 4.4). If the sought signal is heavily distorted by superposition of a low frequency noise (e.g. 50 Hz interferences) as shown in figure 4.5a, a slightly distorted cross-correlation shows up. Additional peaks appear and make the analysis more difficult. This behavior gets worse the more complicated the noise pattern is. Furthermore, the amplitude of the cross-correlation decreases due to a less good match of the two functions.
Another problem is that appears when two template functions that appear too close to each other in the test signal are not discernible in the cross-correlation. As figure 4.7 shows, the test signal (a) produces only one maximum in the cross-correlation output (b) although two pulses are piled-up. The second pulse in the test signal only leads to a tiny bump on the right side of the peak in the correlation function. This bump corresponds to the second peak of the test signal. A better sensitivity to the second pulse can be obtained by using the second derivative of the cross-correlation. The second derivative is given by the curvature of the trajectory and has a negative peak at the position of a local maximum of the trajectory. Figure 4.6 shows the second derivative of the cross-correlations discussed in figure 4.3. All maxima in the cross-correlation function emerge as sharp negative peaks in the second derivative and permit to reconstruct the position of the original signal. Interestingly the amplitude ratio of the two peaks is the same as in the source signal.

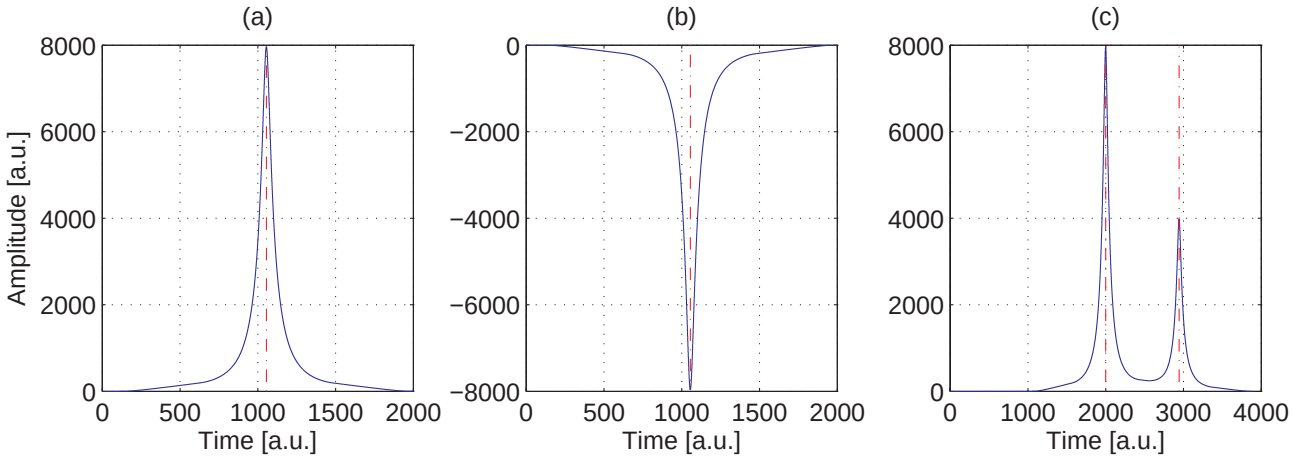

Figure 4.3: Output of the cross-correlation function with template function fig. 4.2(a) and test functions fig. 4.2(b) to (d). The dashed lines give the expected positions of the cross-correlation maxima and minima, respectively. (a): a perfect correlation between template and test signal. (b): a perfect anti-correlation. (c): both pulses of the test signal show a good correlation with the template. The positions of all found maxima and minima correspond to the expected values.

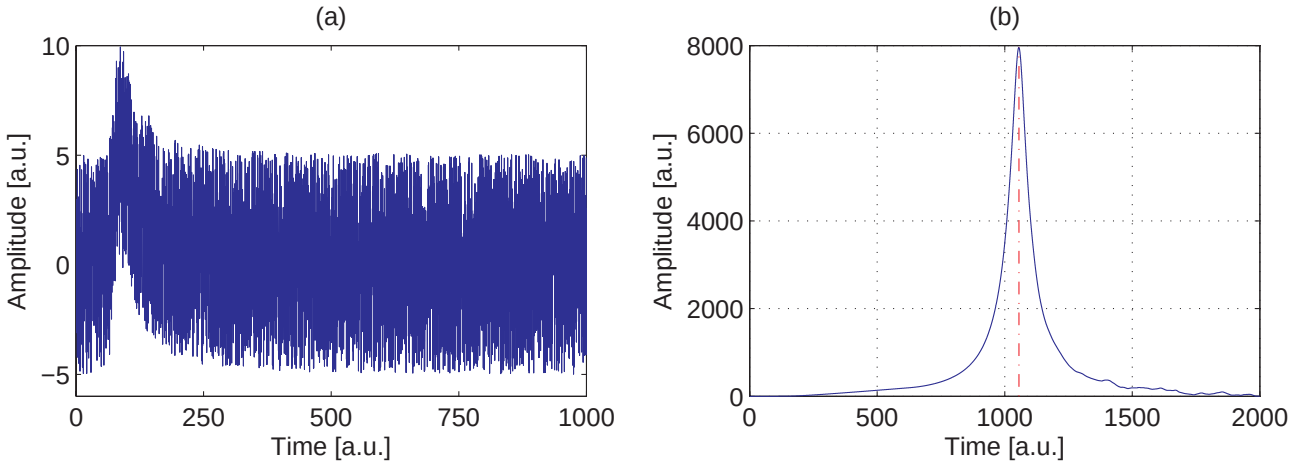

Figure 4.4: (a) shows the same template function as in fig. 4.2a with a superposed white noise. (b): the cross-correlation peaks very clearly at the correct position and amplitude.

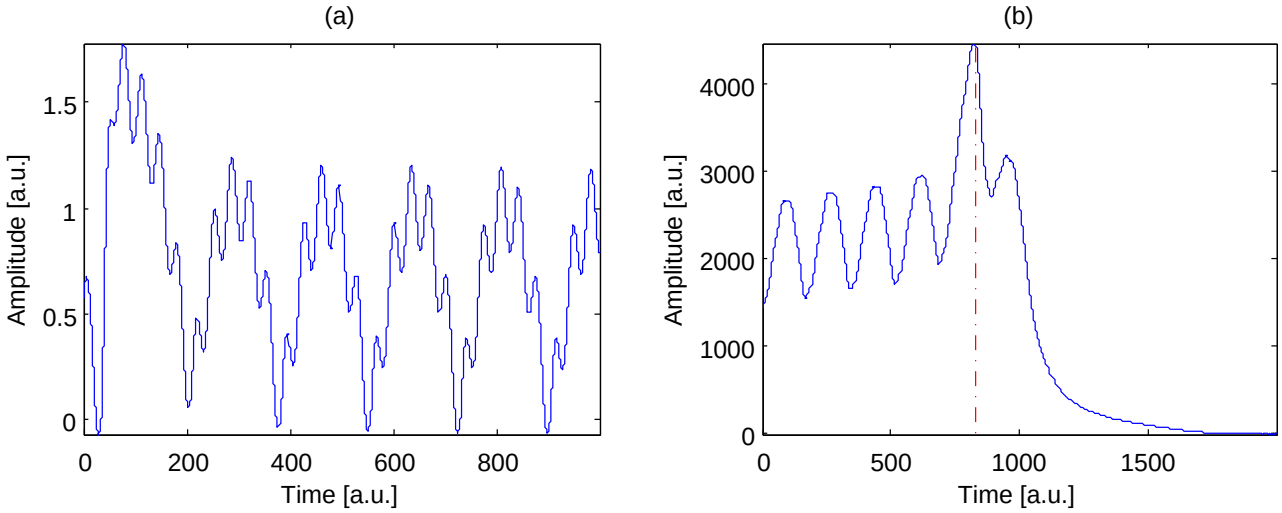

Figure 4.5: (a) shows the same template function as in fig. 4.2a with a superposed low-frequency noise. (b): the cross-correlation peaks at the correct position although the noise distorts the signal.

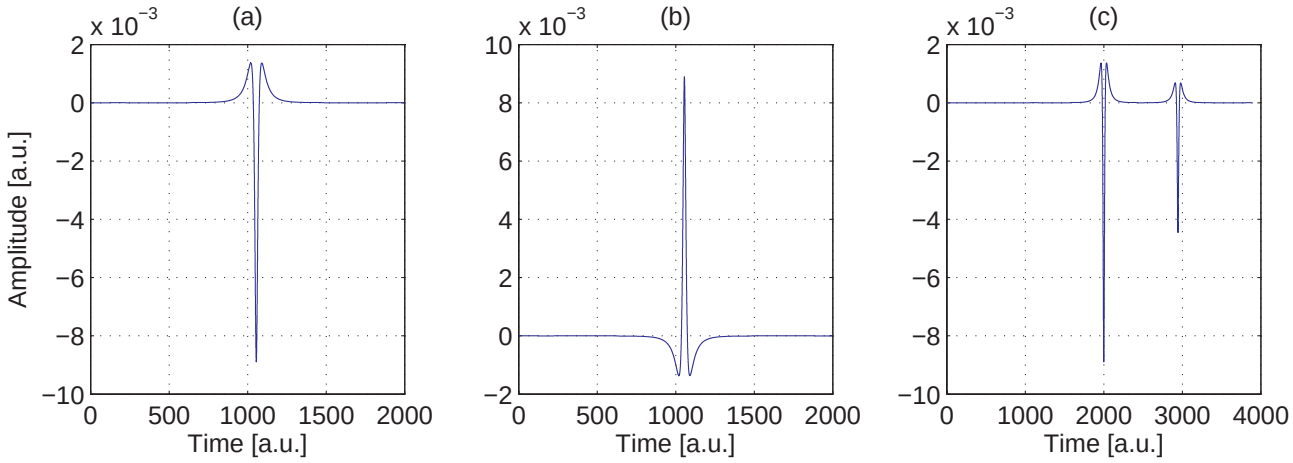

Figure 4.6: Second derivative of the cross-correlation for the test signals shown in fig. 4.2(b) to (d) with the template function shown in fig. 4.2(a). Sharp peaks emerge at the correlation maxima. The negative peak value is explained in the text.

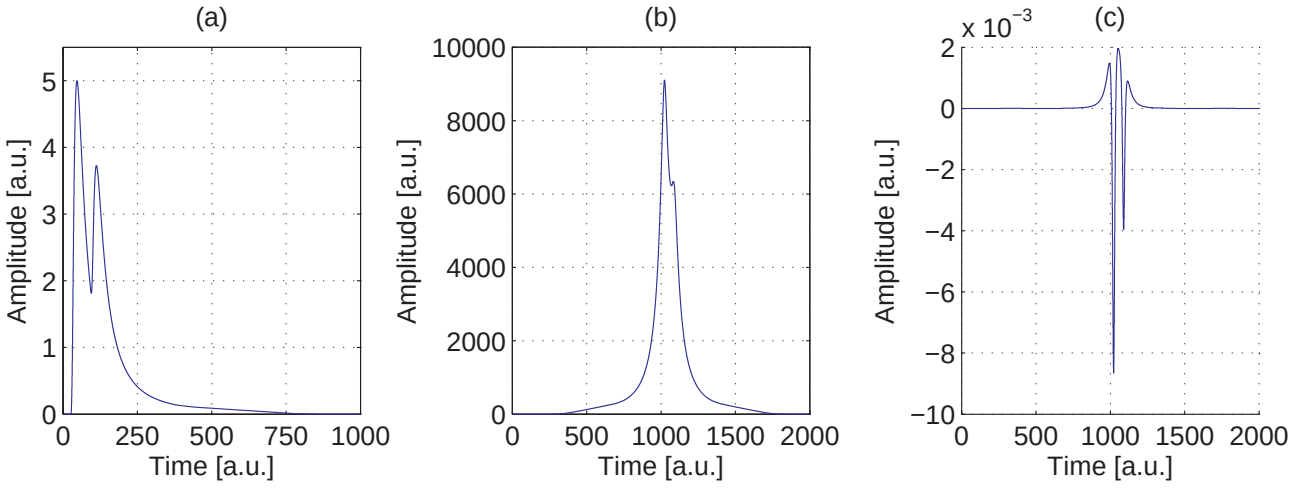

Figure 4.7: An example of two closely piled-up pulses with different amplitudes (a), the second pulse having half the amplitude of the first one. The cross-correlation function (b) gives no feasible information about the second pulse whereas the second derivative of the cross-correlation (c) gives a clear signal for both pulses. The amplitude of the second peak, corresponding to the first pulse in (a), has about half the value of the first peak.

4.1.3 Pile up and the second derivative

We discuss shortly the reconstruction power of the cross-correlation on narrow piled-up pulses and the properties of the second derivative.

4.1.3.1 Pile up study

Figures 4.8(a), 4.9(a) and 4.10(a) show three different test signals with piled-up pulses, with a time difference of 4.6 ns and with amplitude ratios of 1:2, 2:1 and 1:1 (first pulse to second pulse amplitude) respectively. Figures (b) show the cross-correlation output in which only one peak is visible. Figures (c) represent the second derivatives of the cross-correlation in which two single peaks show up. The two peaks are zoomed in in figures (d). The amplitude ratios of the second derivative peaks match quite well the ratios of the test signals (see below).
Figure 4.11 shows that even signals with a time difference of 2.3 ns are distinguishable using the second derivative of the cross-correlation.
For real data, the minimum piled-up time that can be resolved will depend critically on the sampling settings of the ADC and on the distortion/noise of the measured signal.

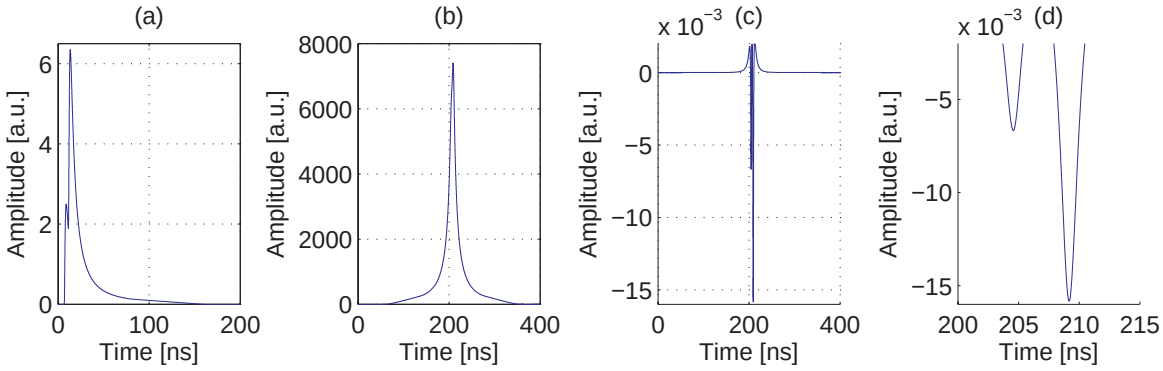

Figure 4.8: (a) Test signal with two piled-up pulses with a time difference of 4.6 ns. The first pulse has an amplitude of 2.5 and the second one an amplitude of 5. (b) Cross-correlation of the test signal with the template. (c) Second derivative of the cross-correlation. (d) Zoom in of figure (c).

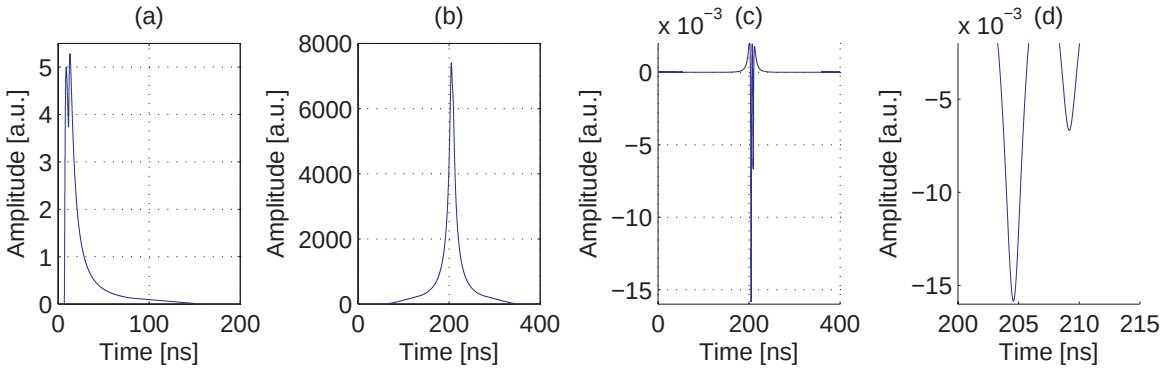

Figure 4.9: (a) Test signal with two piled-up pulses with a time difference of 4.6 ns. The first pulse has an amplitude of 5 and the second one an amplitude of 2.5. (b) Cross-correlation of the test signal with the template. (c) Second derivative of the cross-correlation. (d) Zoom in of figure (c).

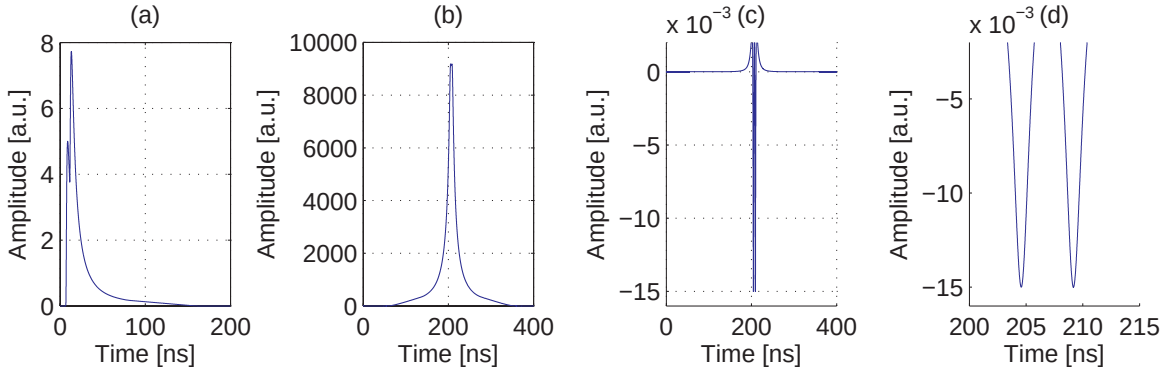

Figure 4.10: (a) Test signal with two piled-up pulses with a time difference of 4.6 ns. Both pulses have an amplitude of 5. (b) Cross-correlation of the test signal with the template. (c) Second derivative of the cross-correlation. (d) Zoom in of figure (c).

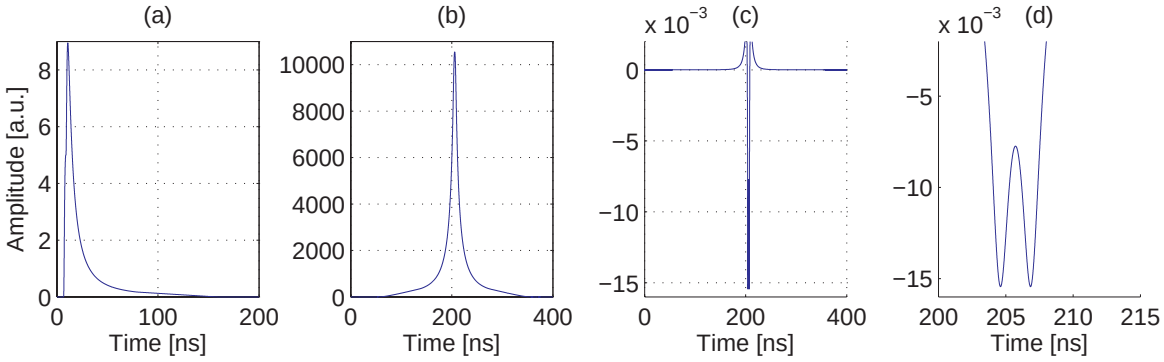

Figure 4.11: (a) Test signal with two piled-up pulses with a time difference of 2.3 ns. Both pulses have an amplitude of 5. (b) Cross-correlation of the test signal with the template. (c) Second derivative of the cross-correlation. (d) Zoom in of figure (c).

4.1.3.2 The second derivative

The second derivative of a function gives its curvature and is negative at the location of a maximum. Looking at the cross-correlation of three Gaussians (4.12a) of the same width and with amplitude ratios of 1:1, 1:2 and 1:4, one can see that the curvature at the maximum becomes sharper with increasing amplitude. This leads to an increasing second derivative minimum as shown in figures (b), (c) and (d). For this reason one gets an amplitude information out of the second derivative of the cross-correlation.

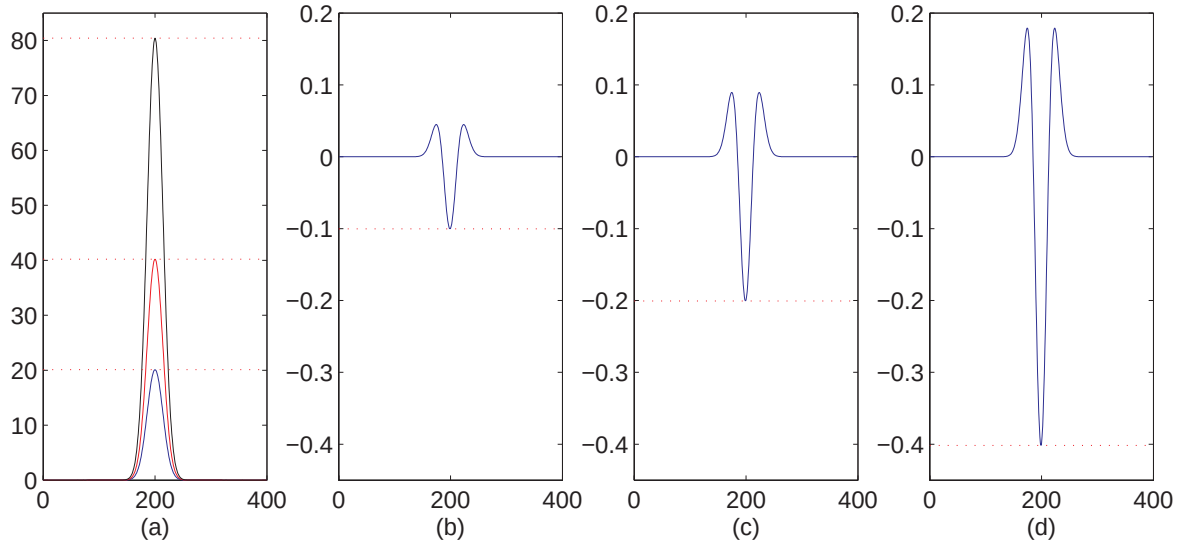

Figure 4.12: Cross-correlation and second derivatives of two Gaussian functions with 1:1, 1:2 and 1:4 amplitude ratios. (a) The smallest curve corresponds to the cross-correlation of the two Gaussian with same amplitude. The middle one to the 1:2 and the biggest to the 1:4 amplitude ratio. One can see, that the maximum increases by a factor of 2 and 4, as expected. (b), (c) and (d) show the second derivative of each correlation. The minima have again the amplitude ratio of 1:2:4.

An analysis of the second derivative of the cross-correlation makes sense, if a reconstruction of piled-up signals of same or similar shape is required. The amplitude of the (local) minima and their positions give a good information on the structure of the original signal. The behavior of the second derivative of the cross-correlation is studied on measured and simulated GAPD signals. Data is taken with the test setup described in section 3.2 and simulated data samples are created with a MATLAB [18] emulation of the hardware as described in the next sections.

4.2 Hardware emulation with MATLAB

Figure 4.13 shows the block diagram of a possible readout circuit of a GAPD with the GAPD on the left, an AC coupling capacitance C_{AC}, an analog to digital converter (ADC) and a Field Programmable Gate Array (FPGA) that holds the processing algorithm. These four blocks are all implemented in a MATLAB file for simulations. Here, only the cross-correlation algorithm that would be implemented in the FPGA shall be discussed in detail in section 4.3 while the other three blocks are presented in a compact and short manner.

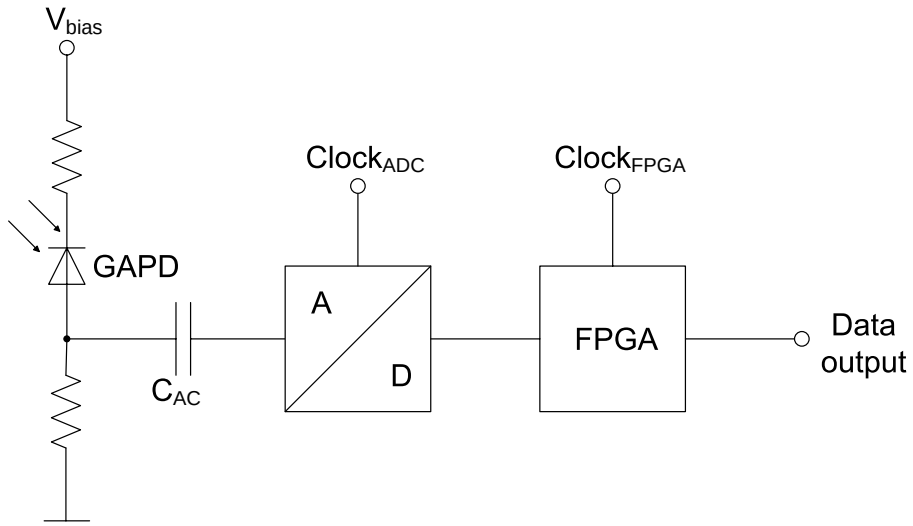

Figure 4.13: Block diagram of the GAPD readout electronics. The capacitor C_{AC} serves as high-pass filter let passing only AC signals (DC base is cut off). The signal is processed in the FPGA by the algorithm after analog digital conversion. The time and amplitude stamp output of the algorithm is then sent to a data acquisition unit.

4.2.1 GAPD emulation

In this code fragment the output signal of a GAPD is emulated by superposition of a well defined number of single pulses to simulate the night sky background and the Cherenkov shower. The single-photon pulse shape is taken from a measured and normalized GAPD pulse (fig. 4.14a, no preamplifier was used). This pulse is uniformly distributed with a given frequency and over a one microsecond long signal sample to simulate the night sky background. To simulate the Cherenkov shower, a single n-photon pulse (single photon pulse multiplied by a factor n) is placed randomly or for better control at a well defined time-position within the interval. Figure 4.14b shows such a constructed signal sample with a 5-photon shower pulse at 210 ns and a background frequency of 30 MHz. For comparison, a measured signal with about 30 MHz background frequency and a laser pulse of about 5 photons at 230 ns is shown in figure 4.14d (see also section 3.2).

4.2.2 High-pass filter

The emulated GAPD pulse is passed through a high-pass filter with a cut-off frequency of f = 1 MHz. This high-pass filter corresponds to the AC coupling in front of the analog to digital converter (ADC), which has a capacitance of $C_{AC} = (2\pi f R)^{-1} = 0.15$ nF and a R = 1 kΩ resistor (see fig. 4.13).

4.2.3 Analog to digital conversion

The analog to digital converter (ADC) is implemented in MATLAB with respect to the highest flexibility. The resolution can be varied between 8, 10, 11 and 12 bits and the sampling rate can be varied between 1000, 500, 333 and 250 MHz (1, 2, 3, 4 ns time resolution). A logarithmic ADC is also implemented but has not been used yet. The dynamic range is set to 400 photons so that 8 bits resolution correspond to $400/2^8 = 1.56$ photon resolution per bit and for 12 bits correspond to a

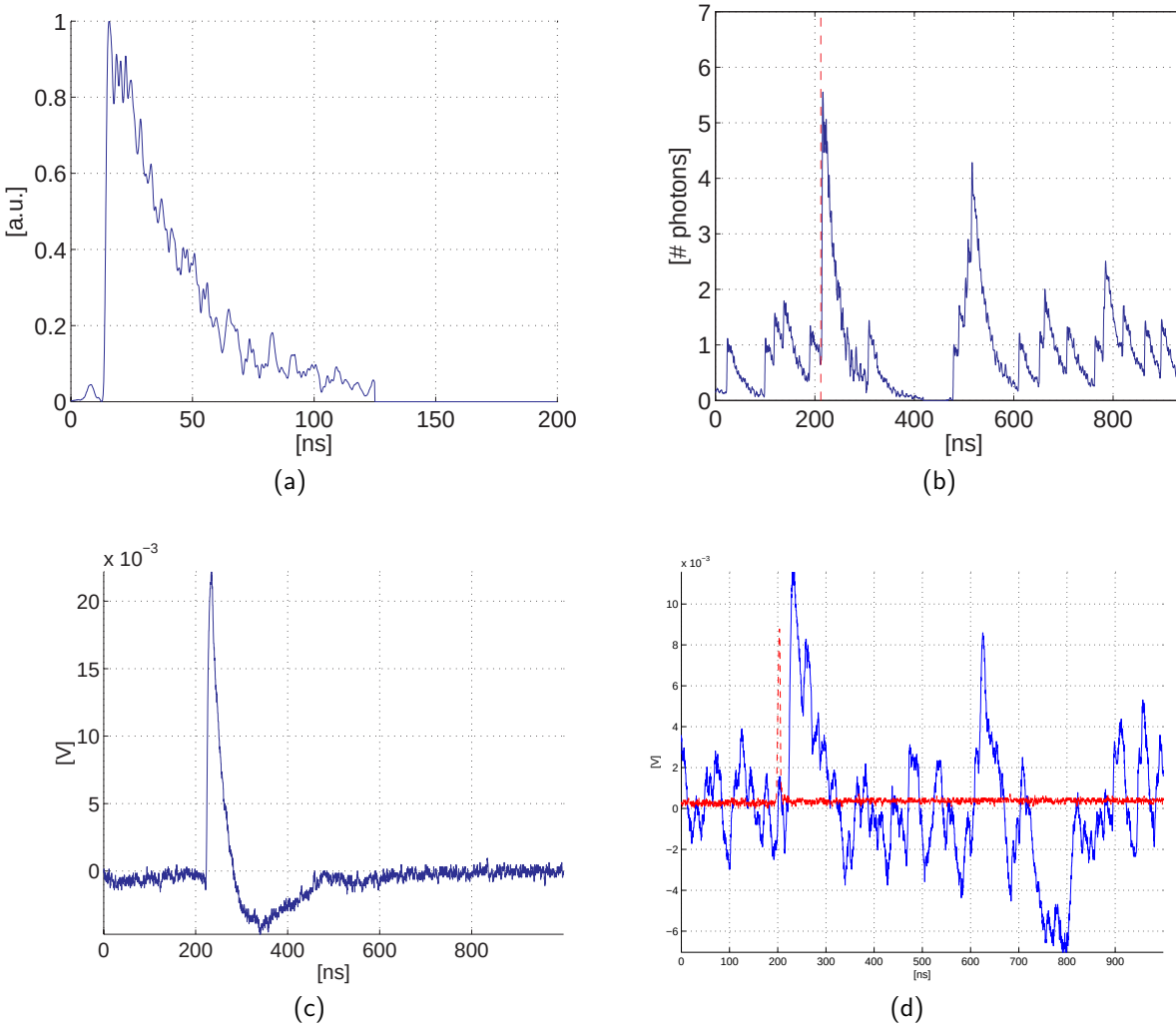

Figure 4.14: (a): Measured GAPD pulse without a preamplifier, used for signal synthesis. (b): A simulated GAPD signal with 30 MHz background frequency and a Cherenkov shower of 5 photons at 210 ns. (c): Output signal of the Photonique preamplifier. The undershoot is almost three times as long as the GAPD signal. (d): A measured GAPD signal with about 30 MHz background frequency and a 5 photon pulse at 230 ns. This signal looks a bit different due to the undershoot of the Photonique preamplifier.

resolution of $400/2^{12} = 0.09$ photons per bit. A proper choice of the dynamic range has a huge effect on the reconstruction quality, especially for small bit resolutions.

4.3 Cross-correlation algorithm implementation in MATLAB

After the digitization of the GAPD signal, the online and triggerless reconstruction is performed using the algorithm discussed above. The cross-correlation algorithm is implemented step by step in MATLAB with the idea that the code can be imported without changes in an FPGA compiler and in the FPGA itself. To maintain the generality of the code instructions, no special MATLAB functions where used. In order to understand the reconstruction algorithm, all MATLAB lines are

listed in list 4.1 and explained afterwards. But first, the proper template function needs to be defined.

4.3.1 The template function

To fit the measured GAPD pulse (fig. 4.14a) as well as possible and to optimize the power of the reconstruction algorithm, different template functions were checked. These tests were very time consuming and showed that due the many varying signal parameters, the optimization is better left to the stage, where real measured signals are available for reconstruction. Therefore, one should take the presented template as a guidepost with potential for further optimization.

The finally used template function is the so called generalized extreme value probability density function (fig. 4.15a). The MATLAB version of this function is $Y = gevpdf(X, K, \sigma, \mu)$ and the formula is:

$$f(X; K, \sigma, \mu) = \frac{1}{\sigma}\left[1 + K\left(\frac{X-\mu}{\sigma}\right)\right]^{-1-\frac{1}{K}} exp\left\{-\left[1 + K\left(\frac{X-\mu}{\sigma}\right)\right]^{-\frac{1}{K}}\right\} \tag{4.3}$$

The shape, scale and location of the function are defined by the three parameters $K \in [-\infty, \infty]$, $\sigma \in [0, \infty]$ and $\mu \in [-\infty, \infty]$ respectively. X is an array of the times at which the function is evaluated. For further details see the MATLAB help [18]. The chosen parameters for the $gevpdf$

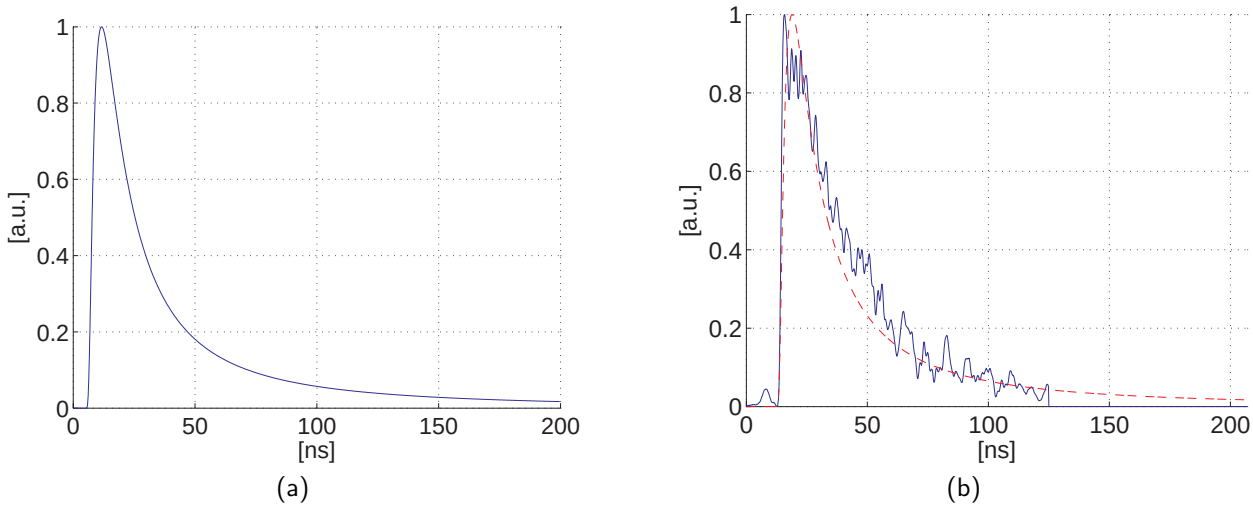

Figure 4.15: Generalized extreme value probability density function as the template function for the cross-correlation on the left and the template function (red dashed) in comparison with a GAPD single pulse (see fig. 4.14a) on the right.

function are:

Time Array	X: time array with a resolution of 0.125 ns per step and a length of 200 ns
Shape parameter	K: 1.2
Scale parameter	σ: 170
Location parameter	μ: 180

4.3.2 MATLAB code of the reconstruction algorithm

The MATLAB lines of the reconstruction algorithm are shown in listing 4.1.

Listing 4.1: MATLAB code of the reconstruction algorithm.

```
Input variables:
    SigGAPD, array, contains the simulated or measured GAPD signal
    RefPulse, array,  template function gevpdf(tp,1.2,170,180)

01: for m=1:(length(SigGAPD)-length(RefPulse))
02:     for n=1:length(RefPulse)
03:         avXC(m) = avXC(m) + RefPulse(n) * SigGAPD(n+m,2);   % X-corr
04:     end

05:     if m>6
06:         t = m-3;
07:         XC(m) = 1/16*(avXC(t-3) + 2*avXC(t-2) + 3*avXC(t-1) + ...
            4*avXC(t) + 3*avXC(t+1) + 2*avXC(t+2) + avXC(t+3));
08:     end

09:     if m>8
10:         XC2D(m-2) = (XC(m)-XC(m-1)) - (XC(m-1)-XC(m-2)); % 2. diff
11a:        % XC1D(m-1) = XC(m)-XC(m-1);                     % 1. diff
11b:        % XC2D(m-2) = XC1D(m-1) - XC1D(m-2);             % 2. diff

12:         if XC2D(m-2)>=XC2D(m-3) && XC2D(m-4)>XC2D(m-3)
13:             j = j + 1;
14:             MinAmp2D(j,1) = m-3;
15:             MinAmp2D(j,2) = 500*XC2D(m-3);
16:             if MinAmp2D(j,2)<(Threshold) % Amplitude threshold
17:                 k = k + 1;
18:                 MinPos(k) = MinAmp2D(j,1);     % Pos of found pulses
19:                 MinVal(k) = MinAmp2D(j,2);     % Amp of found pulses
20:             end
21:         end
22:     end
23: end
```

The algorithm starts with the calculation of the cross-correlation defined in formula 4.2 (lines 02..04). A simple smoothing [19] of the cross-correlation (lines 05..08) avoids correlated noise which would have a large impact on the results of the second derivative without giving additional information. In line 10, the second derivative is calculated numerically (lines 11a and 11b would be an alternative with the intermediate calculation of the first derivative). Line 12 looks for minima in the second derivative by comparing three adjacent array values and checking for a smallest middle value. If a minimum is found, then the position (line 14) and the amplitude (line 15) are saved. The amplitude

is multiplied by a factor of 500 since the second derivative of the cross-correlation tends to have very small values that could be truncated in the further processing (loss of precision). For an FPGA implementation this multiplication should already happen in line 10 to avoid truncation problems. Line 16 sets a threshold on the amplitude that corresponds to a certain number of photons. The smaller this threshold, the higher the efficiency for reconstructing real pulses, but also the larger the number of wrong reconstructed noise pulses. Here, the threshold is set to about 0.6 photons so that pulses greater then 0.6-photons should be reconstructed properly. In line 18 and 19 the position and amplitude values are again saved and would now be ready to be sent to a DAQ (data acquisition). The for loop at the beginning (line 01) is not necessary, if the data flow is continuous.

The results of the reconstruction algorithm for simulated and measured data are described in the next section.

4.4 Algorithm output

Two test signals (fig. 4.16), one measured and one simulated, are analyzed with ADC resolutions of 8 and 12 bits and time sampling rates of 1 and 4 ns. Figures 4.17 and 4.18 show the output of

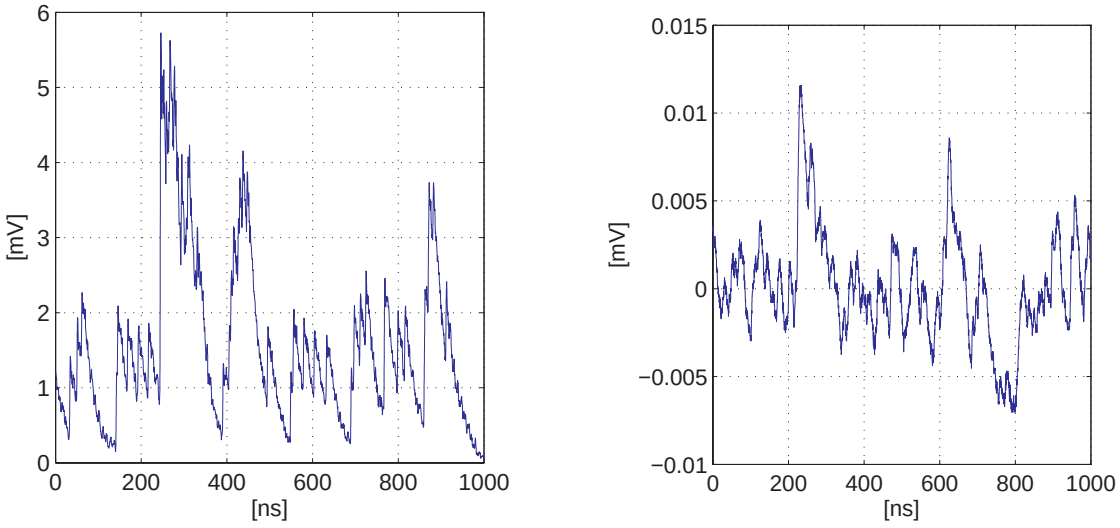

Figure 4.16: (a) Simulated GAPD signal with 60 MHz background rate and a 5 photon pulse at 250 ns. (b) Measured GAPD signal with about 40 MHz background and an estimated 5 photon laser pulse at 220 ns.

the second derivative of the cross-correlation for the simulated signal. Figures 4.19 and 4.20 show the output for the measured signal. The applied threshold is indicated by a red horizontal line. In each figure, the upper plots show the second derivative of the cross-correlation and the lower plots show the discrete points of the second derivative and encircled the points which would be saved as reconstructed pulses. The plots demonstrate that the reconstruction with 8 bits is quite bad compared to the 12 bit sampling. Nevertheless, the simulated shower, as well as the measured laser pulse seem to be reconstructed for both ADC settings.
Figures 4.21 and 4.22 show the reconstruction of the simulated signal (fig. 4.16a). The reconstruction

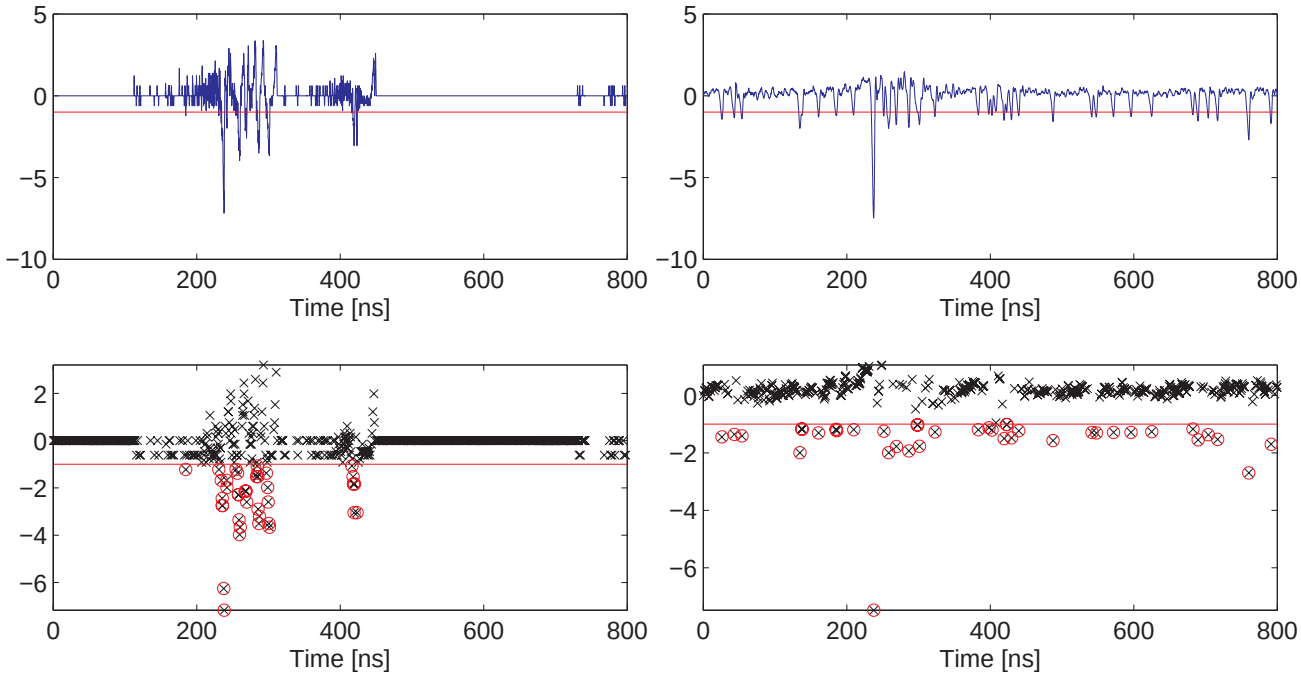

(a) 1 ns, 8 bit sampling.

(b) 1 ns, 12 bit sampling.

Figure 4.17: Second derivative of the cross-correlation for the simulated GAPD signal. Sampling is 1 ns and (a) 8 bits, (b) 12 bits respectively. The red horizontal line marks the threshold described in list 4.1, line 16 (x-axis has arbitrary units). The lower plots show the discrete values of the cross-correlation with reconstructed pulses encircled.

of the measured signal (fig. 4.16b) is shown in figures 4.23 and 4.24. In each figure, the uppermost plots show the simulated or measured signals after the high-pass filter and the ADC. The second row of plots shows all reconstructed pulses without any cleaning and only with the 0.6 photon threshold of the algorithm. Without any further cleaning one would have a lot of wrongly reconstructed pulses. One very strong cleaning criteria that is used is the elimination of reconstructed pulses that are closer together than the sampling time (e.g. if three pulses are reconstructed within a time of 1 ns at a time sampling rate of 1 ns, only the first pulse is taken). A further threshold level on the reconstructed amplitude removes all unphysical < 1 photon pulses. The result is shown in the third row of plots. One can see, that the number of reconstructed pulses decreases dramatically. Further pulses can be eliminated by increasing the amplitude threshold (fourth and fifth rows of plots).
One problem with the reconstruction of the measured signal is that the Photonique preamplifier has an undershoot (see fig. 4.14c), which is not reproduced by the template function. This reduces the correlation between the template and the signal significantly. The adaption of the template (using fig. 4.14c as template) should in principle lead to a better reconstruction. However, it was found that the reconstruction quality does not increase as one can see by comparing the results for the reconstruction with the analytic (fig. 4.23 and 4.24) and the Photonique template (fig. 4.25), respectively. This is probably due to the only rough adjustment of the reconstruction parameters. It should be possible to improve the reconstruction quality by optimizing the reconstruction algorithm (amplitude factors, cleaning settings, etc.) to the new template. Nevertheless, the shower pulses are reconstructed with both templates.

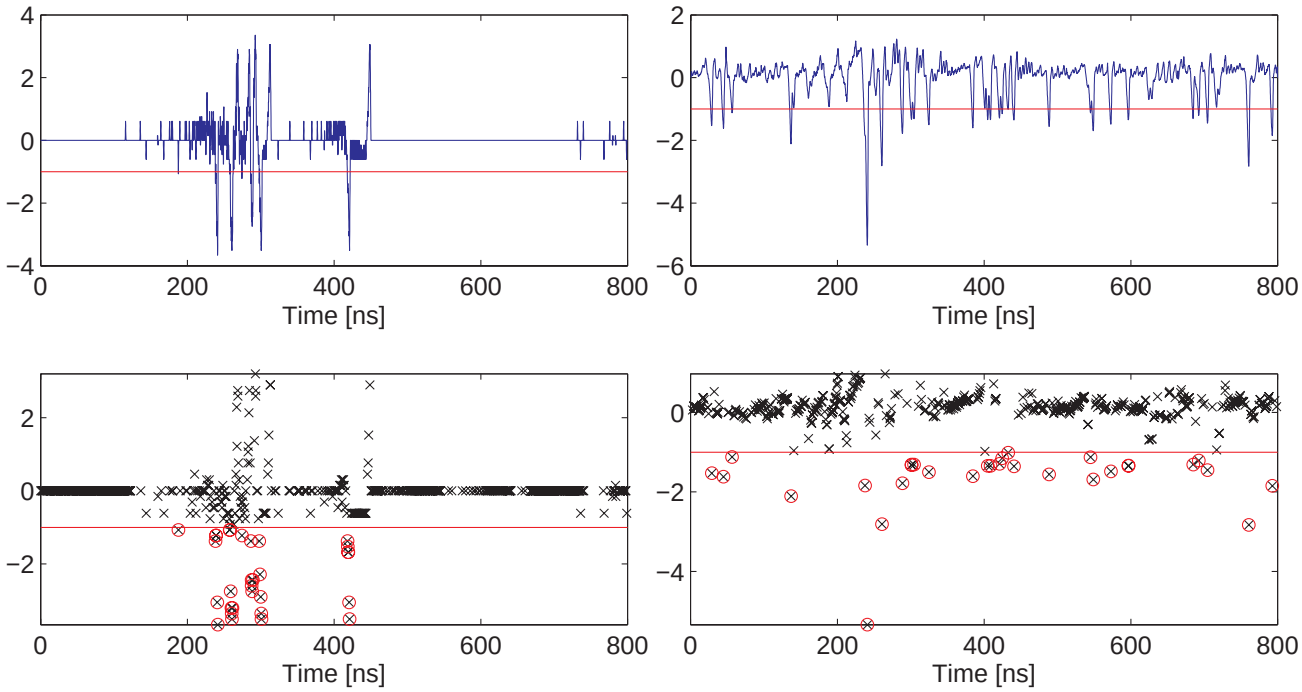

(a) 4 ns, 8 bit sampling rate.

(b) 4 ns, 12 bit sampling rate.

Figure 4.18: Second derivative of the cross-correlation for the simulated GAPD signal. Sampling is 4 ns and (a) 8 bits, (b) 12 bits respectively. The red horizontal line marks the threshold described in list 4.1, line 16 (x-axis has arbitrary units). The lower plots show the discrete values of the cross-correlation with reconstructed pulses encircled.

The results of the reconstruction for different ADC settings are discussed in chapter 5.

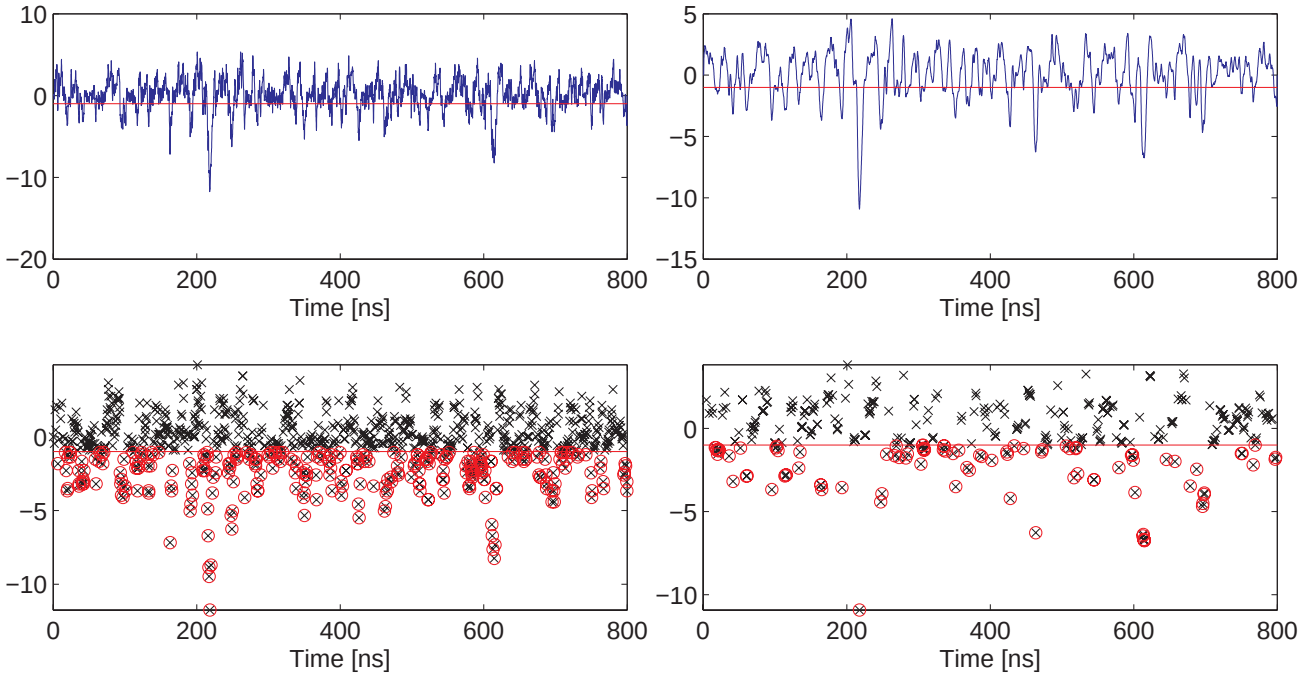

(a) 1 ns, 8 bit sampling rate.

(b) 1 ns, 12 bit sampling rate.

Figure 4.19: Second derivative of the cross-correlation for the measured GAPD signal. Sampling is 1 ns and (a) 8 bits, (b) 12 bits respectively. The red horizontal line marks the threshold described in list 4.1, line 16 (x-axis has arbitrary units). The lower plots show the discrete values of the cross-correlation with reconstructed pulses encircled.

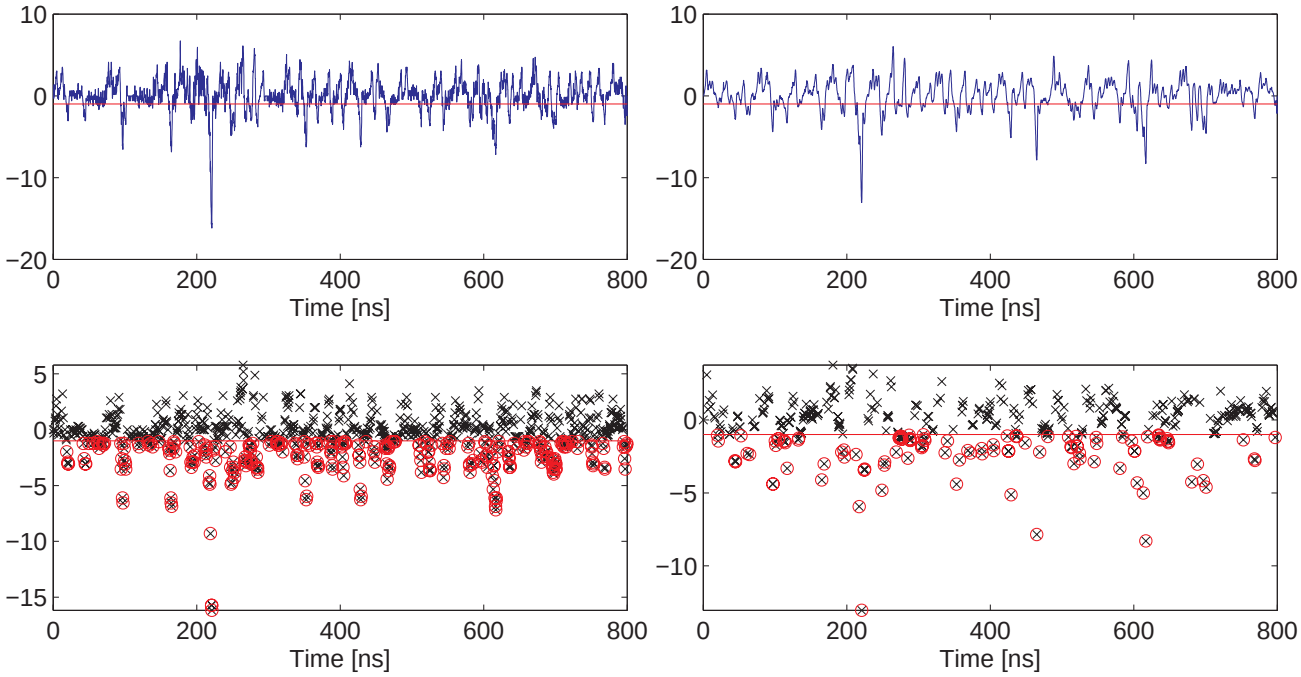

(a) 4 ns, 8 bit sampling rate.

(b) 4 ns, 12 bit sampling rate.

Figure 4.20: Second derivative of the cross-correlation for the measured GAPD signal. Sampling is 4 ns and (a) 8 bit, (b) 12 bit respectively. The red horizontal line marks the threshold described in list 4.1, line 16 (x-axis has arbitrary units). The lower plots show the discrete values of the cross-correlation with reconstructed pulses encircled.

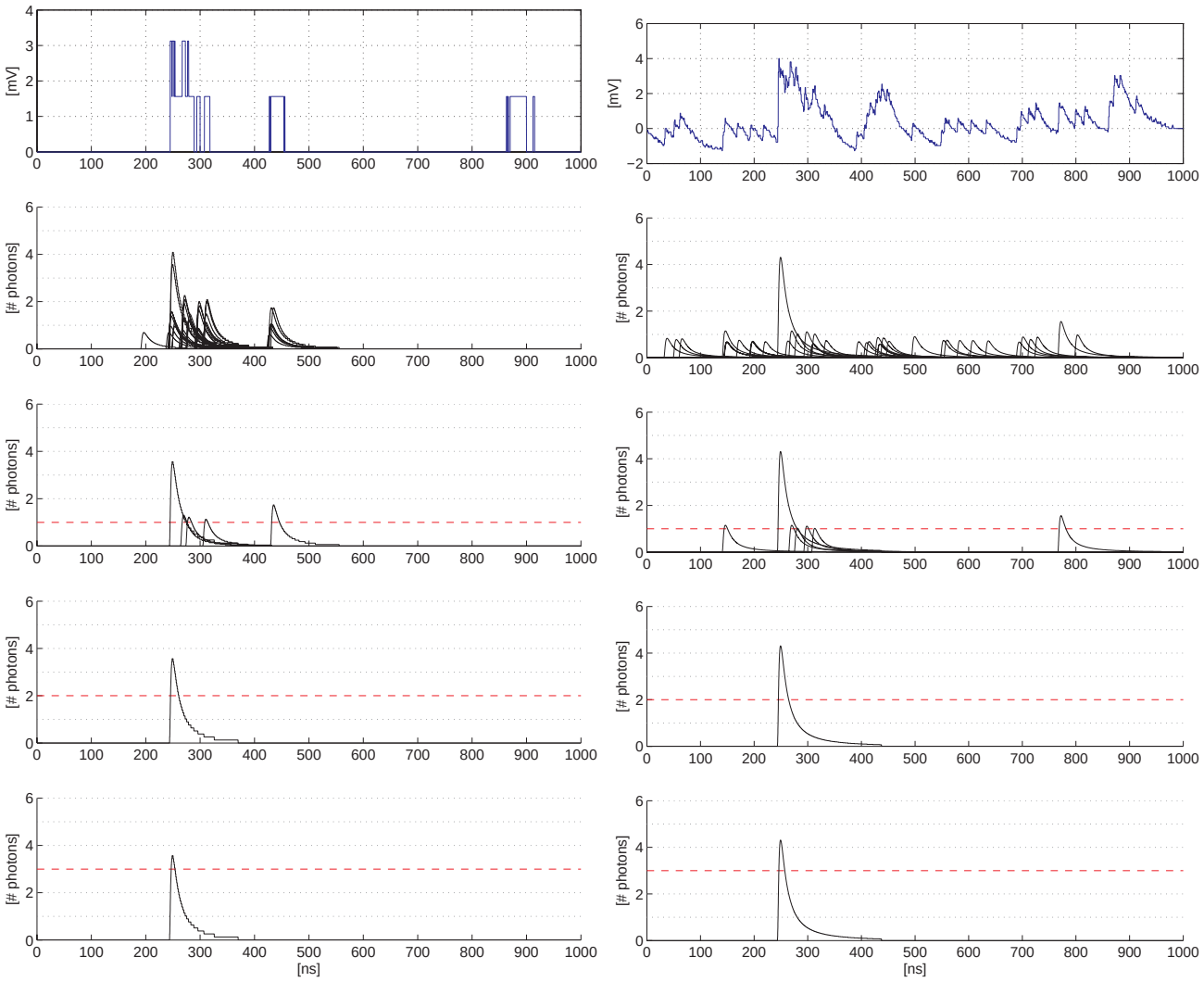

(a) 1 ns, 8 bit sampling rate.

(b) 1 ns, 12 bit sampling rate.

Figure 4.21: Reconstruction of the simulated signal using the pulse time and amplitude information obtained for 1 ns sampling rate and (a) 8 bit, (b) 12 bit resolution. The uppermost plots show the simulated signal after passing the high pass filter and the ADC. The second row of plots show all reconstructed pulses before cleaning. The reconstruction after cleaning and setting a threshold level at 1 photon is shown in the third row of plots. The last two rows of plots show the result with 2 and 3 photon threshold, respectively.

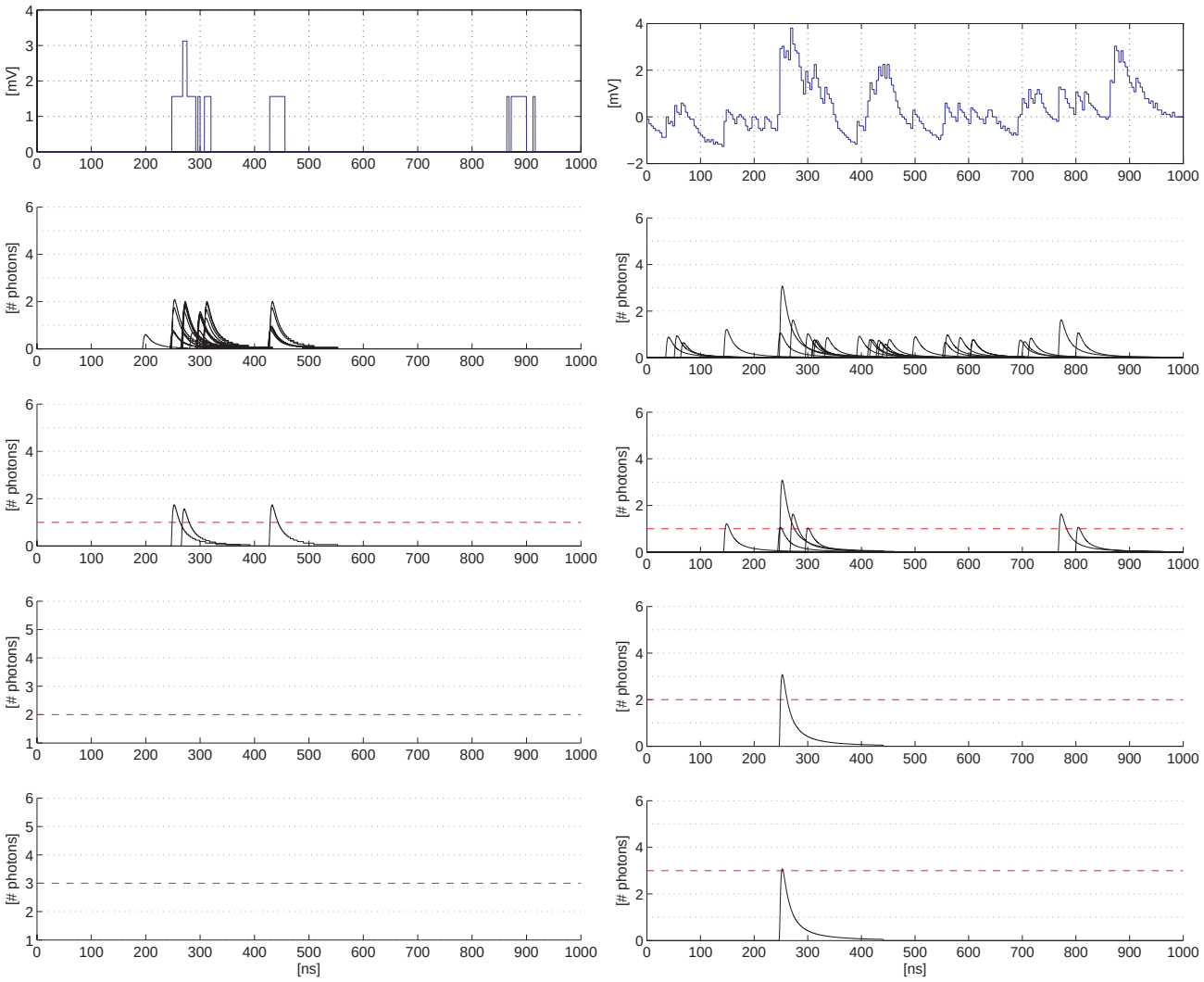

(a) 4 ns, 8 bit sampling rate.

(b) 4 ns, 12 bit sampling rate.

Figure 4.22: Reconstruction of the simulated signal using the pulse time and amplitude information obtained for 4 ns sampling rate and (a) 8 bit, (b) 12 bit resolution. The uppermost plots show the simulated signal after passing the high pass filter and the ADC. The second row of plots show all reconstructed pulses before cleaning. The reconstruction after cleaning and setting a threshold level at 1 photon is shown in the third row of plots. The last two rows of plots show the result with 2 and 3 photon threshold, respectively.

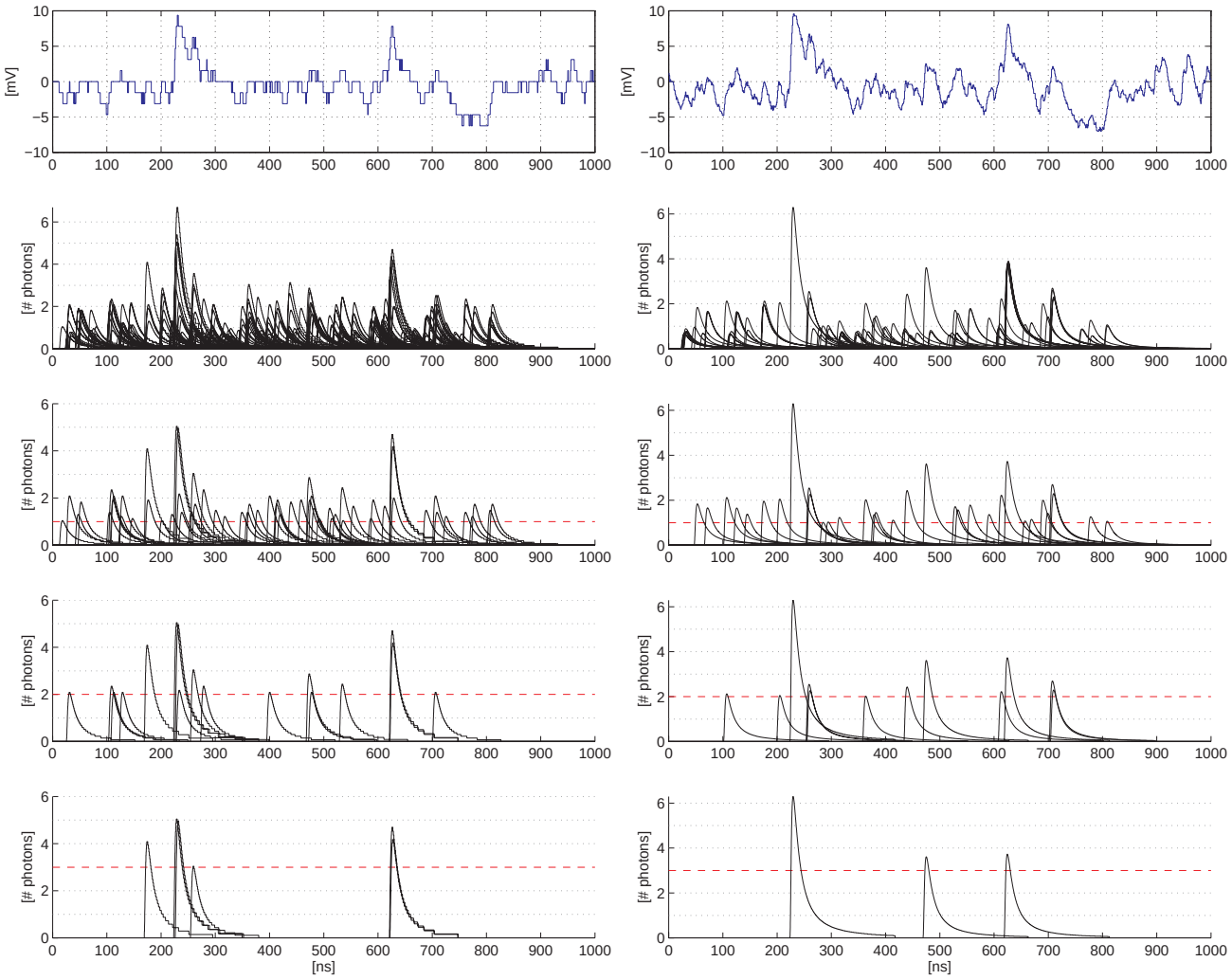

(a) 1 ns, 8 bit sampling rate.

(b) 1 ns, 12 bit sampling rate.

Figure 4.23: Reconstruction of the measured signal using the pulse time and amplitude information obtained for 1 ns sampling rate and (a) 8 bit, (b) 12 bit resolution. The uppermost plots show the simulated signal after passing the high pass filter and the ADC. The second row of plots show all reconstructed pulses before cleaning. The reconstruction after cleaning and setting a threshold level at 1 photon is shown in the third row of plots. The last two rows of plots show the result with 2 and 3 photon threshold, respectively.

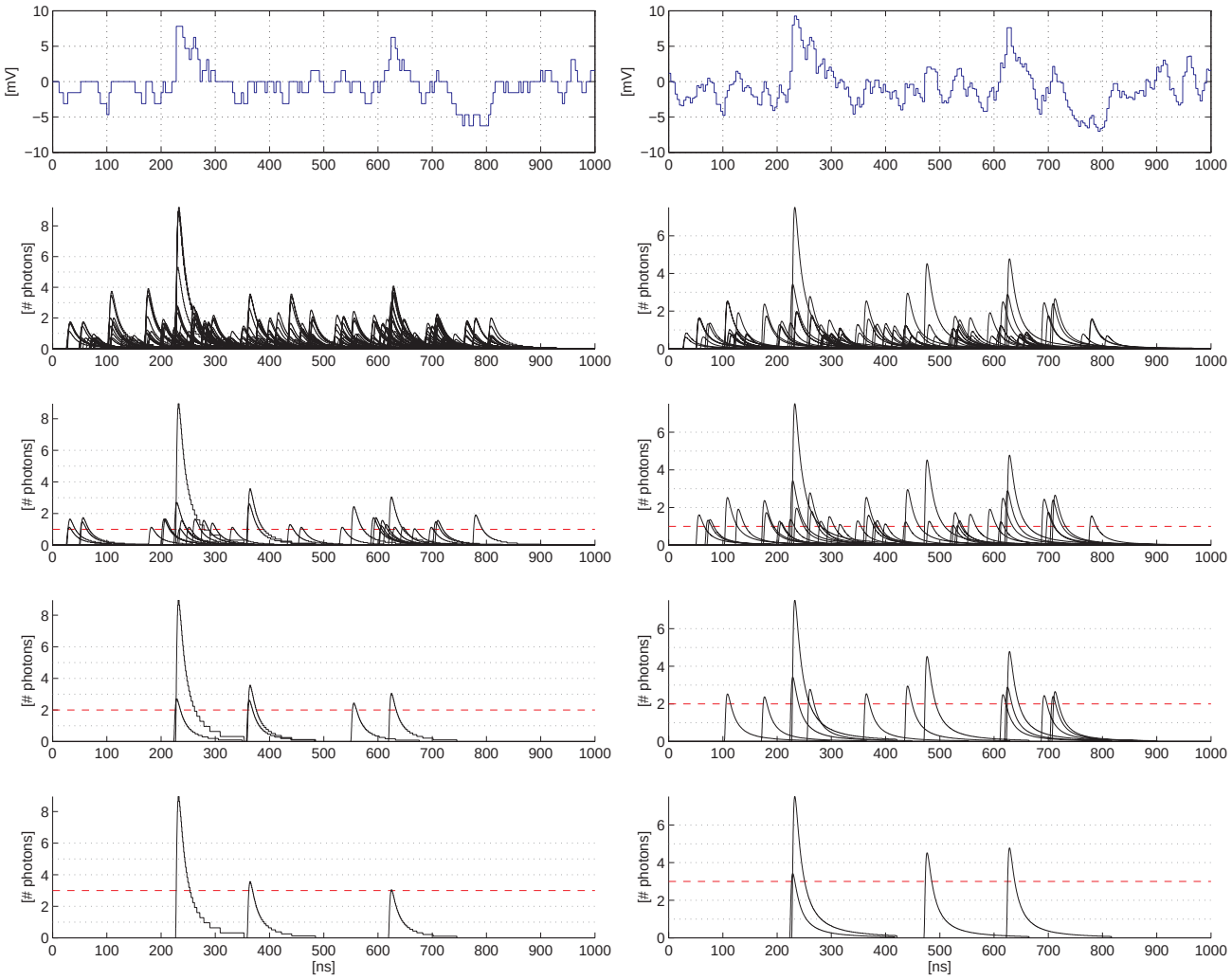

(a) 4 ns, 8 bit sampling rate.

(b) 4 ns, 12 bit sampling rate.

Figure 4.24: Reconstruction of the measured signal using the pulse time and amplitude information obtained for 4 ns sampling rate and (a) 8 bit, (b) 12 bit resolution. The uppermost plots show the simulated signal after passing the high pass filter and the ADC. The second row of plots show all reconstructed pulses before cleaning. The reconstruction after cleaning and setting a threshold level at 1 photon is shown in the third row of plots. The last two rows of plots show the result with 2 and 3 photon threshold, respectively.

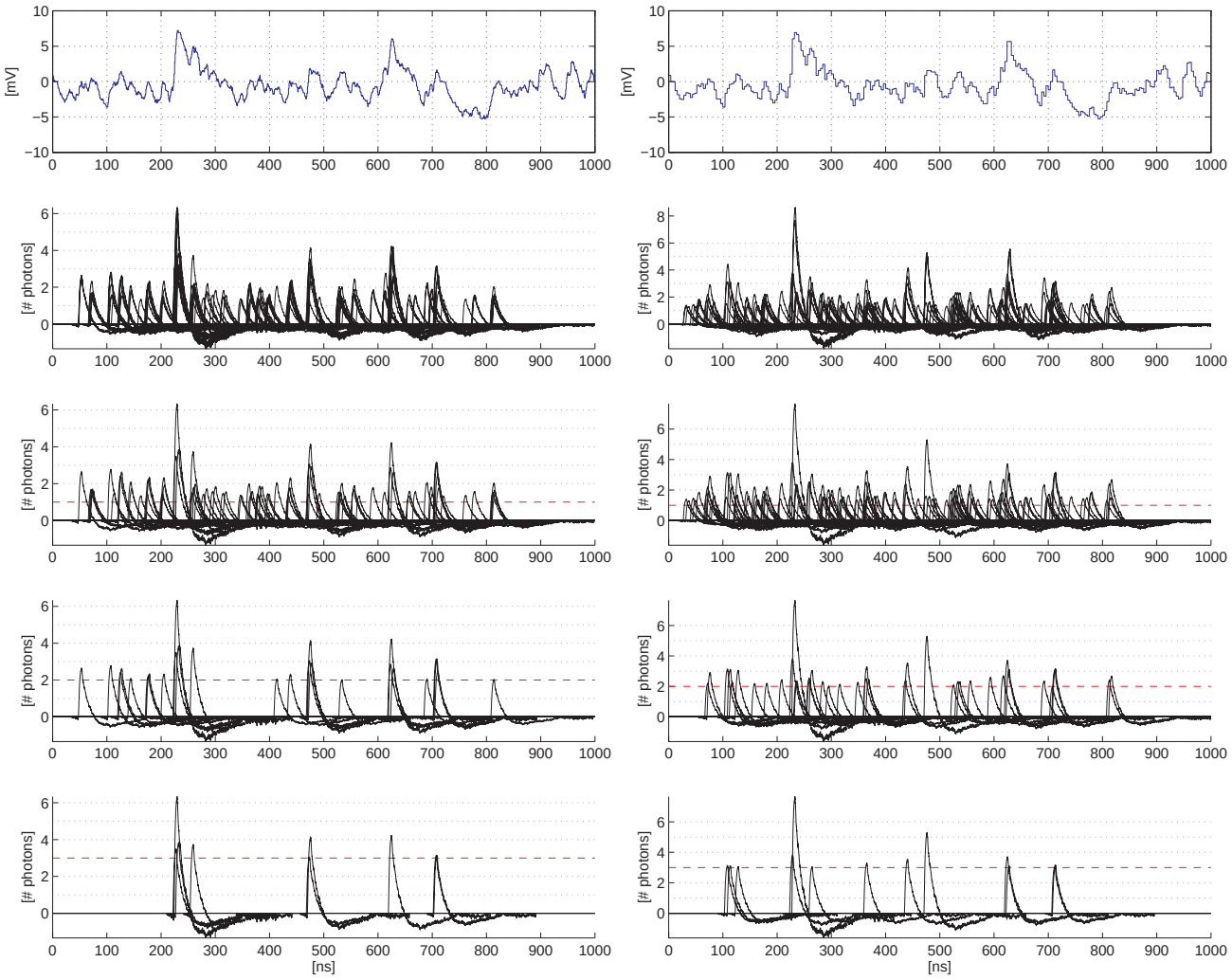

(a) 1 ns, 12 bit sampling rate.

(b) 4 ns, 12 bit sampling rate.

Figure 4.25: Reconstruction of the measured signal with the correct Photonique pulse template (fig. 4.14c) for (a) 1 ns and (b) 4 ns sampling rate and 12 bit resolution. The uppermost plots show the simulated signal after passing the high pass filter and the ADC. The second row of plots show all reconstructed pulses before cleaning. The reconstruction after cleaning and setting a threshold level at 1 photon is shown in the third row of plots. The last two rows of plots show the result with 2 and 3 photon threshold, respectively.

5 Results

The quality of the reconstruction algorithm is defined through its efficiency for reconstructing shower signals, its noise reconstruction rate, and its time and amplitude resolution. To investigate the quality of the reconstruction algorithm for a wide range of parameters a set of 1000 emulated signal samples for each combination of the following parameters was generated.

Sampling time t_s:	1, 2, 3, 4 ns
Sampling resolution A_s:	8, 10, 11, 12 bit
Night sky background frequency f_{BG}:	40, 100, 300, 500, 800, 1000, 2000, 3000 MHz
Cherenkov shower amplitude A_{sim}:	1, 2, 3, 4, 5, 10, 15, 20, 25, 30, 40, 50, 100 photons

Each sample contains two (Cherenkov) shower pulses of the same amplitude at two fixed time positions to improve statistics. Examples of such emulated signals are shown in figure 5.1. One can see a DC offset that increases with increasing night sky background (NSB) frequency and a ripple amplitude that increases from about 5 photons at 40 MHz NSB to about 25 photons at 3000 MHz NSB.
The sampling settings for the ADC (dynamical range of 400 photons) were chosen after the aspects discussed in section 4.2.3. A NSB frequency of 40 MHz corresponds to a dark moonless night whereas an NSB frequency of 3000 MHz relates to a full moon night. The Cherenkov shower amplitude corresponds to a range of several tens GeV to a few TeV gamma-rays.
The photons within an emulated shower have no time spread as they would have in reality (few nano seconds). The reconstruction of spread showers should be investigated in a further step or even better with measured data.

The main results concerning efficiency, noise rate and resolution will be discussed in the following sections. All reconstruction quality plots can be found in the appendix B.

5.1 Efficiency

To estimate the reconstruction efficiency for a given generated shower amplitude A_{sim}, a time window with a width of twice the chosen sampling time t_s ($\Delta t = 2t_s$), is placed around the nominal time of each of the two shower pulses and all reconstructed shower pulses within this window are selected. Figure 5.2(a) shows as an example the distribution of reconstructed amplitudes A_{rec} within the time window for $A_{sim} = 20$ photons. Two distinct contributions show up, reconstructed shower pulses with an amplitude around A_{sim} and reconstructed noise with small amplitudes. To suppress the noise, a threshold is applied on the reconstructed amplitudes. The efficiency is then defined as the ratio of the number of reconstructed pulses above this threshold within the time window and the number of

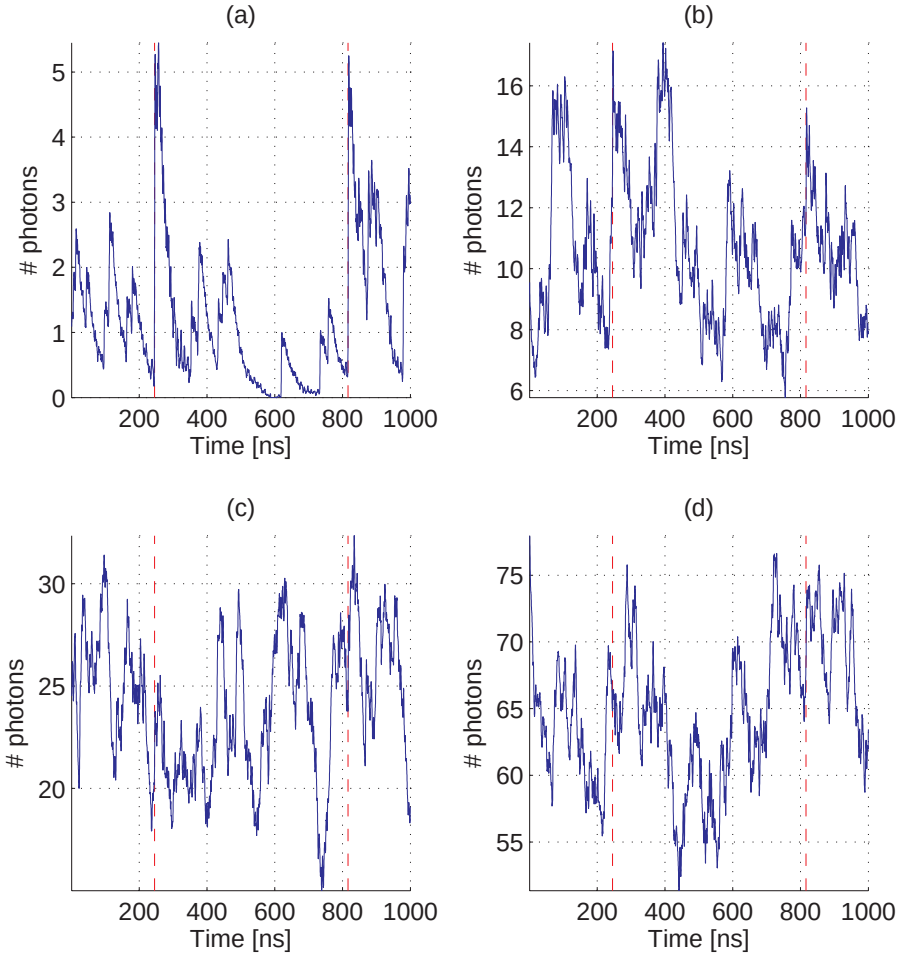

Figure 5.1: Test samples with 40, 400, 1000 and 3000 MHz night sky background, two 5 photon shower pulses at time positions 245 ns and 815 ns (from (a) to (d). The red dashed lines mark the beginning of the shower pulses. It is with already 400 MHz NSB difficult to identify the two shower pulses by eye. The DC base increases with higher NSB frequencies (note that the y-axes have suppressed-zero scales).

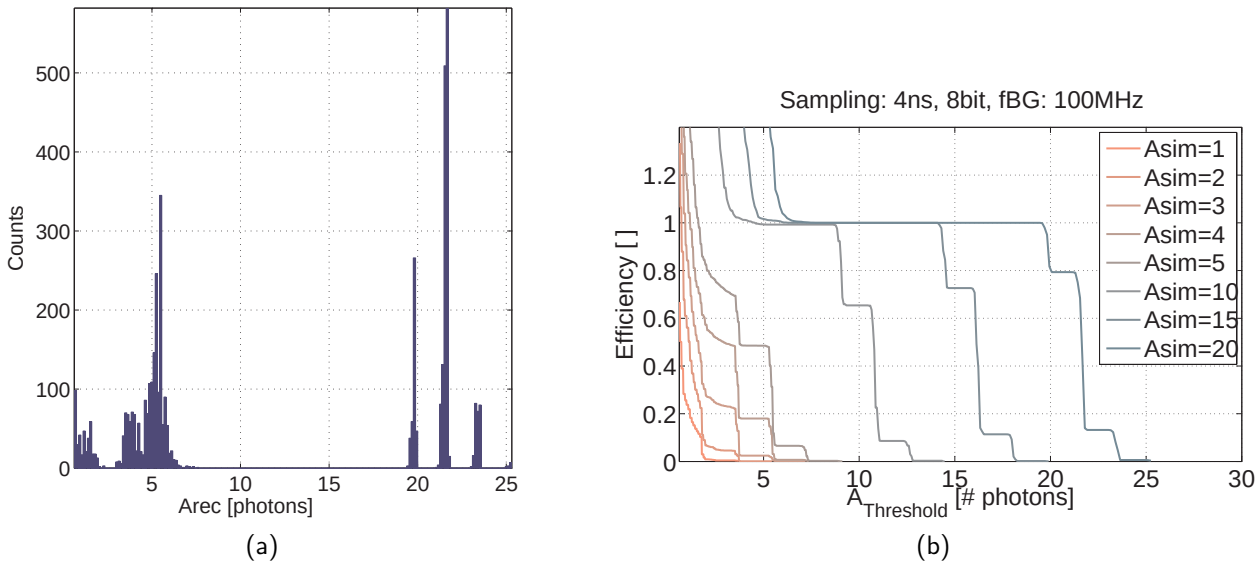

Figure 5.2: Calculation of the efficiency. (a) shows the histogram of the reconstructed amplitudes A_{rec} of all 2000 shower pulses with A_{sim} = 20 photons. (b) shows the reconstruction efficiency as the integration of the histogram values from the right to the left.

all emulated pulses (2·1000).

$$Efficiency = \frac{\#\ reconstructed\ pulses\ in\ time\ window\ \Delta t\ with\ A_{rec} > A_{Threshold}}{\#\ of\ emulated\ pulses} \tag{5.1}$$

Figure 5.2(b) shows as an example the calculated efficiency for one set of parameters. Taking A_{sim} = 20 for illustration, one sees, that for threshold values $A_{Threshold}$ larger than A_{sim} only few reconstructed pulses and therefore a small efficiency occurs. The efficiency reaches 100% just below A_{sim}. For very low thresholds, efficiencies larger than 100% are found. This is an artifact due to additional noise pulses that are reconstructed within the chosen time window.
The threshold value should be chosen high enough to suppress these noise pulses but low enough to obtain full efficiency for shower pulses. The noise rate will be discussed in more detail in the next section.

All efficiency plots are shown in appendix B.1. They show that very bad efficiency is achieved for 8 bit sampling resolution due to the large dynamical amplitude range corresponding to 400 photons. Comparing figures B.1 to B.4 it looks like the efficiency improves with increasing sampling time, but this is an artifact due to the large additional reconstructed noise. Much better results are achieved with a sampling resolution of 10 bits (fig. B.5 to B.8). As expected, the efficiency gets worse for increasing NSB frequency and sampling time and again additional reconstructed noise appears for small $A_{Threshold}$. The 12 bits resolution leads to best results for all parameter settings (fig. B.9 to B.12).

Figure 5.3 shows as an example the best (12 bits) and the worst (8 bits) efficiencies for 1 ns sampling time and 40 MHz NSB frequency.

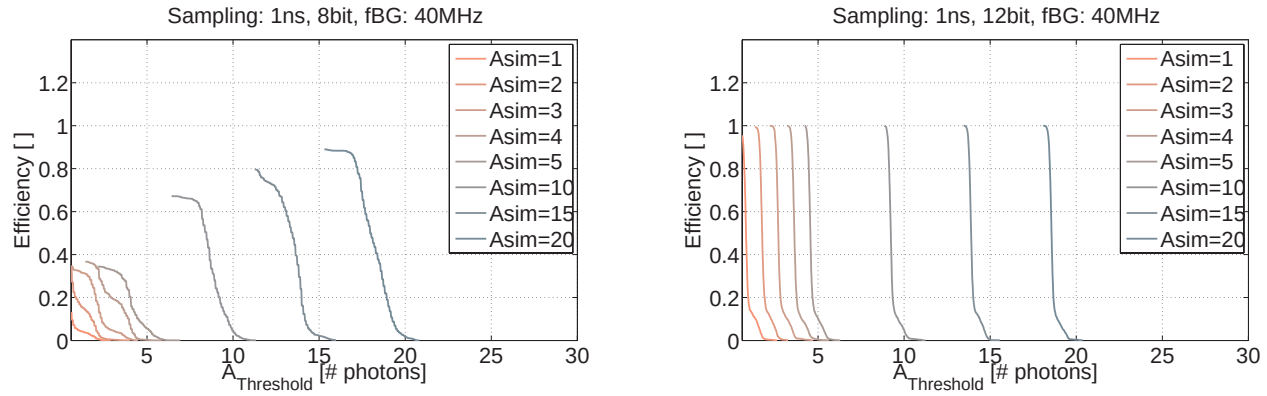

(a) (b)

Figure 5.3: Efficiency for 8 and 12 bits resolution and 1 ns sampling time. The fixed NSB frequency f_{BG} is 40 MHz. The x-axis shows the amplitude threshold value in number of photons. Each curve is plotted for a fixed shower amplitude A_{sim} (left curve $A_{sim} = 1$ photon, right curve $A_{sim} = 20$ photons).

5.2 Noise rate

The noise rate is defined as the number of reconstructed pulses per time unit in the absence of shower pulses. To evaluate the noise rate as a function of all parameter settings, described above, test samples with no showers were generated and analyzed. The reconstructed noise rates are plotted in appendix B.2. For each sample, the noise rate is determined as a function of the threshold $A_{Threshold}$ applied on the reconstruction amplitude. No time window is applied in this case. The noise "efficiency" (noise retention) is defined as the ratio of the reconstructed noise rate and the simulated NSB rate. It is shown as a function of the applied threshold in appendix B.2, right column. Figures 5.4, 5.5 and 5.6 summarize the noise rate figures, showing the noise rate as a function of the NSB frequency.
The noise rate decreases with increasing resolution. For example, for a NSB frequency of 3000 MHz and 1 ns sampling time, it decreases from about 360 MHz for 8 bits, to 240 MHz for 10 bits, down to 125 MHz for 12 bits. This ratio of about 3:2:1 shows up for all sampling times and thresholds.
Increasing the threshold shows, that only few large reconstructed amplitudes occur. This does not surprise since the probability of perfectly piled-up pulses from a noise source is very small (about 1% over the whole NSB range). Hence an amplitude threshold of 2, 3 and 4 photons will reduce the noise rate by about a factor of 2, 4 and 8.

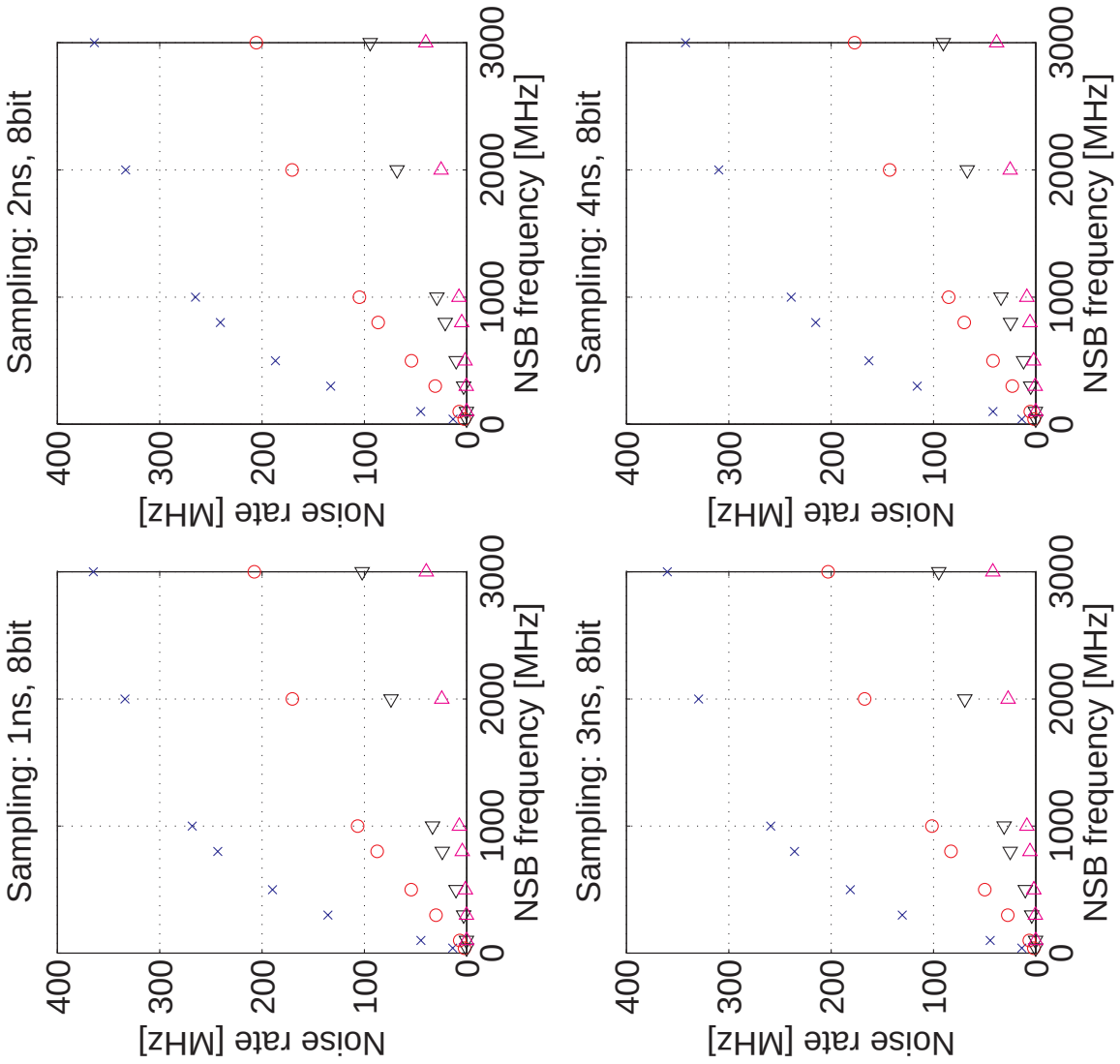

Figure 5.4: Noise rate in function of the background frequency for 8 bit sampling resolution and varying sampling time (1-4 ns). The symbols correspond to an amplitude threshold of: × one, ○ two, ◁ three, ▷ four photons.

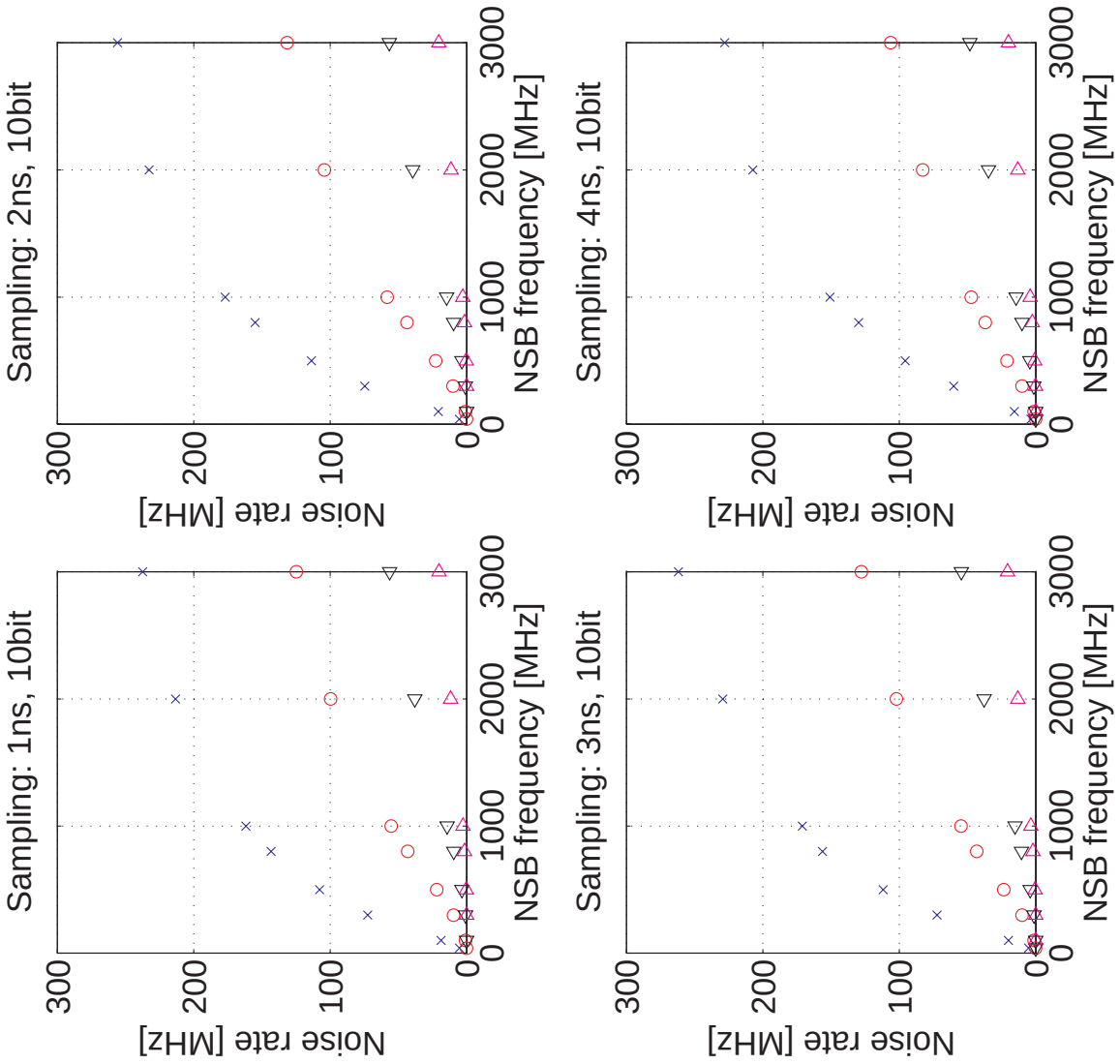

Figure 5.5: Noise rate in function of the background frequency for 10 bit sampling resolution and varying sampling time (1-4 ns). The symbols correspond to an amplitude threshold of: × one, ○ two, ◁ three, ▷ four photons.

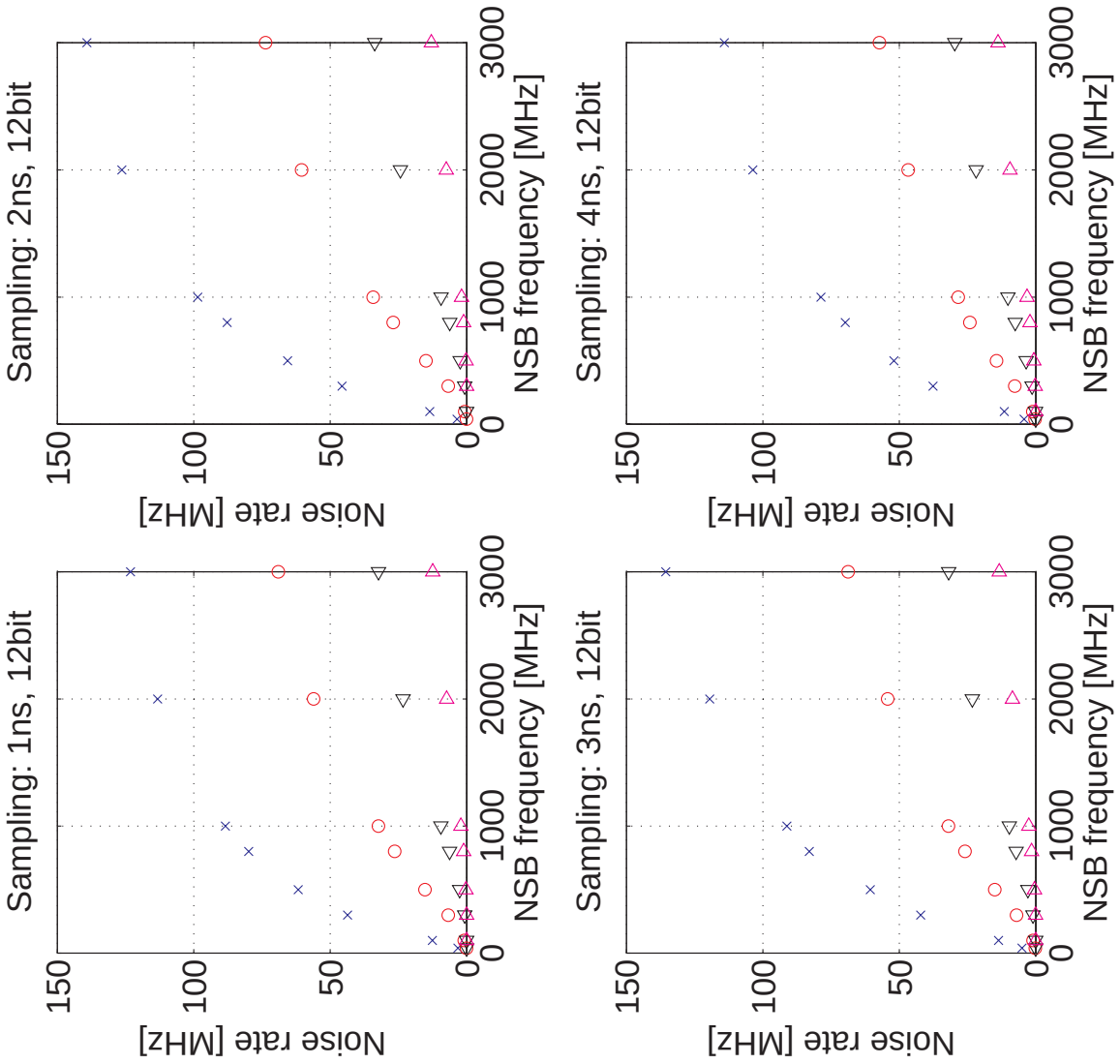

Figure 5.6: Noise rate in function of the background frequency for 12 bit sampling resolution and varying sampling time (1-4 ns). The symbols correspond to an amplitude threshold of: × one, ○ two, ◁ three, ▷ four photons.

5.3 Time and amplitude resolution

The reconstruction resolution is characterized by the mean and the standard deviation of the difference (residual) between the generated shower amplitude A_{sim} and the reconstructed amplitude A_{rec}, or the difference T_{sim} - T_{rec} for the time, respectively. The reconstructed pulses are obtained as described in section 5.1.

5.3.1 Amplitude resolution

The means (left column) and the standard deviations (right column) of the amplitudes differences for given A_{sim} are shown in figures 5.7, 5.8 and 5.9.
Figure 5.7 shows the distribution for $A_{sim} = 3$ photons. No significant differences in the amplitude resolution are observed for the three sampling resolutions and sampling times. The spread of the residuals is small for all settings but the distribution of the means has a large offset for small NSB frequencies. The spread grows whereas the distribution of the means shrinks with increasing NSB. For $A_{sim} = 5$ (fig. 5.8) and $A_{sim} = 10$ (fig. 5.9) the effect of sampling time and sampling resolution in more pronounced. The mean values tend, with a few exceptions, to have a constant offset for the whole range of the NSB frequencies. The reconstructed amplitudes are consistently too small. This offset can be eliminated by adjusting the reconstructed amplitude. The standard deviations improve with increasing sampling resolution and with decreasing sampling time.

Appendix B.3 shows histograms of the amplitude residuals for each parameter setting and plots of the amplitude residuals versus NSB frequency. These figures are not discussed here since their information is contained in the mean and standard deviation figures shown in the next sections.

5.3.2 Time resolution

The means (left column) and the standard deviations (right column) of the time differences for given A_{sim} are shown in figures 5.10, 5.11 and 5.12, respectively.

An excellent time resolution within the sampling time precision is achieved with the cross-correlation for all parameter settings. Mean values close to zero with small standard deviations are found especially for the 1 ns sampling time. Standard deviations lead to increase with increasing NSB frequency. For 8 bits and 10 bits resolution, they do not change for $A_{sim} = 3$ to $A_{sim} = 10$. For 12 bits resolution, standard deviations decrease with increasing A_{sim}.

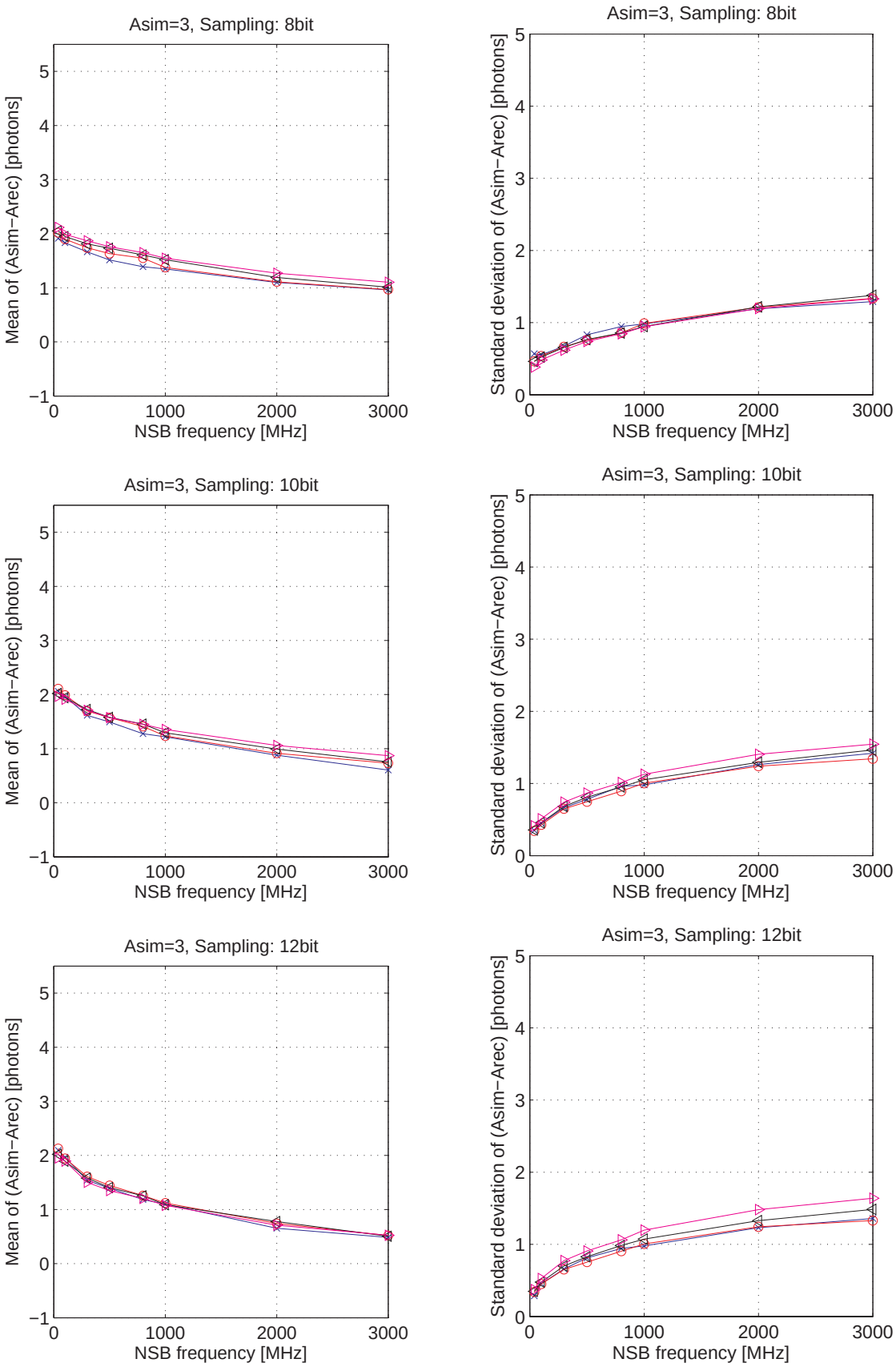

Figure 5.7: Mean (left column) and standard deviation (right column) of the amplitude difference $A_{sim} - A_{rec}$ for fixed $A_{sim} = 3$ photons. The resolution is 8, 10 and 12 bits and the symbols correspond to the sampling times: $\times$ 1 ns, $\circ$ 2 ns, $\triangleleft$ 3 ns, $\triangleright$ 4 ns.

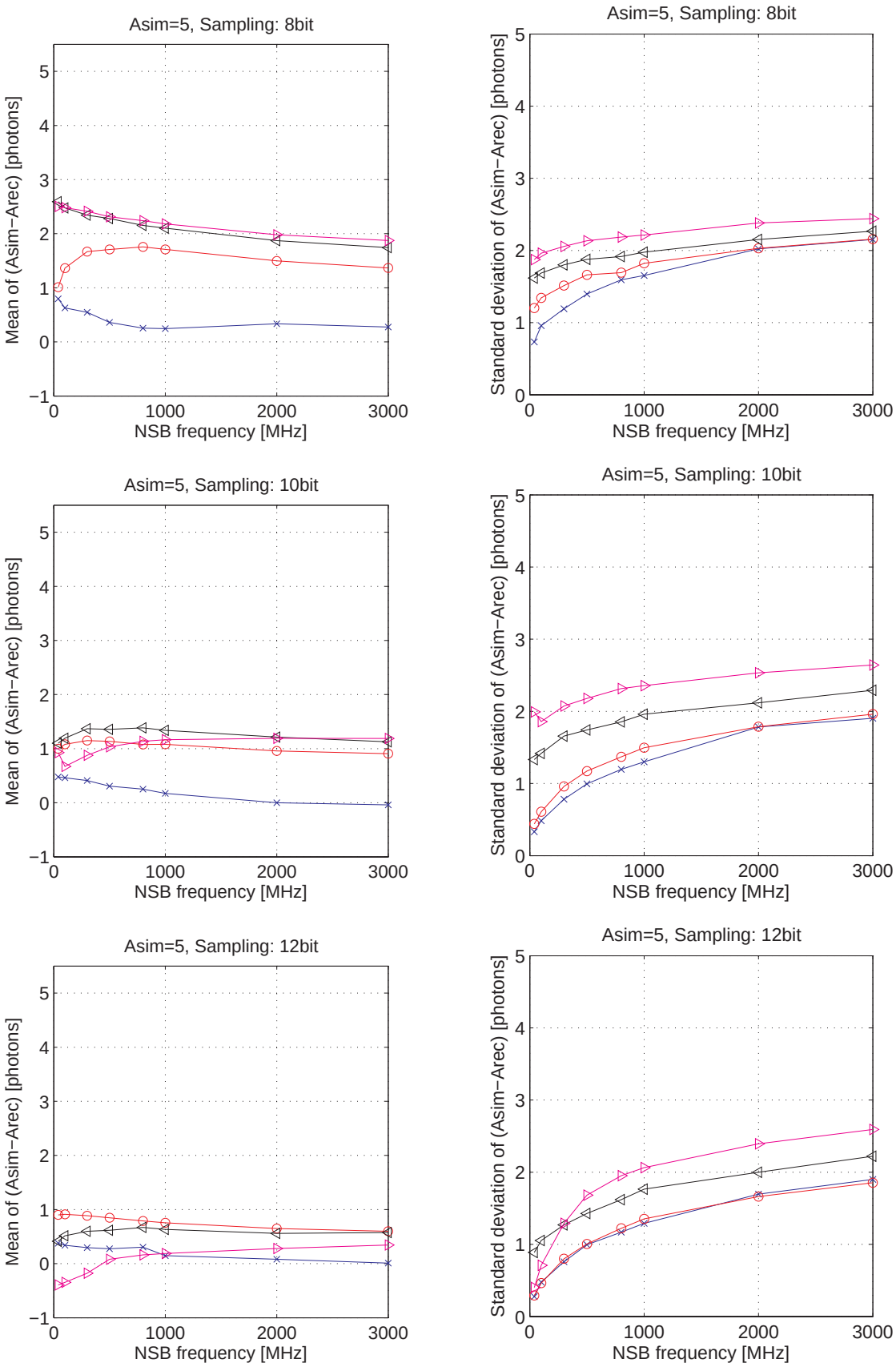

Figure 5.8: Mean (left column) and standard deviation (right column) of the amplitude difference $A_{sim} - A_{rec}$ for fixed $A_{sim} = 5$ photons. The resolution is 8, 10 and 12 bits and the symbols correspond to the sampling times: $\times$ 1 ns, $\circ$ 2 ns, $\triangleleft$ 3 ns, $\triangleright$ 4 ns.

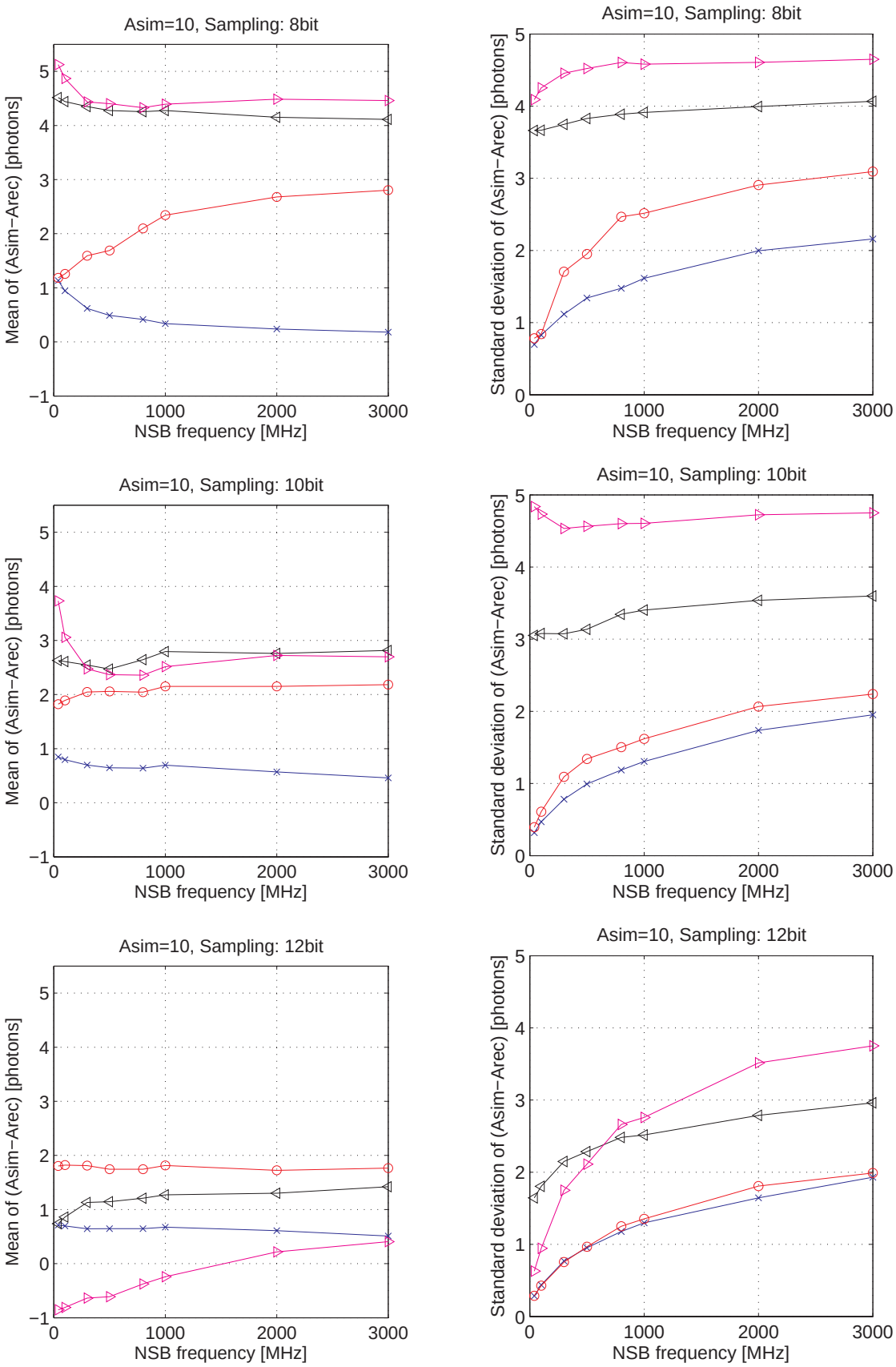

Figure 5.9: Mean (left column) and standard deviation (right column) of the amplitude difference $A_{sim} - A_{rec}$ for fixed $A_{sim} = 10$ photons. The resolution is 8, 10 and 12 bits and the symbols correspond to the sampling times: $\times$ 1 ns, $\circ$ 2 ns, $\triangleleft$ 3 ns, $\triangleright$ 4 ns.

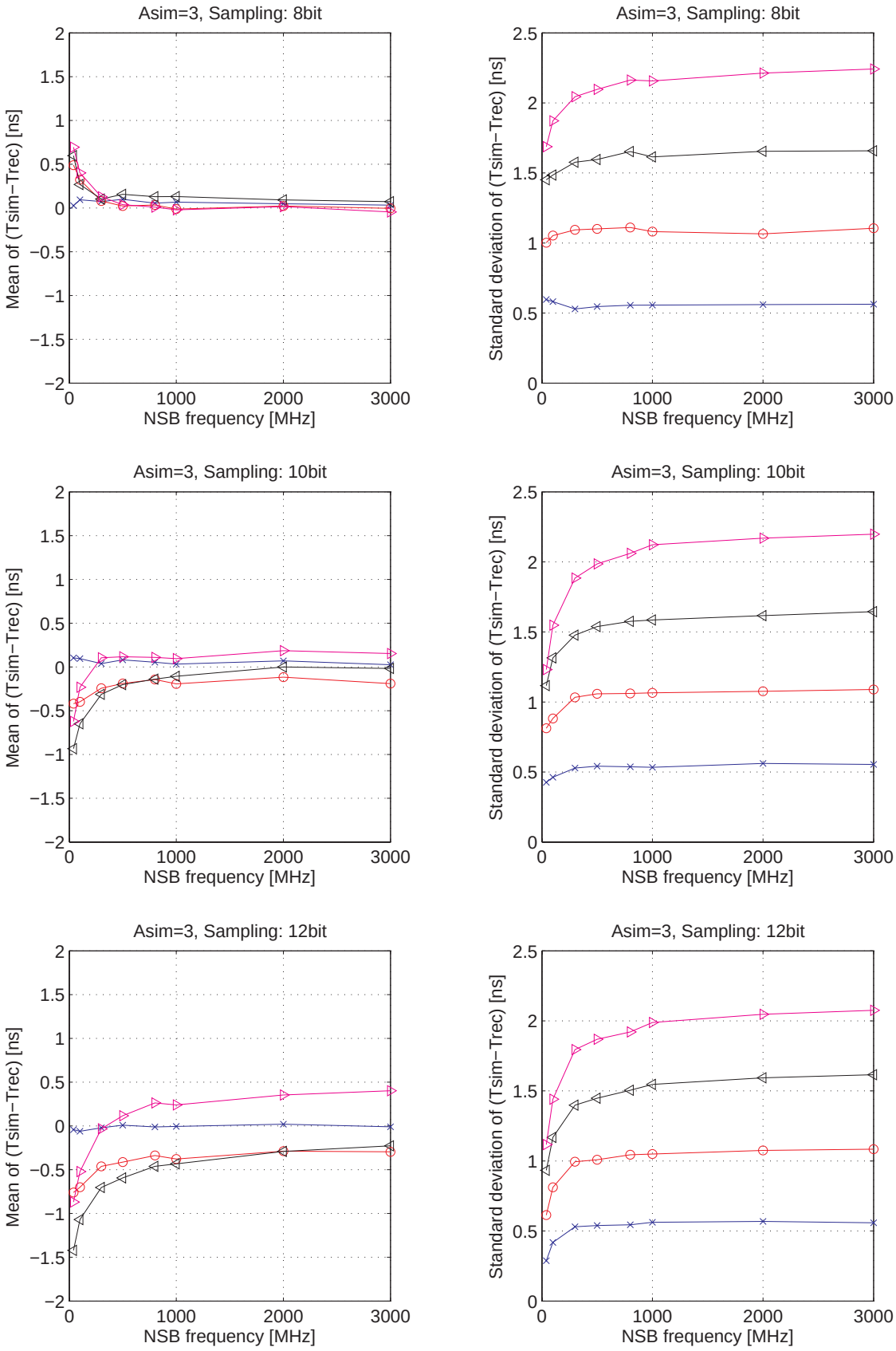

Figure 5.10: Mean (left column) and standard deviation (right column) of the time difference $T_{sim} - T_{rec}$ for fixed $A_{sim} = 3$ photons. The resolution is 8, 10 and 12 bits and the symbols correspond to the sampling times: $\times$ 1 ns, $\circ$ 2 ns, $\triangleleft$ 3 ns, $\triangleright$ 4 ns.

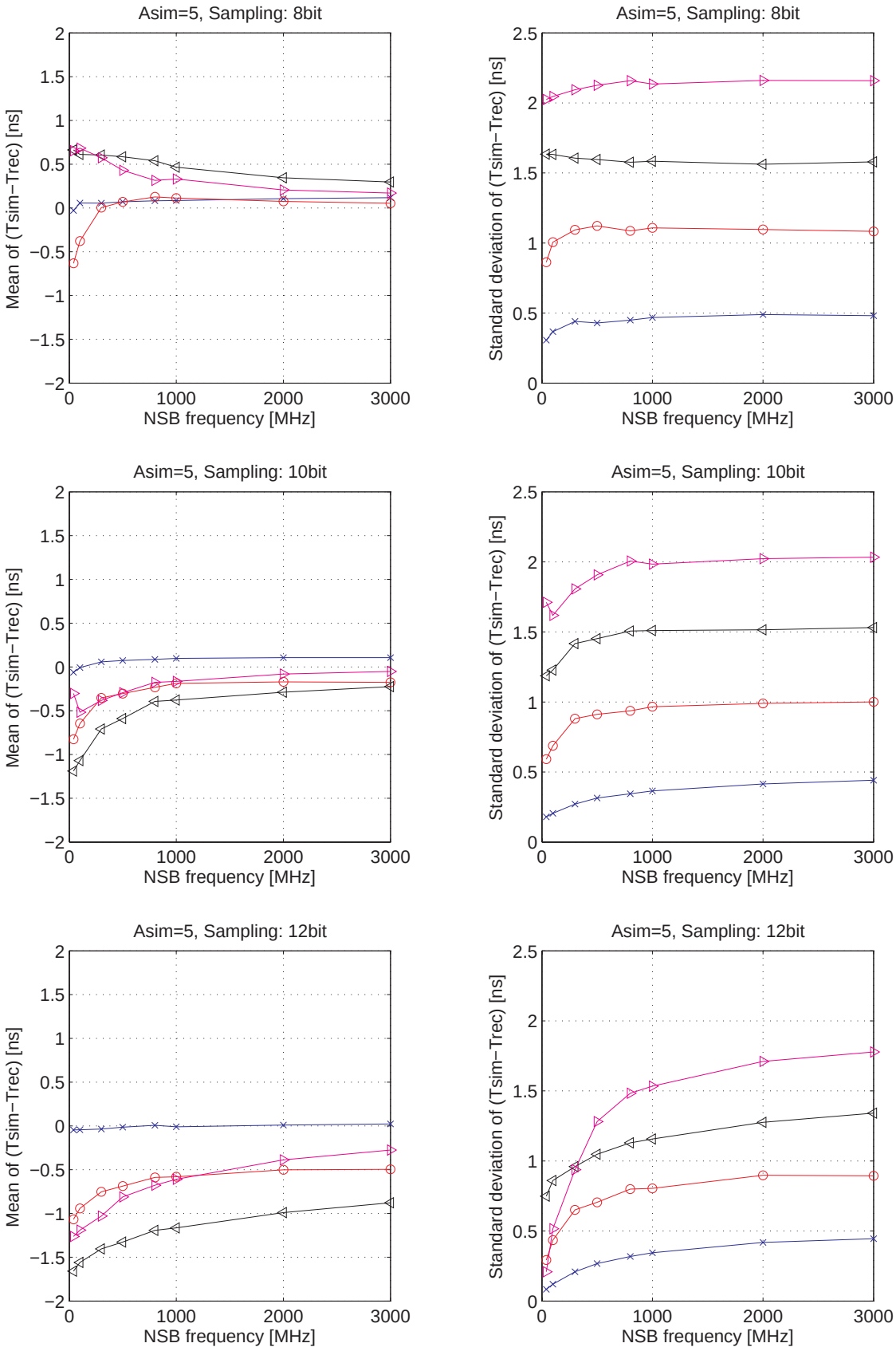

Figure 5.11: Mean (left column) and standard deviation (right column) of the time difference $T_{sim} - T_{rec}$ for fixed $A_{sim} = 5$ photons. The resolution is 8, 10 and 12 bits and the symbols correspond to the sampling times: $\times$ 1 ns, $\circ$ 2 ns, $\triangleleft$ 3 ns, $\triangleright$ 4 ns.

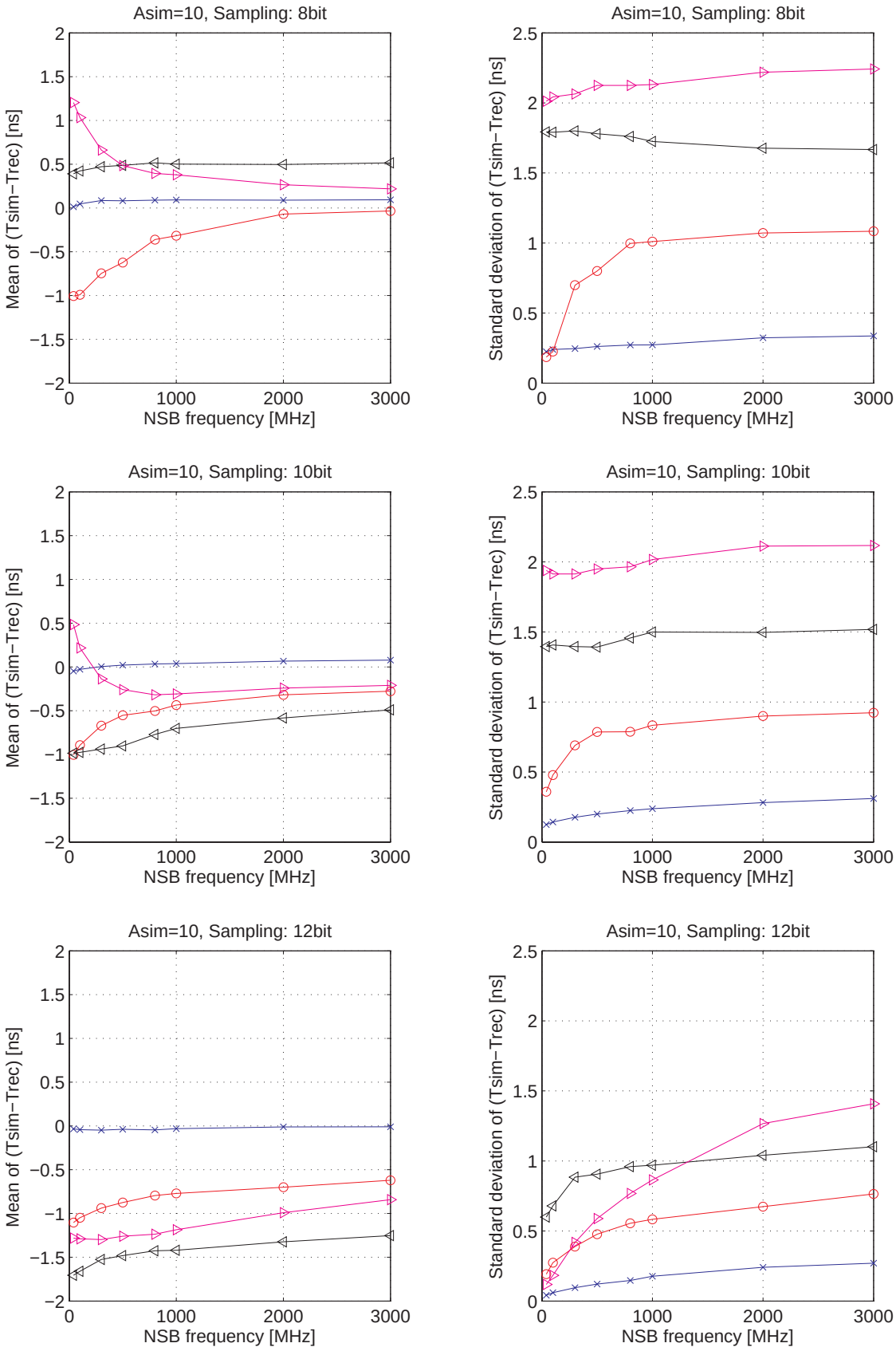

Figure 5.12: Mean (left column) and standard deviation (right column) of the time difference $T_{sim} - T_{rec}$ for fixed $A_{sim} = 10$ photons. The resolution is 8, 10 and 12 bits and the symbols correspond to the sampling times: $\times$ 1 ns, $\circ$ 2 ns, $\triangleleft$ 3 ns, $\triangleright$ 4 ns.

6 Conclusions

In this thesis a triggerless and online reconstruction method based on the second derivative of the cross-correlation with a template function is developed for the reconstruction of shower signals of a Cherenkov telescope. The algorithm was tested on measured and emulated data samples. The measurements were gained with a test setup consisting of a light pulser and a Geiger mode Avalanche Photo Diode (GAPD). The emulated samples were produced with realistic parameters for night sky background frequency (40 - 3000 MHz), shower pulse amplitudes (1 - 100 photons) and ADC values (1 - 4 ns sampling time and 8, 10, 11, 12 bits resolution). The performance of the algorithm is shown by its reconstruction efficiency, its noise rate and the amplitude and time resolution.

The results show, that the cross-correlation algorithm provides good reconstruction efficiencies for 10 and 12 bits ADC sampling resolutions for almost all emulated shower and night sky background settings. Although a high sampling resolution and sampling rate are preferable for the reconstruction, lower values are desired for a hardware implementation due to the high power consumption and costs of high-speed ADC. These studies indicate that for a dynamical amplitude range of 400 photons an ADC with a sampling resolution of 9 or 10 bits and a sampling rate larger than 300 MHz should cover the needs. A good reconstruction efficiency for pulse heights larger then 5 photons and noise rate below 100 kHz for small night sky background frequencies (around 100 MHz) and 5 MHz for large night sky background frequencies (around 3000 MHz) should be achievable.

The continuation of this work should include three major investigations:
- Optimizing the dynamical range of the ADC for the 8 bits resolution to get a better conclusion about the reconstruction power.
- Include the FPGA clock in the simulation. The FPGA clock determines the cross-correlation resolution and will have an influence on the reconstruction efficiency. Varying the clock frequency will show, if the algorithm can work in an FPGA and where the clock limits will be.
- Apply the algorithm to reconstruct real data from a Cherenkov telescope. Only the comparison of the results of the algorithm with the results of the currently used reconstruction software will show, if the developed algorithm really works for the purpose needed.

Finally, the presented reconstruction algorithm is not limited to Cherenkov shower or GAPD applications. It could be used for any signal reconstruction in continuous data streams where trigger conditions are hard to define. The algorithm can also be applied for offline reconstructions.

7 Acknowledgments

I want to thank Achim Vollhardt for a great supervision, for help in almost any situation, for the prove reading of this paper and for a very good lab time. Special thanks go to Olaf Steinkamp for his inputs and for the very interesting talks as well for his prove reading of the paper. Many thanks go to Professor Ulrich Straumann for his great support but especially for the opportunity to join his group and letting me proceed freely. A big thank goes to Stefan Steiner for his support in all mechanics related questions. I also want to thank Ben Huber for the lively discussions and for his inputs. Thanks also go to the whole UZH LHCb group.

A Winston cones for a prototype GAPD camera

GAPDs have a small active area as seen in chapter 3 and a slightly larger ceramic frame that increases the mounting area and therefore reduces the light collection efficiency of the camera. Light concentrators mounted in front of the GAPDs improve the light collection and therefore increase the detection efficiency. Such a light concentrator is the presented Winston cone.

A Winston cone is a nonimaging solid light-collection device with parabolic shape, large entrance aperture and smaller exit aperture. The parabola is tilted so that its focus lies on the edge of the exit aperture. This shape leads by definition to only one internal reflexion (see blue ray fig. A.1). Light rays entering at an angle $\alpha > 20°$ will be reflected several times and eventually leave through the entrance window. The cone concentrates therefore only light with a small incident angle $\alpha < 20°$ dependent on the cones construction. Our light collectors deviate from the standard Winston

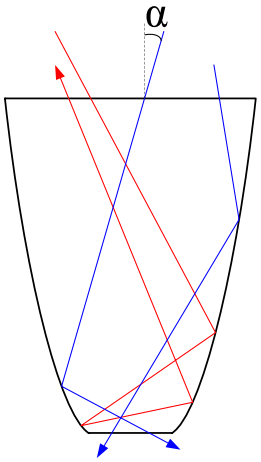

Figure A.1: Winston cone principle. The blue rays have a small enough incident angle α and pass the Winston cone with only one reflection. If the incident angle is to big as for the red ray it will be reflected several times until it leaves the cone through its entrance. The Winston cone limits in that way its field of view to about $\alpha \approx 20°$.

cone shape. They were calculated and dimensioned by Isabel Braun from ETH Zurich and were produced by Stefan Steiner UZH. The cones have a hexagonal entrance window to reduce the corner rays compared to a squared entrance window (see [20]) and a square-shaped exit window fitting the active surface of the GAPD chip. Two side walls of the cone are flat and go from one edge of the hexagon to one edge of the square (see fig. A.2 (a) left and right side). The other four edges of the hexagon share pairwise one edge of the square, so walls are parabolic. This shape leads to not one but three reflexions for a passing ray and is more difficult to be produced. Several production

techniques are being discussed and as soon as the proper shape is calculated and simulated a test production will start.

For further information about Winston cones and light collectors in general see e.g. [13].

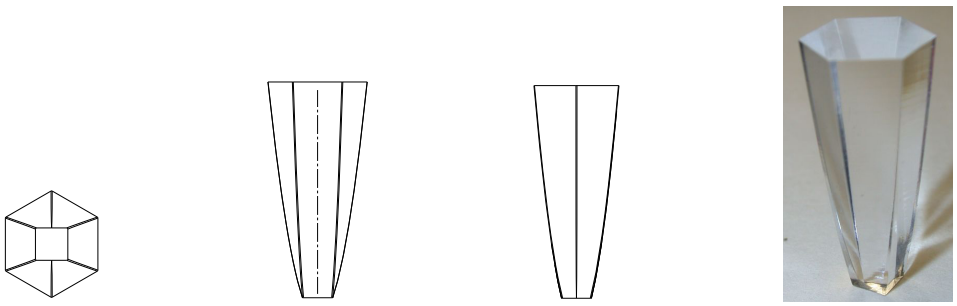

(a) (b) (c) (d)

Figure A.2: (a) Winston cone top view. (b) Side view on the flat face. (c) Side view on the arced face. (d) Photo of a Winston cone produced at UZH.

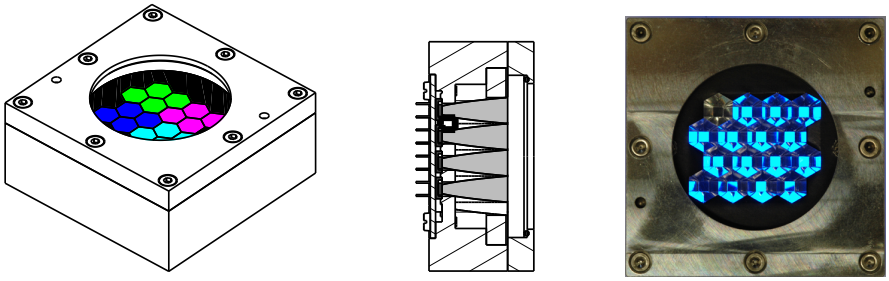

(a) (b) (c)

Figure A.3: (a) Camera frame with installed Winston cones. (b) Sectional drawing through camera frame with from left to right: circuit board with preamplifier and GAPDs, Winston cones (gray), entrance window. (c) Photo of the camera front with back light. The camera is assembled with only one GAPD (left upper corner).

B Reconstruction quality plots

The following sections contain all efficiency and noise reconstruction plots as well as the amplitude residual histograms. The definitions of the efficiency and the noise rate are (see sections 5.1 and 5.2):

Efficiency = ratio of the number of reconstructed pulses above the threshold $A_{Threshold}$ within the time window $\Delta t = \pm t_s$ and the number of all emulated pulses (2·1000).

Noise rate = the number of reconstructed pulses per time unit in the absence of shower pulses.

B.1 Efficiency

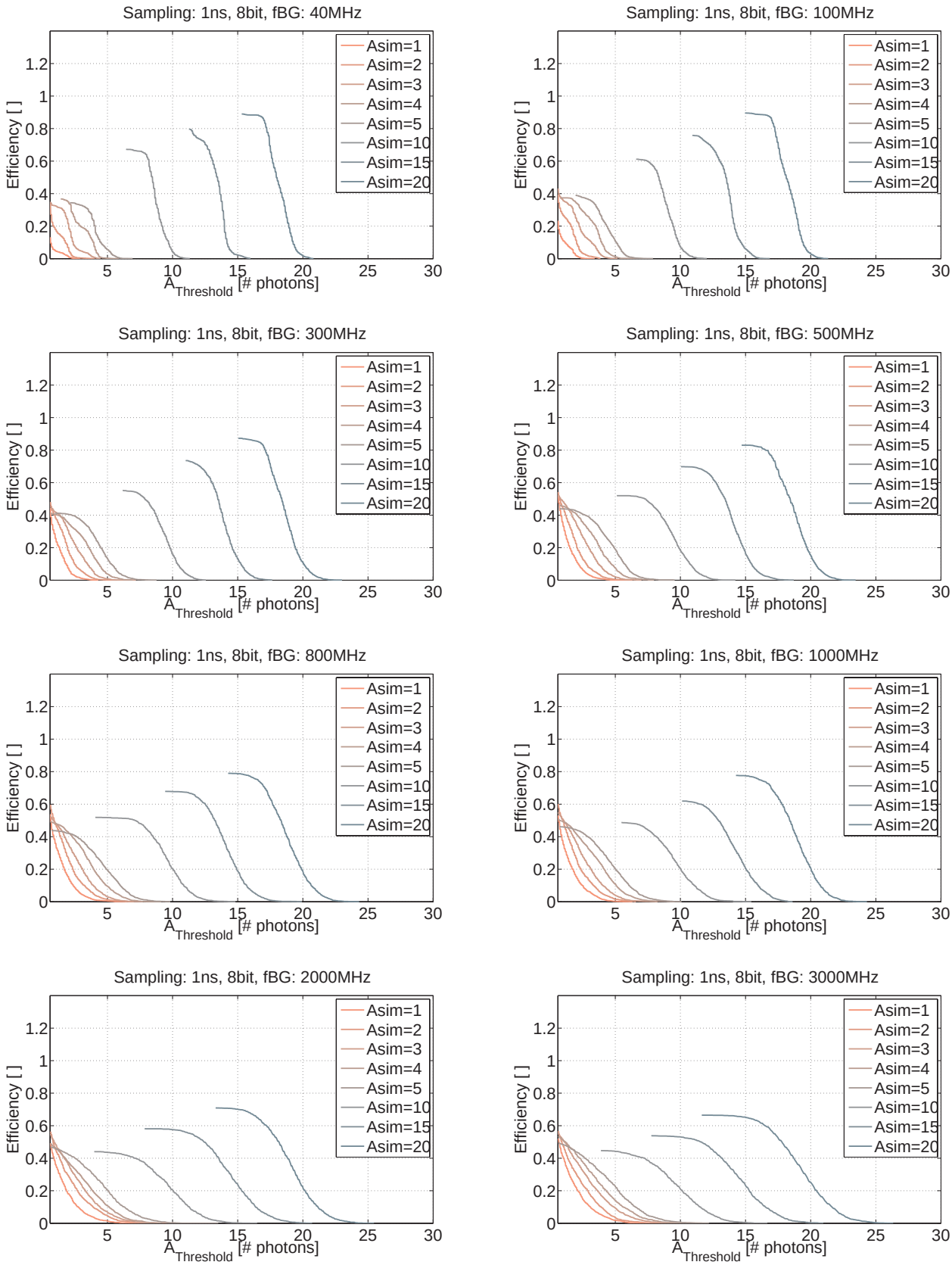

Figure B.1: Efficiency vs. amplitude threshold for 8 bit and 1 ns sampling and NSB frequencies of 40 to 3000 MHz. Each curve has a fixed shower amplitude A_{sim}.

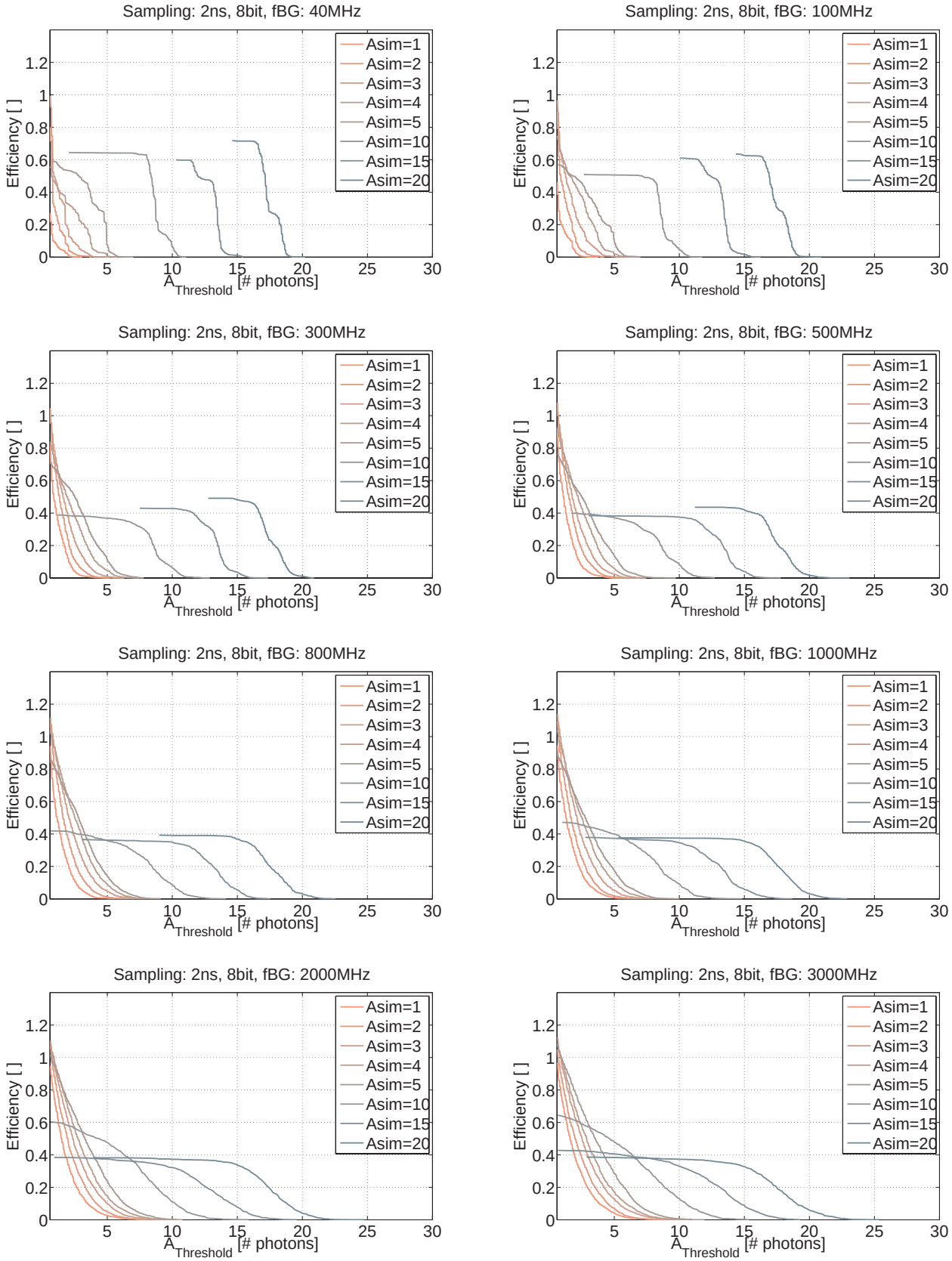

Figure B.2: Efficiency vs. amplitude threshold for 8 bit and 2 ns sampling and NSB frequencies of 40 to 3000 MHz. Each curve has a fixed shower amplitude A_{sim}.

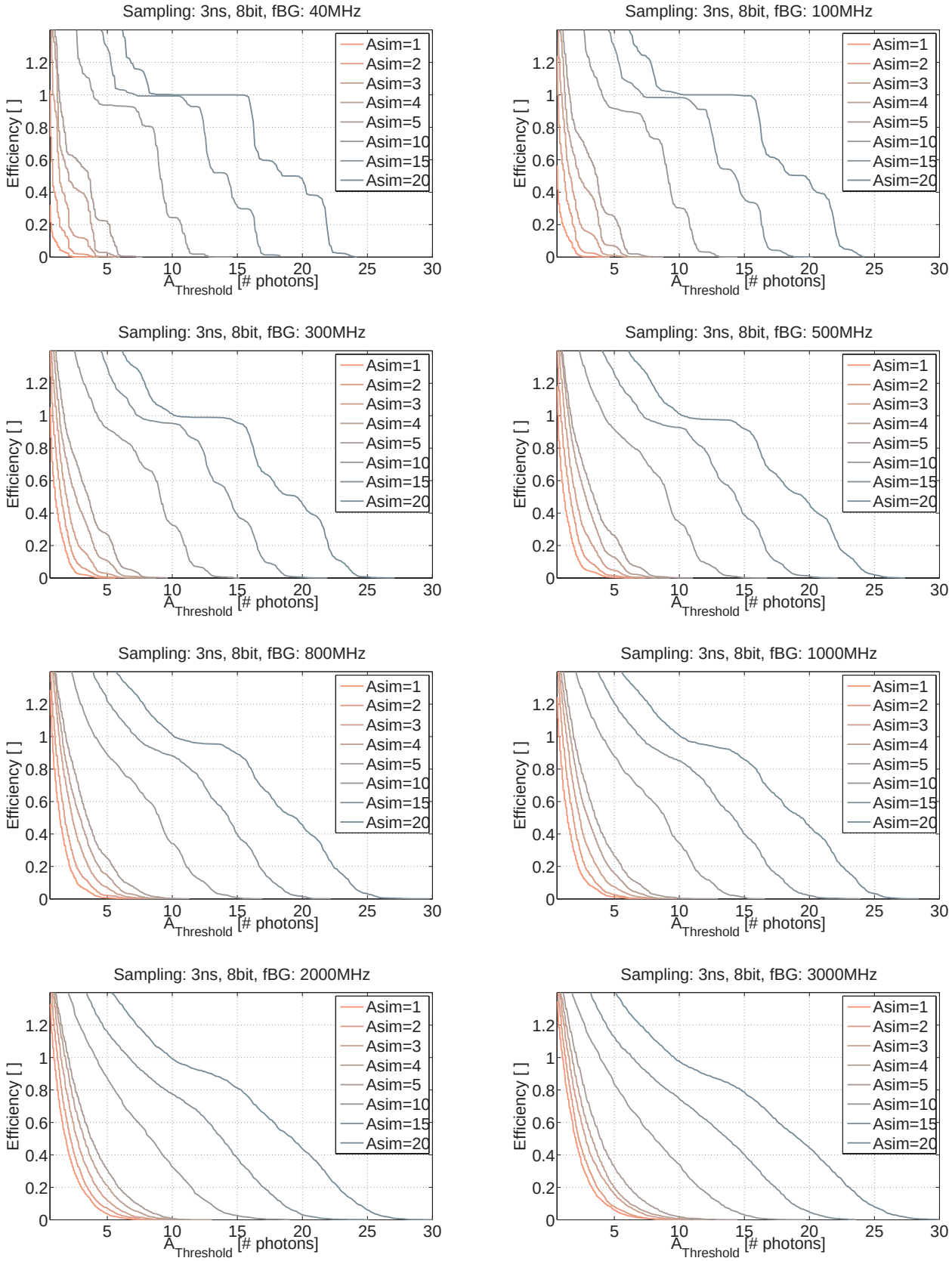

Figure B.3: Efficiency vs. amplitude threshold for 8 bit and 3 ns sampling and NSB frequencies of 40 to 3000 MHz. Each curve has a fixed shower amplitude A_{sim}.

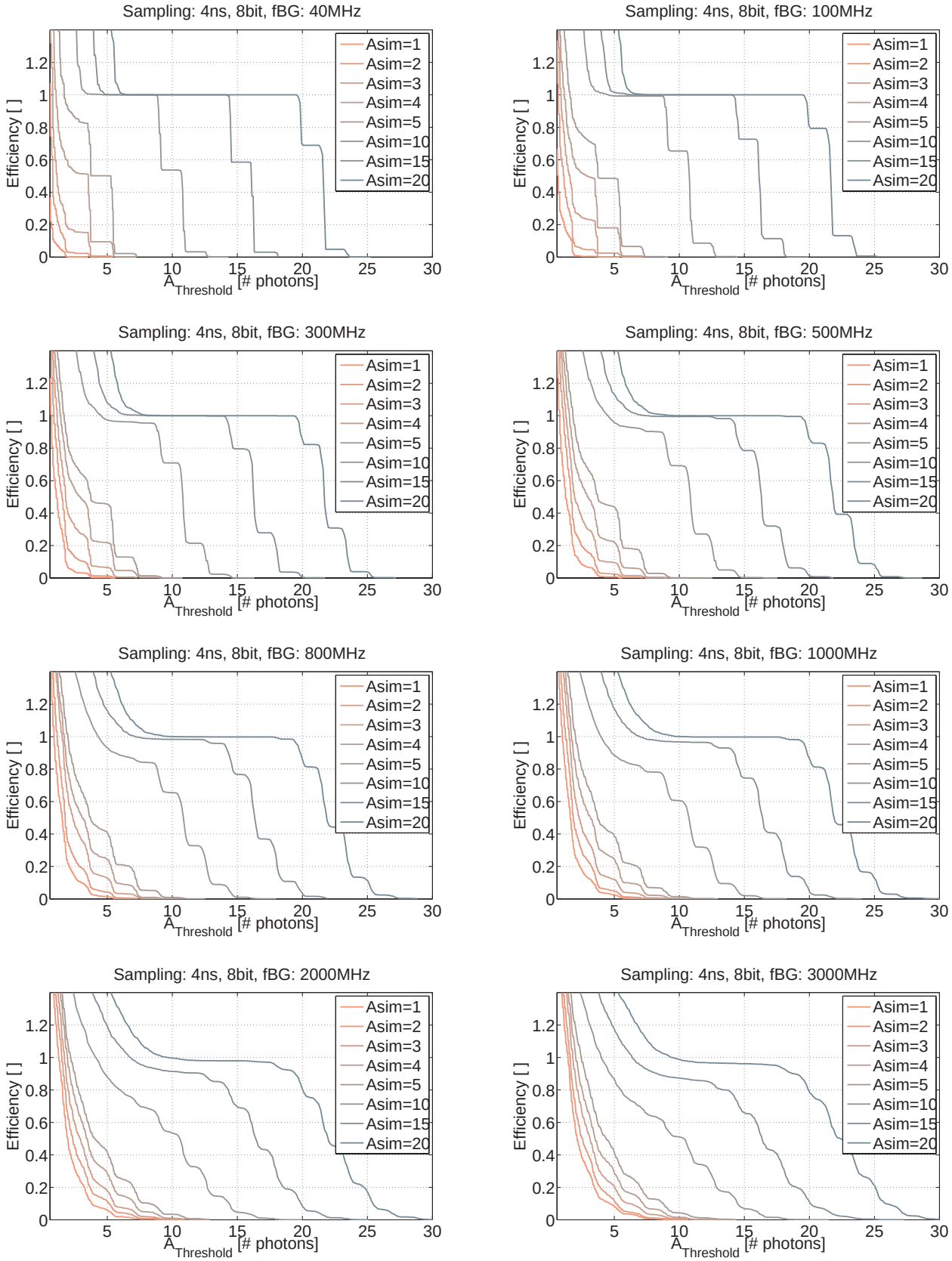

Figure B.4: Efficiency vs. amplitude threshold for 8 bit and 4 ns sampling and NSB frequencies of 40 to 3000 MHz. Each curve has a fixed shower amplitude A_{sim}.

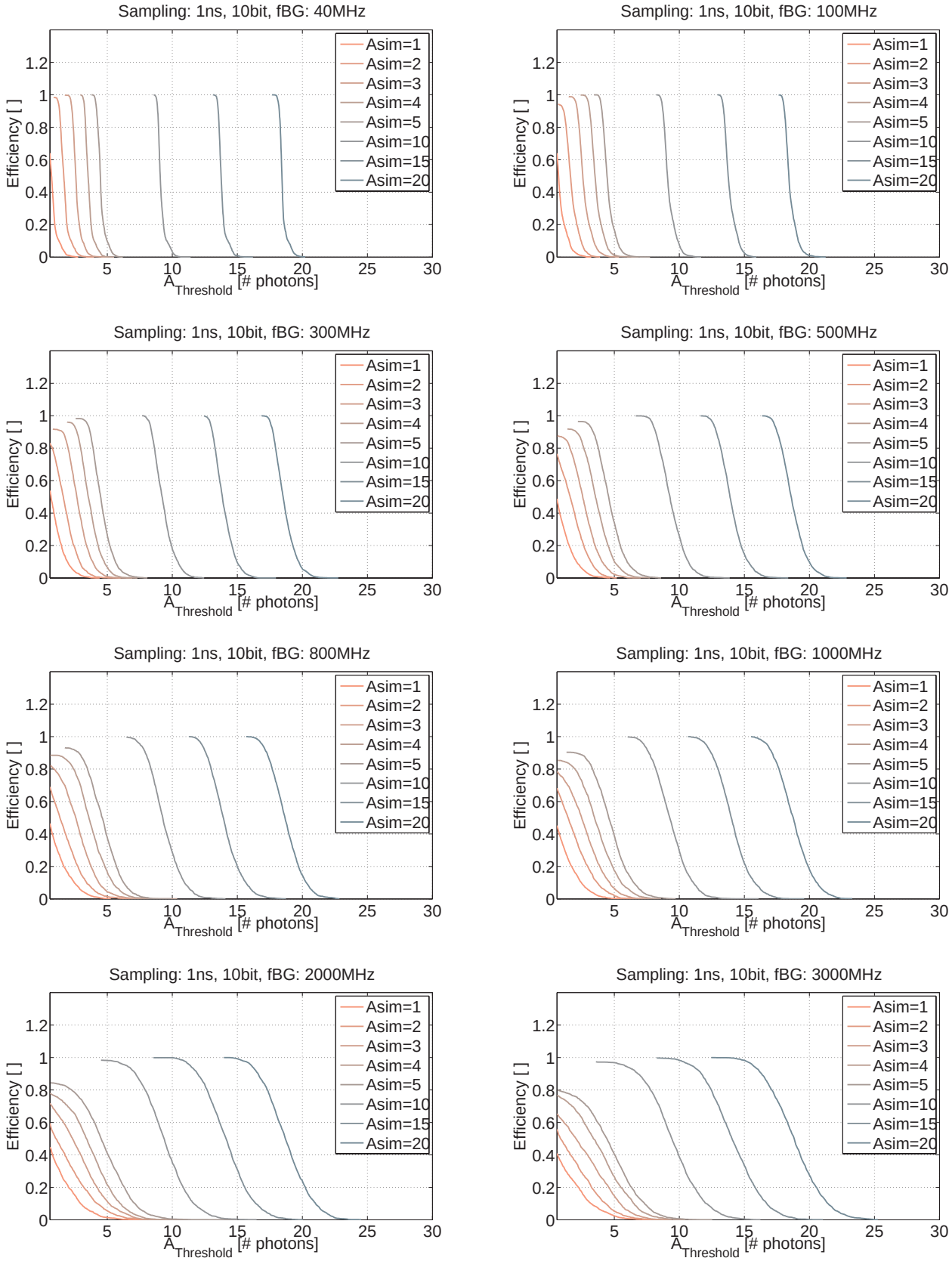

Figure B.5: Efficiency vs. amplitude threshold for 10 bit and 1 ns sampling and NSB frequencies of 40 to 3000 MHz. Each curve has a fixed shower amplitude A_{sim}.

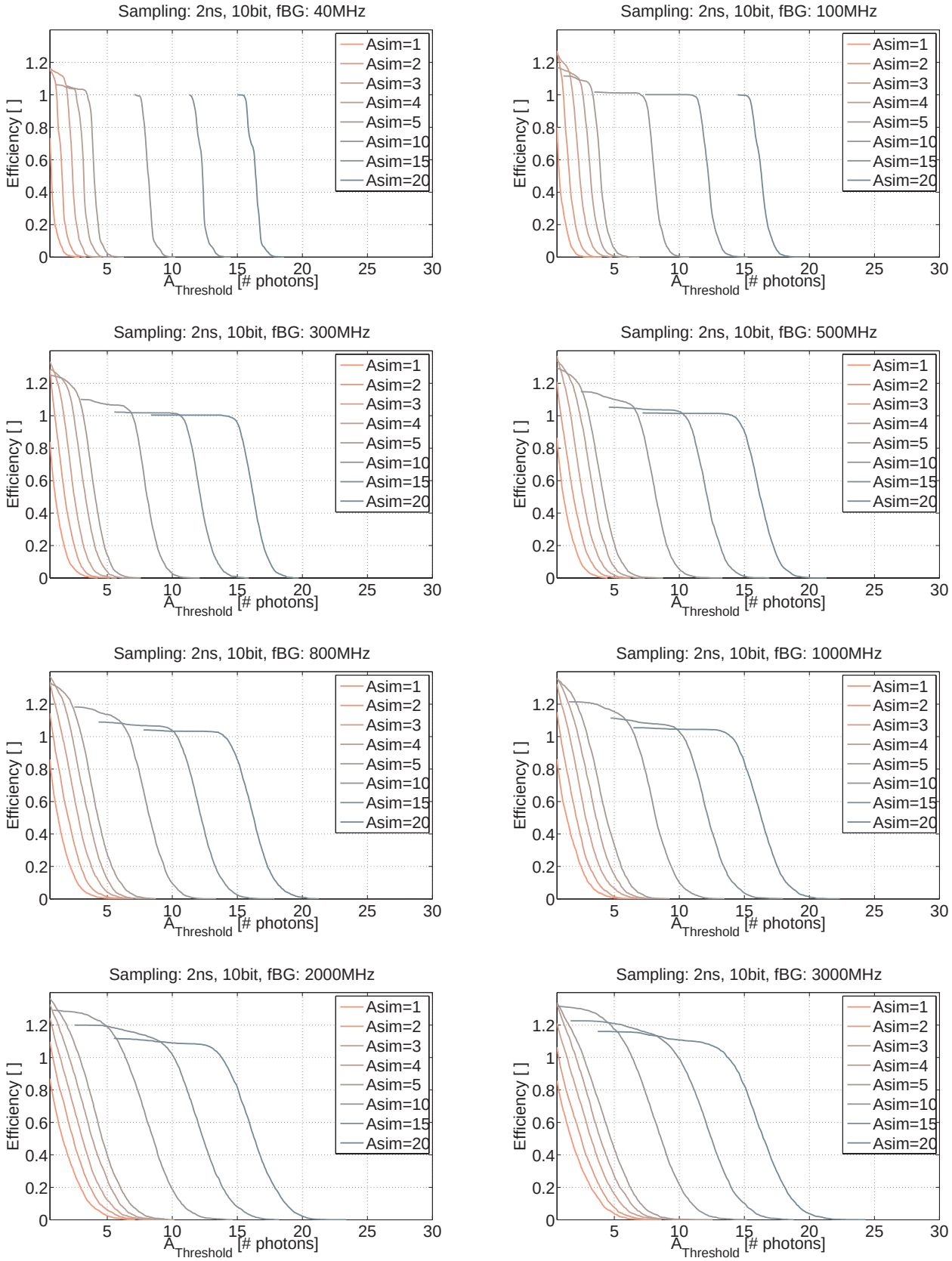

Figure B.6: Efficiency vs. amplitude threshold for 10 bit and 2 ns sampling and NSB frequencies of 40 to 3000 MHz. Each curve has a fixed shower amplitude A_{sim}.

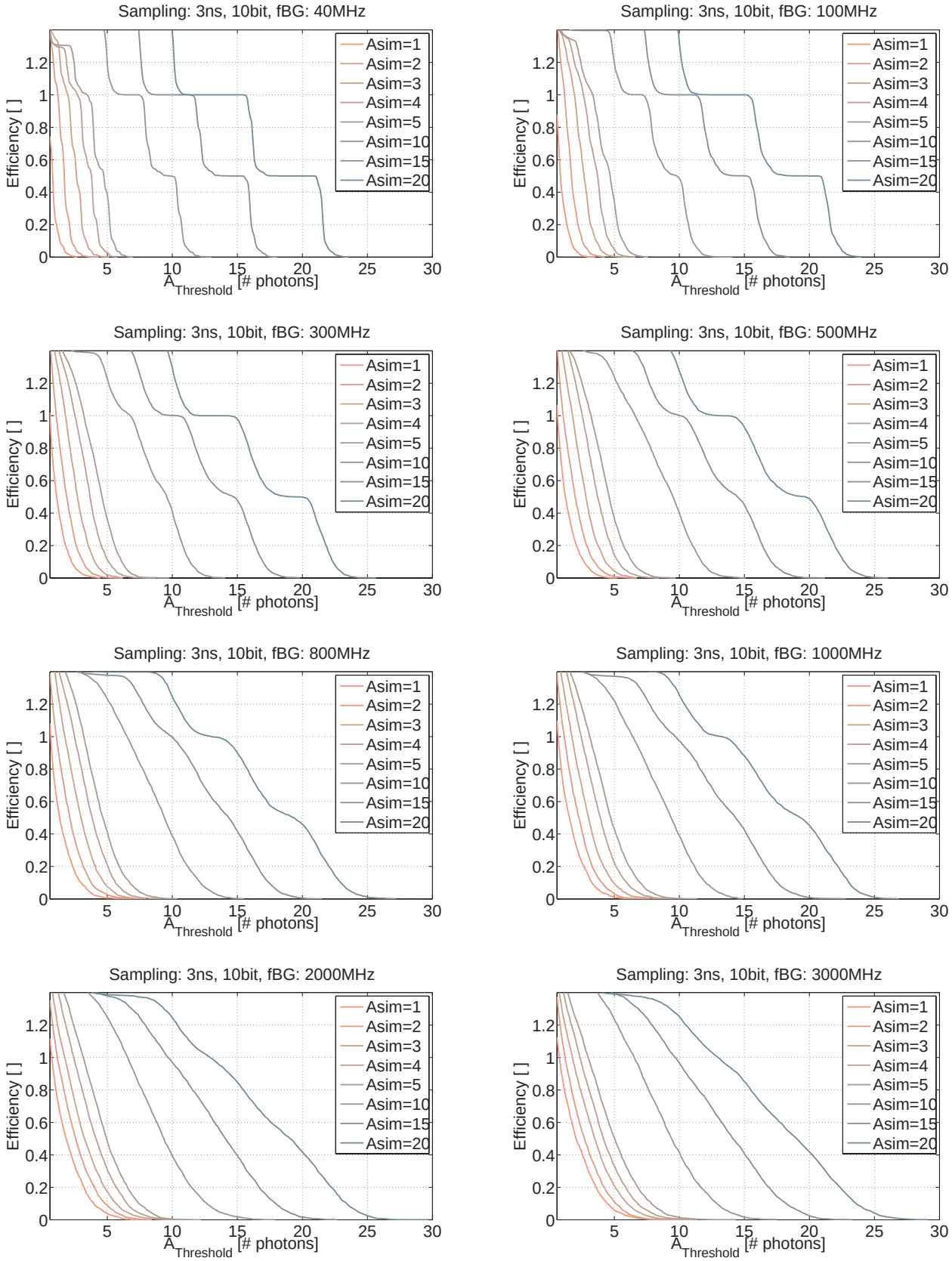

Figure B.7: Efficiency vs. amplitude threshold for 10 bit and 3 ns sampling and NSB frequencies of 40 to 3000 MHz. Each curve has a fixed shower amplitude A_{sim}.

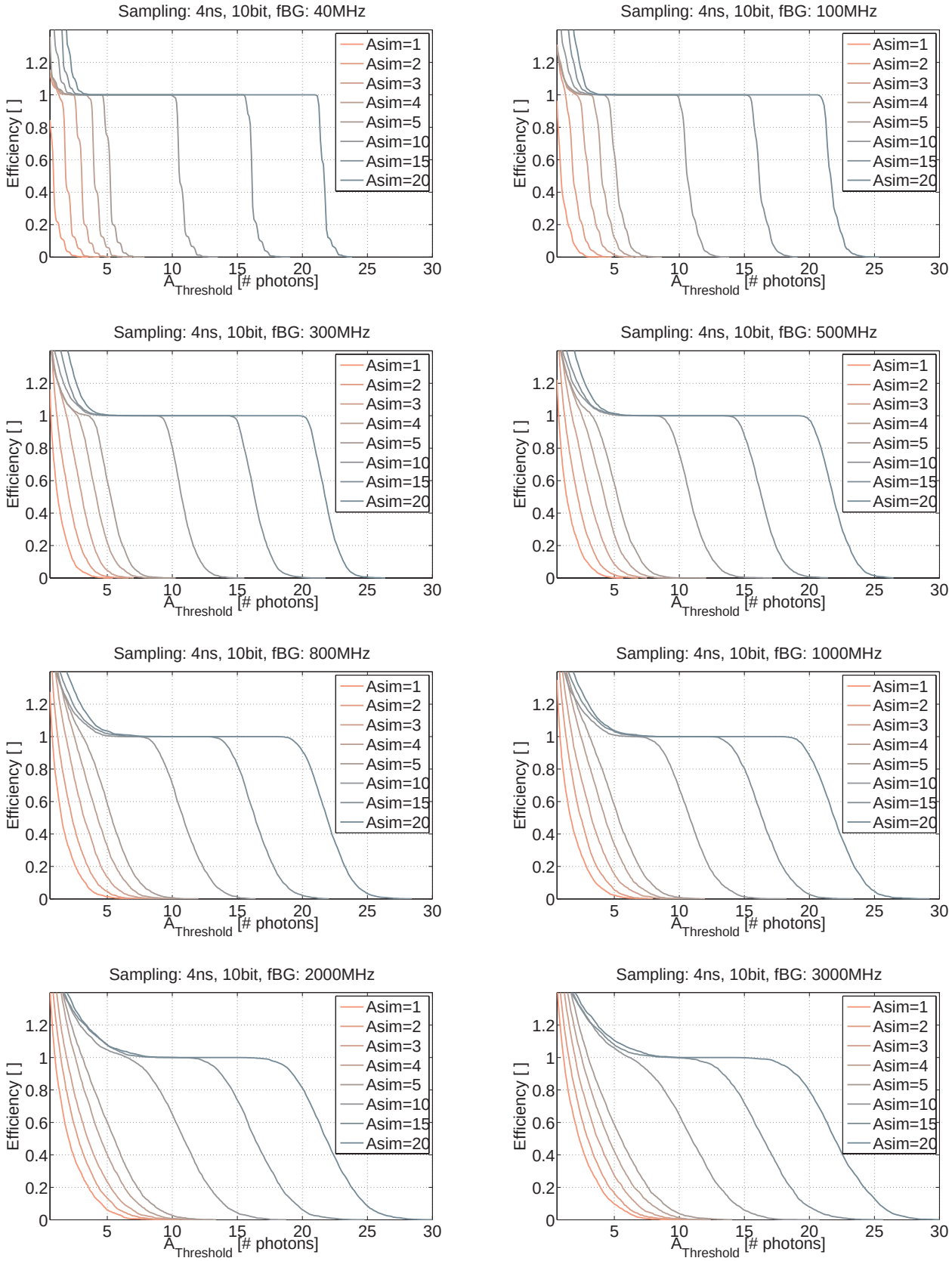

Figure B.8: Efficiency vs. amplitude threshold for 10 bit and 4 ns sampling and NSB frequencies of 40 to 3000 MHz. Each curve has a fixed shower amplitude A_{sim}.

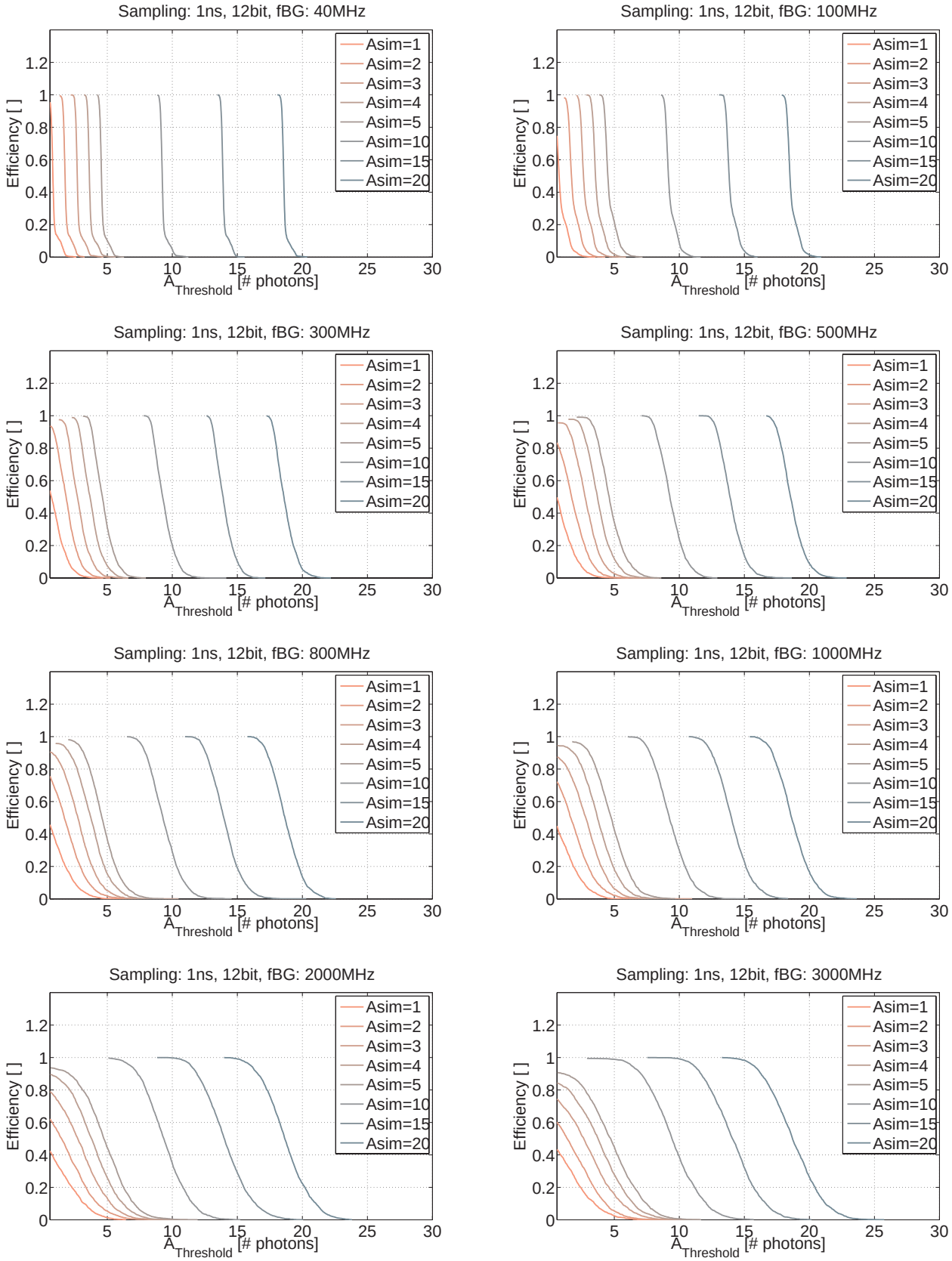

Figure B.9: Efficiency vs. amplitude threshold for 12 bit and 1 ns sampling and NSB frequencies of 40 to 3000 MHz. Each curve has a fixed shower amplitude A_{sim}.

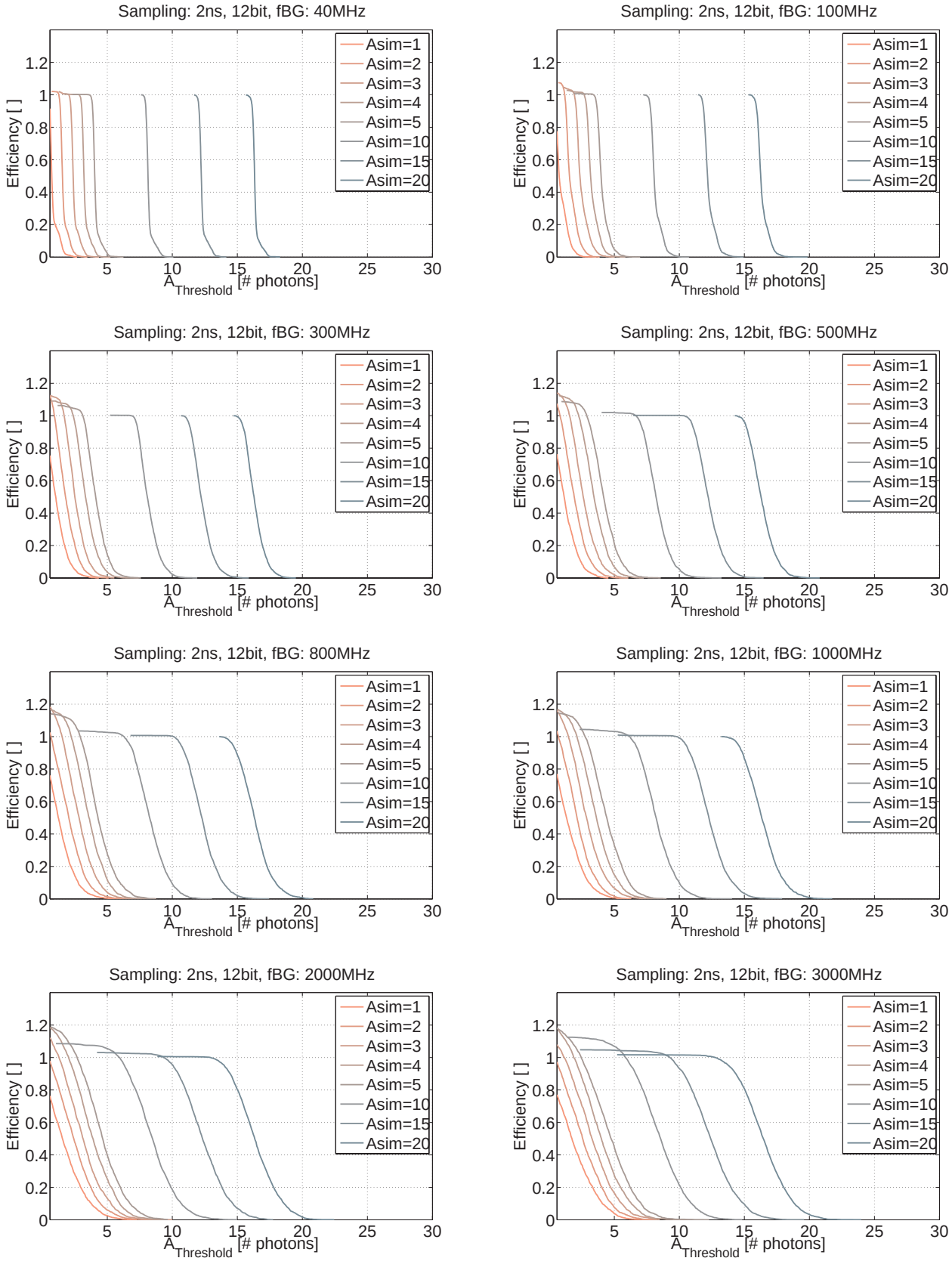

Figure B.10: Efficiency vs. amplitude threshold for 12 bit and 2 ns sampling and NSB frequencies of 40 to 3000 MHz. Each curve has a fixed shower amplitude A_{sim}.

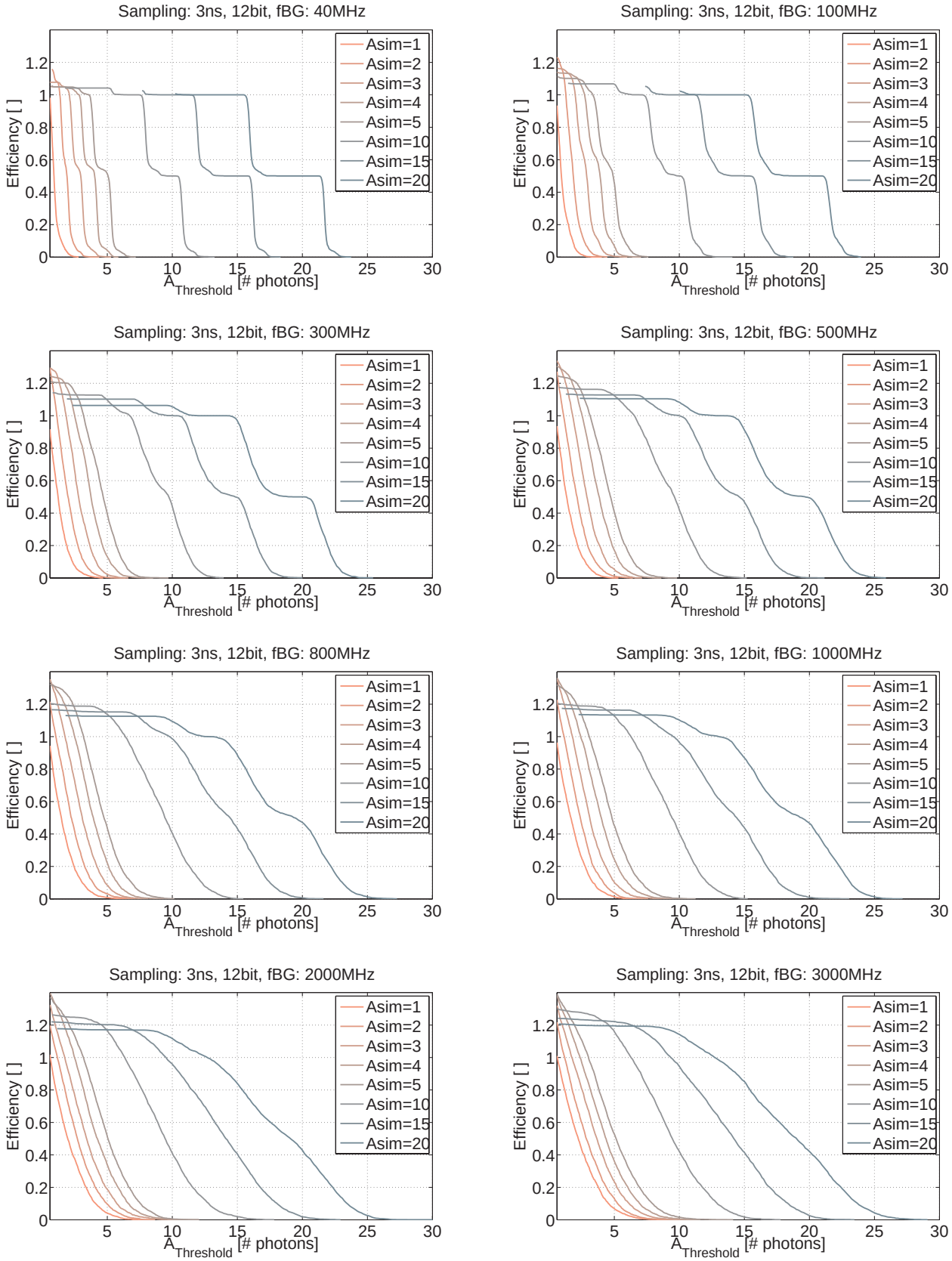

Figure B.11: Efficiency vs. amplitude threshold for 12 bit and 3 ns sampling and NSB frequencies of 40 to 3000 MHz. Each curve has a fixed shower amplitude A_{sim}.

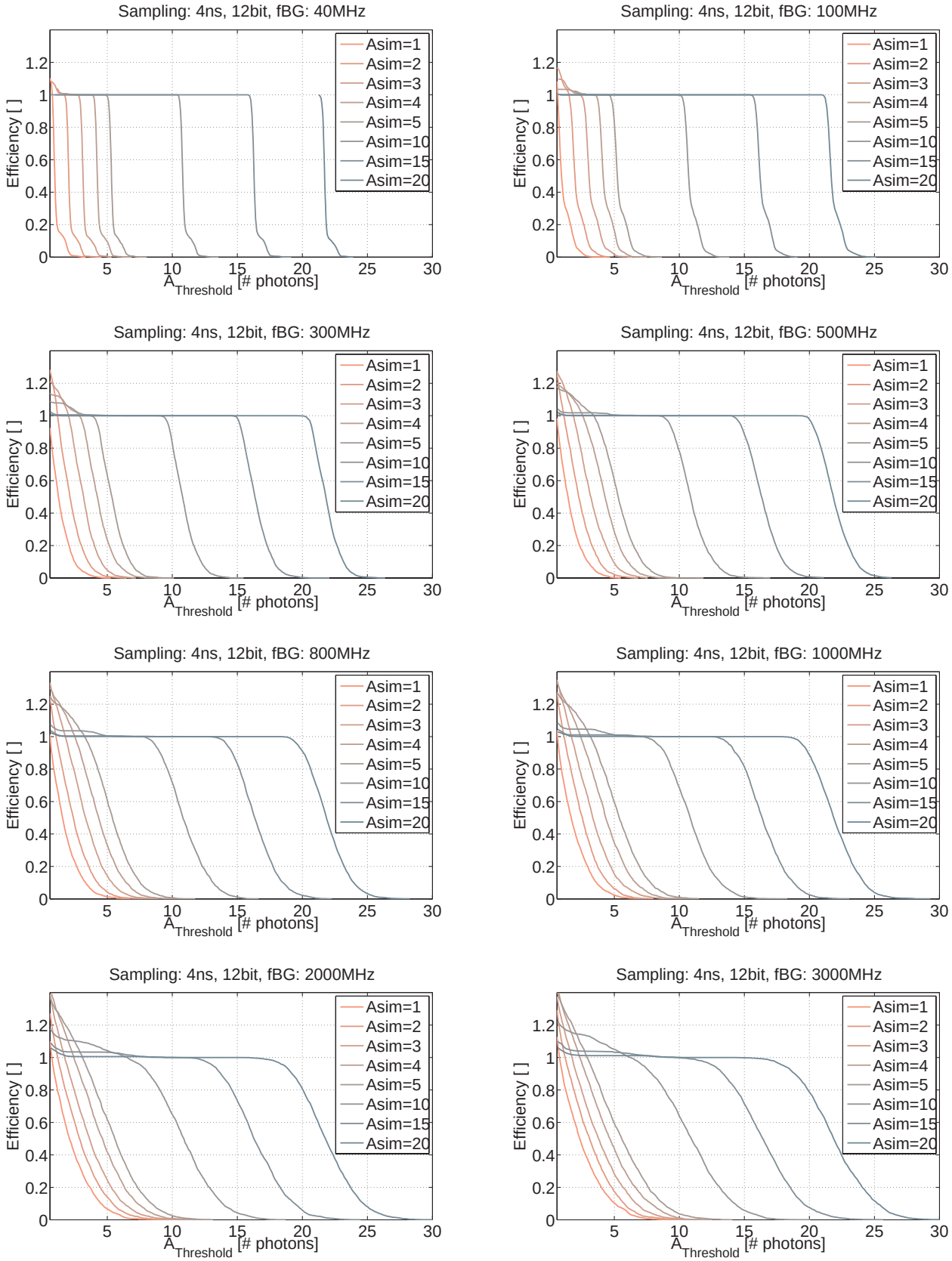

Figure B.12: Efficiency vs. amplitude threshold for 12 bit and 4 ns sampling and NSB frequencies of 40 to 3000 MHz. Each curve has a fixed shower amplitude A_{sim}.

B.2 Noise rate

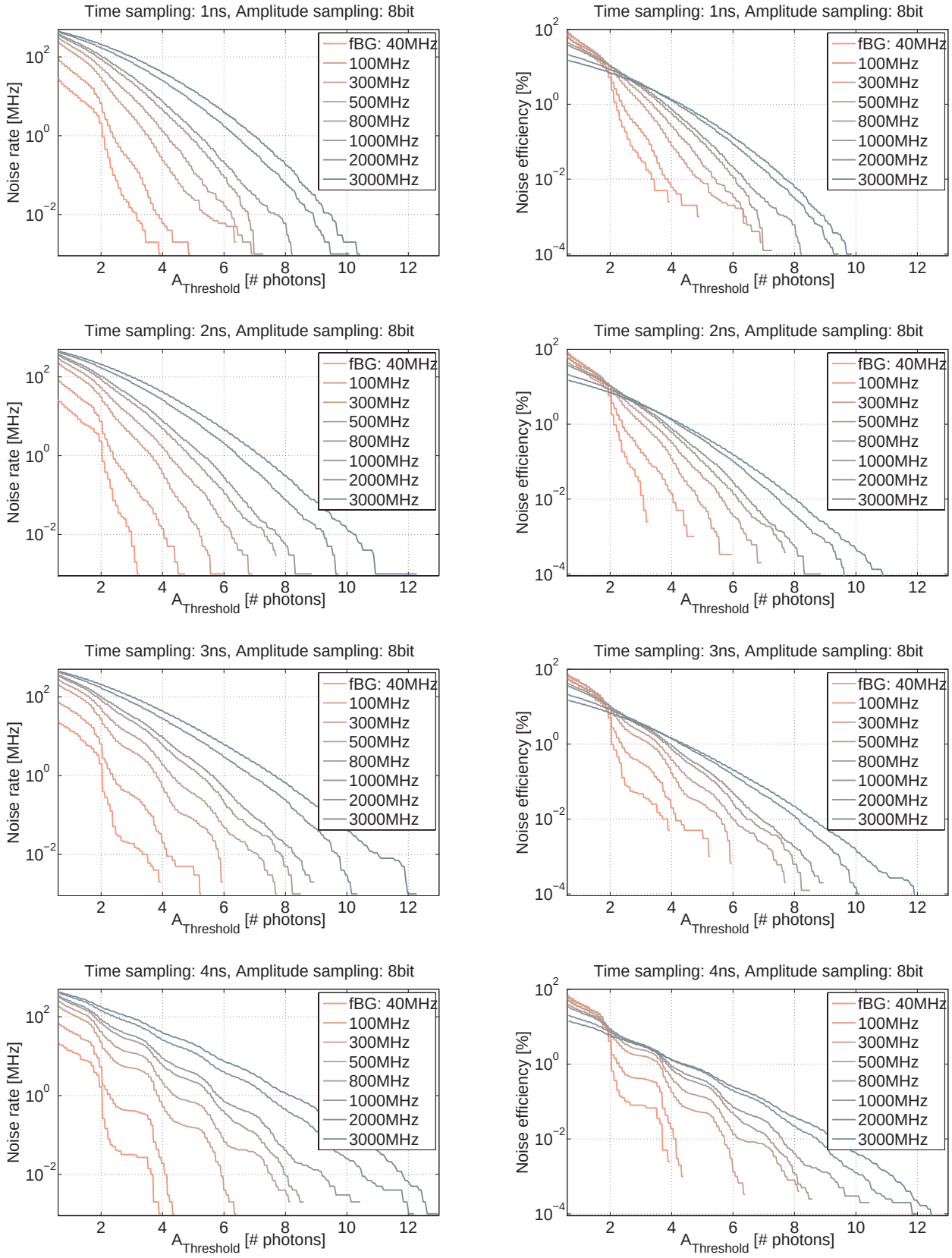

Figure B.13: Noise rate (left) and noise efficiency (right) versus amplitude threshold for 1-4 ns and 8 bit sampling.

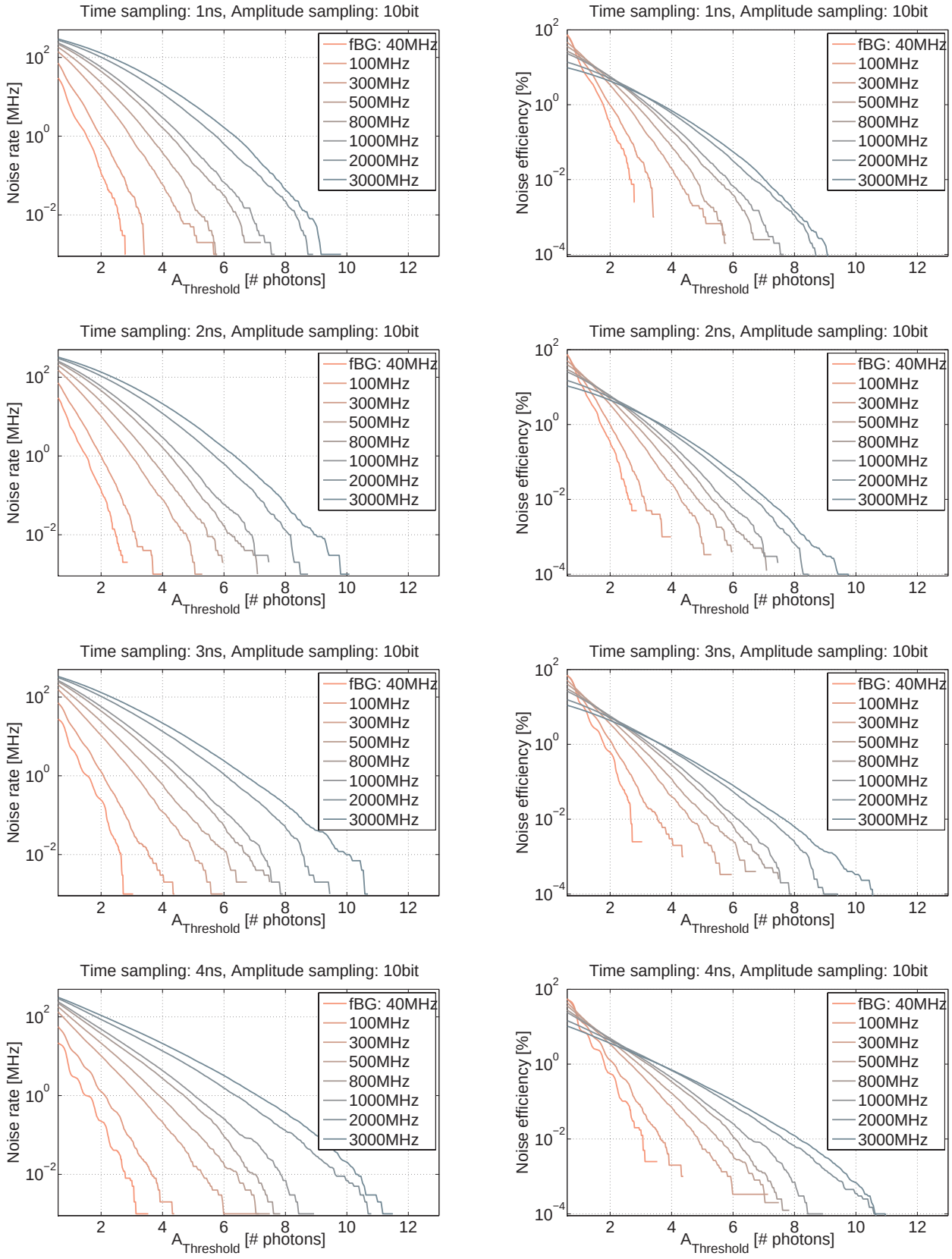

Figure B.14: Noise rate (left) and noise efficiency (right) versus amplitude threshold for 1-4 ns and 10 bit sampling.

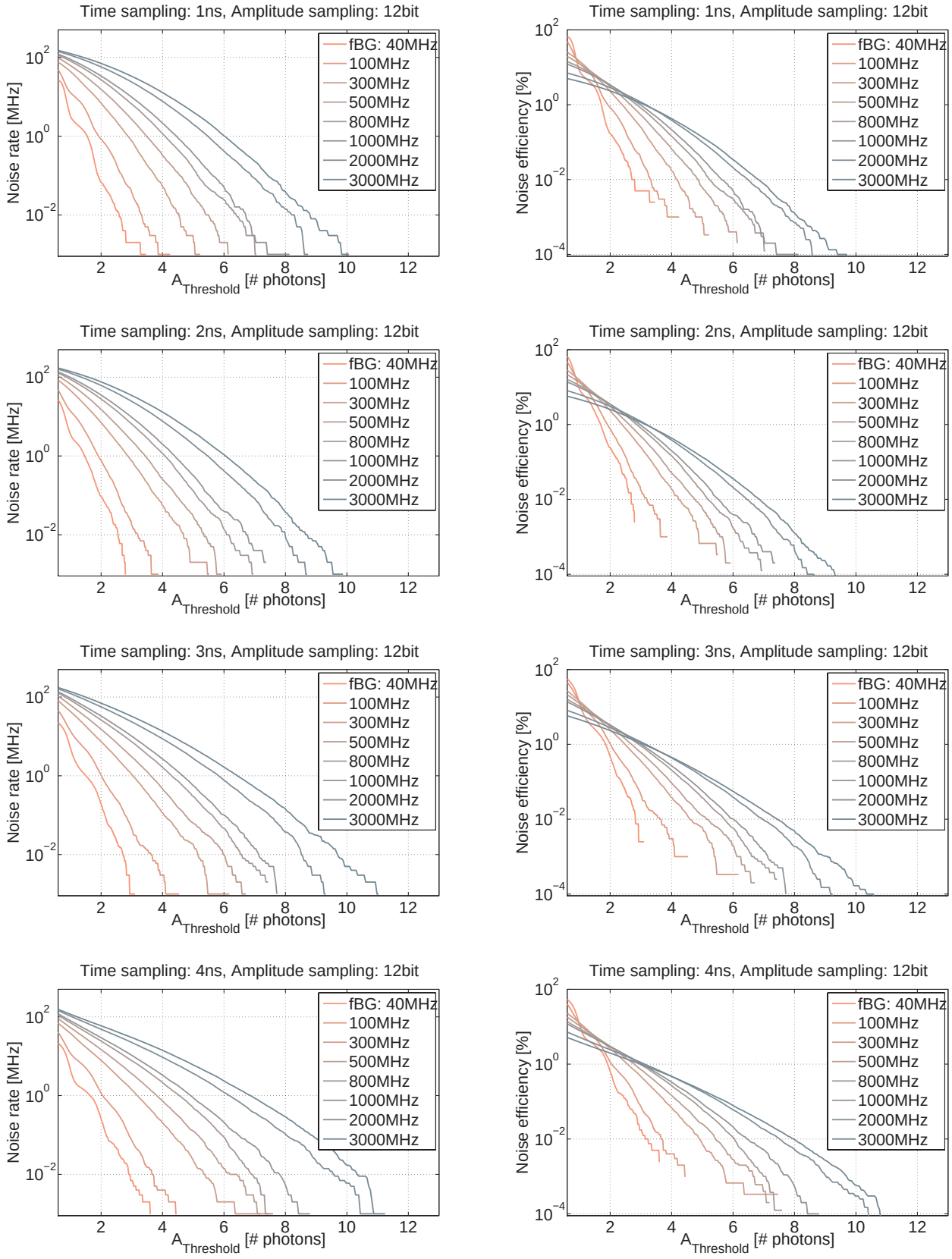

Figure B.15: Noise rate (left) and noise efficiency (right) versus amplitude threshold for 1-4 ns and 12 bit sampling.

B.3 Histograms of the amplitude difference $\Delta A = A_{sim} - A_{rec}$

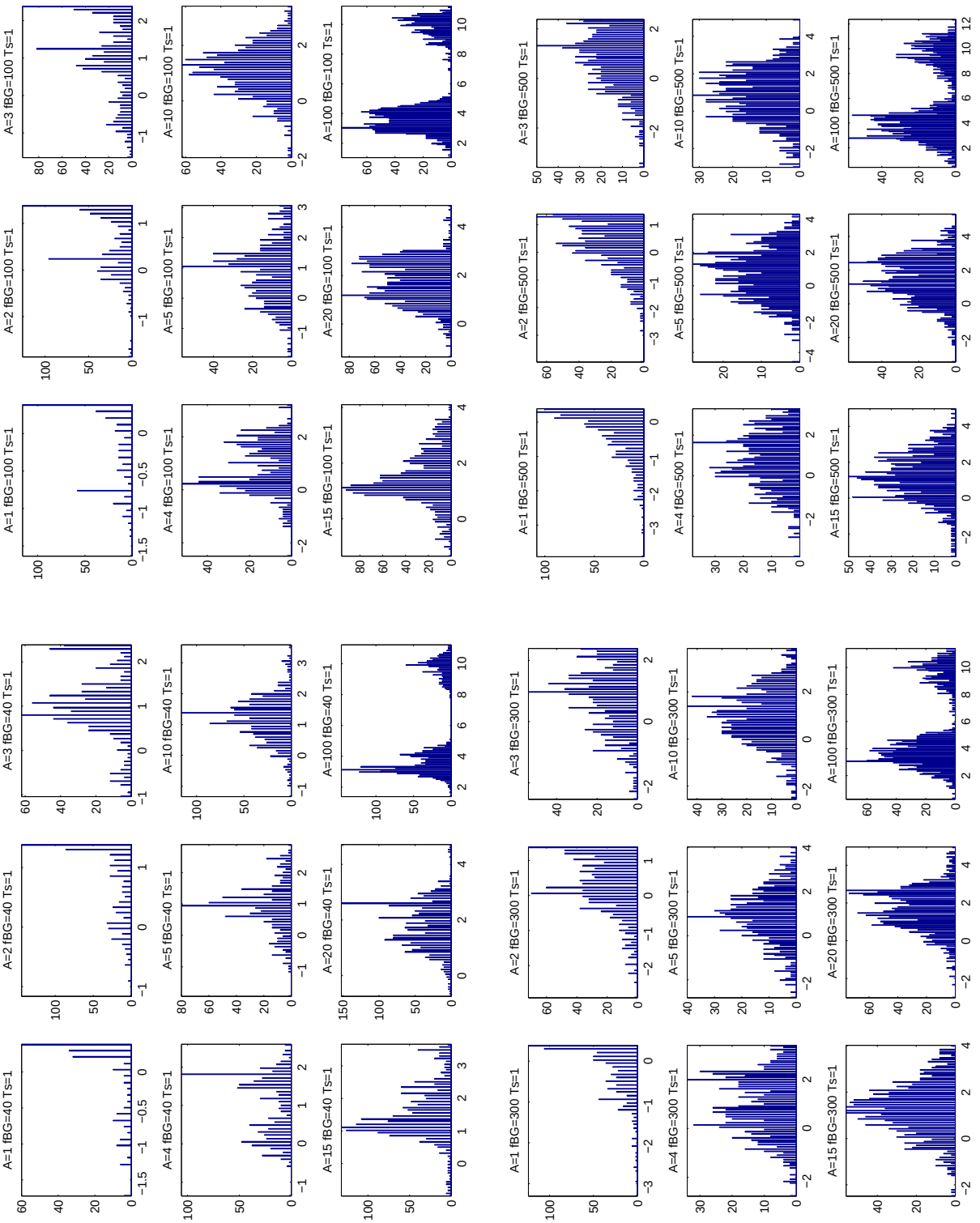

Figure B.16: Histograms of $\Delta A = A_{sim} - A_{rec}$ for 8 bits and 1 ns sampling. NSB frequency f_{BG} = 40 to 500 MHz.

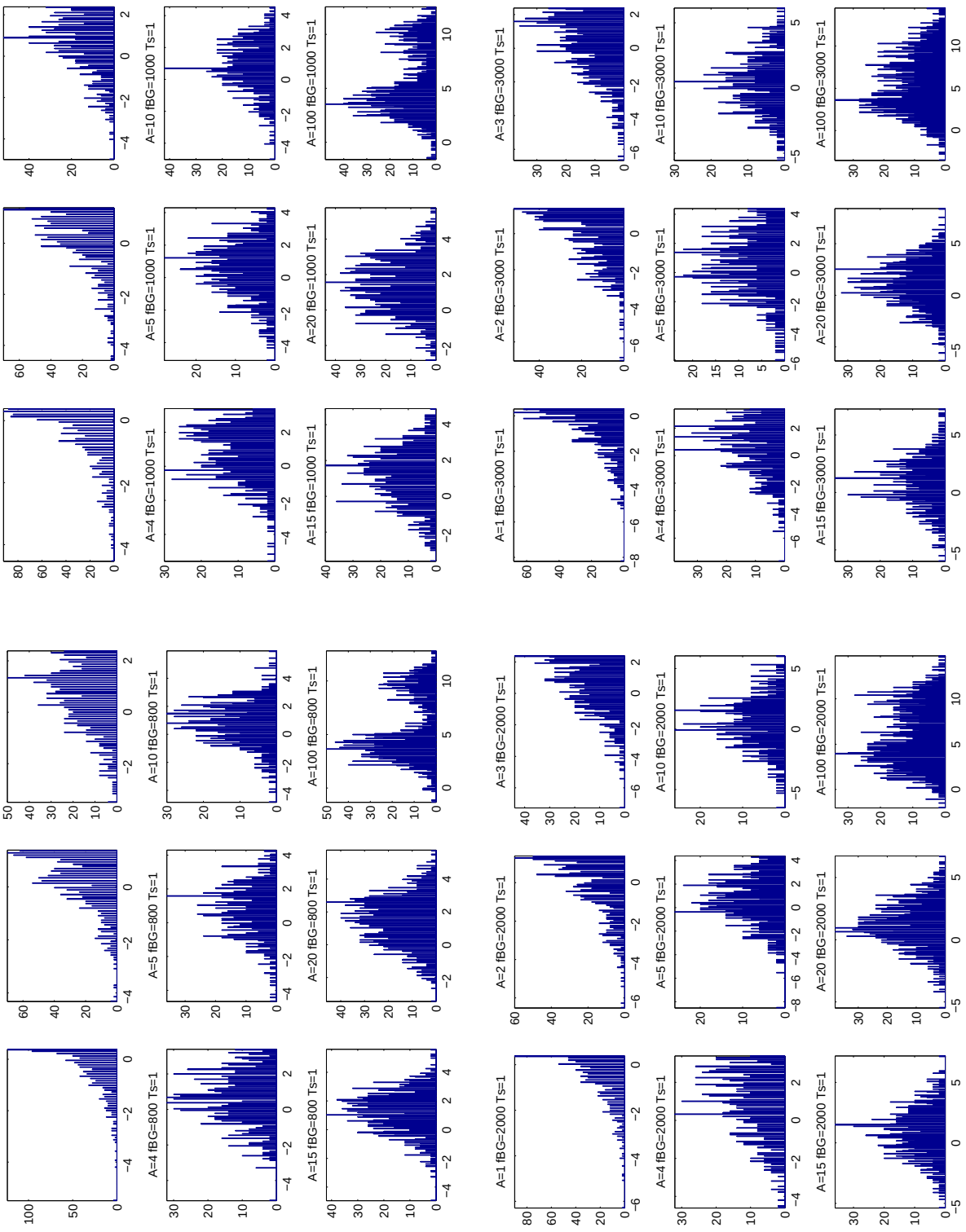

Figure B.17: Histograms of $\Delta A = A_{sim} - A_{rec}$ for 8 bits and 1 ns sampling. NSB frequency f_{BG} = 800 to 3000 MHz.

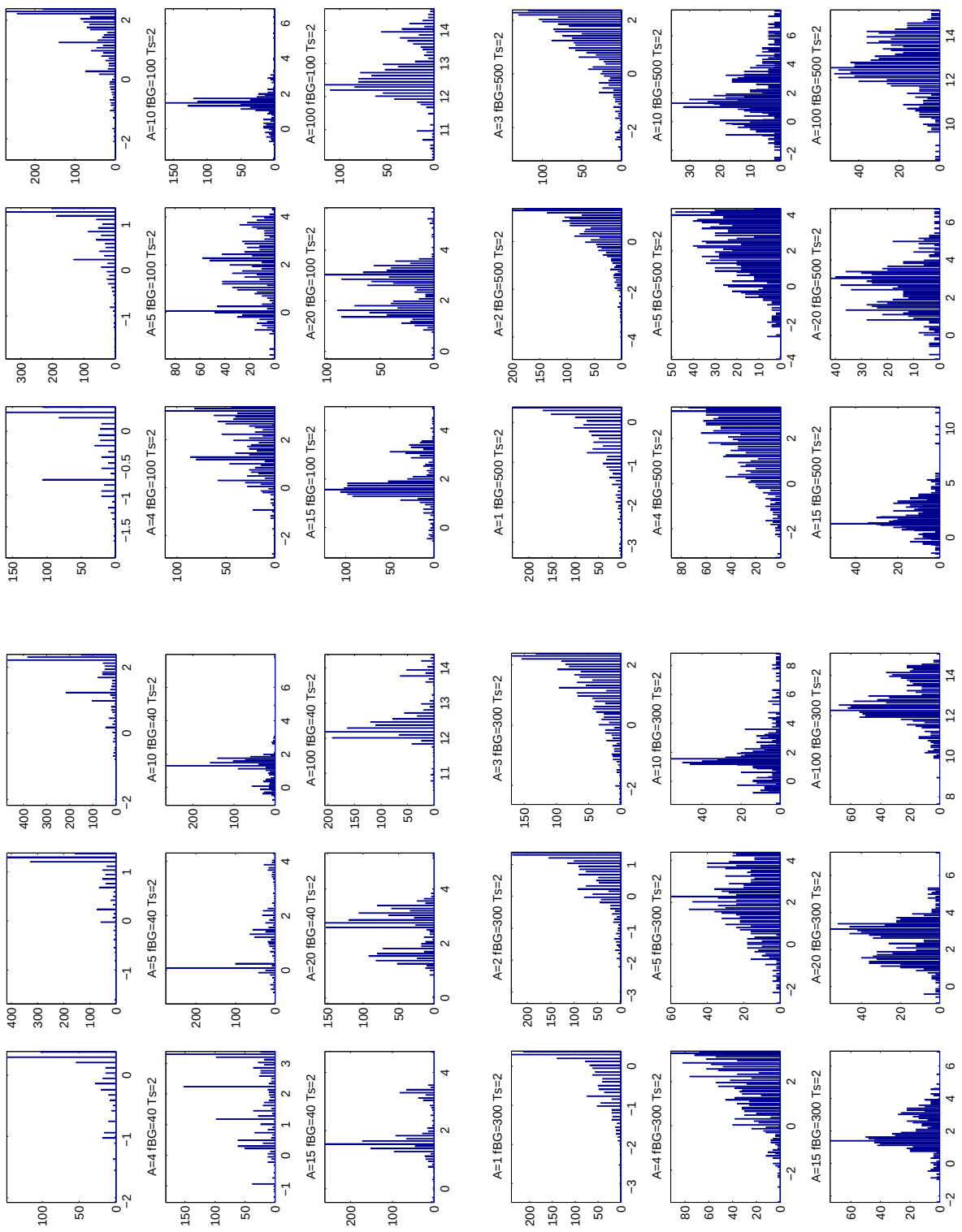

Figure B.18: Histograms of $\Delta A = A_{sim} - A_{rec}$ for 8 bits and 2 ns sampling. NSB frequency f_{BG} = 40 to 500 MHz.

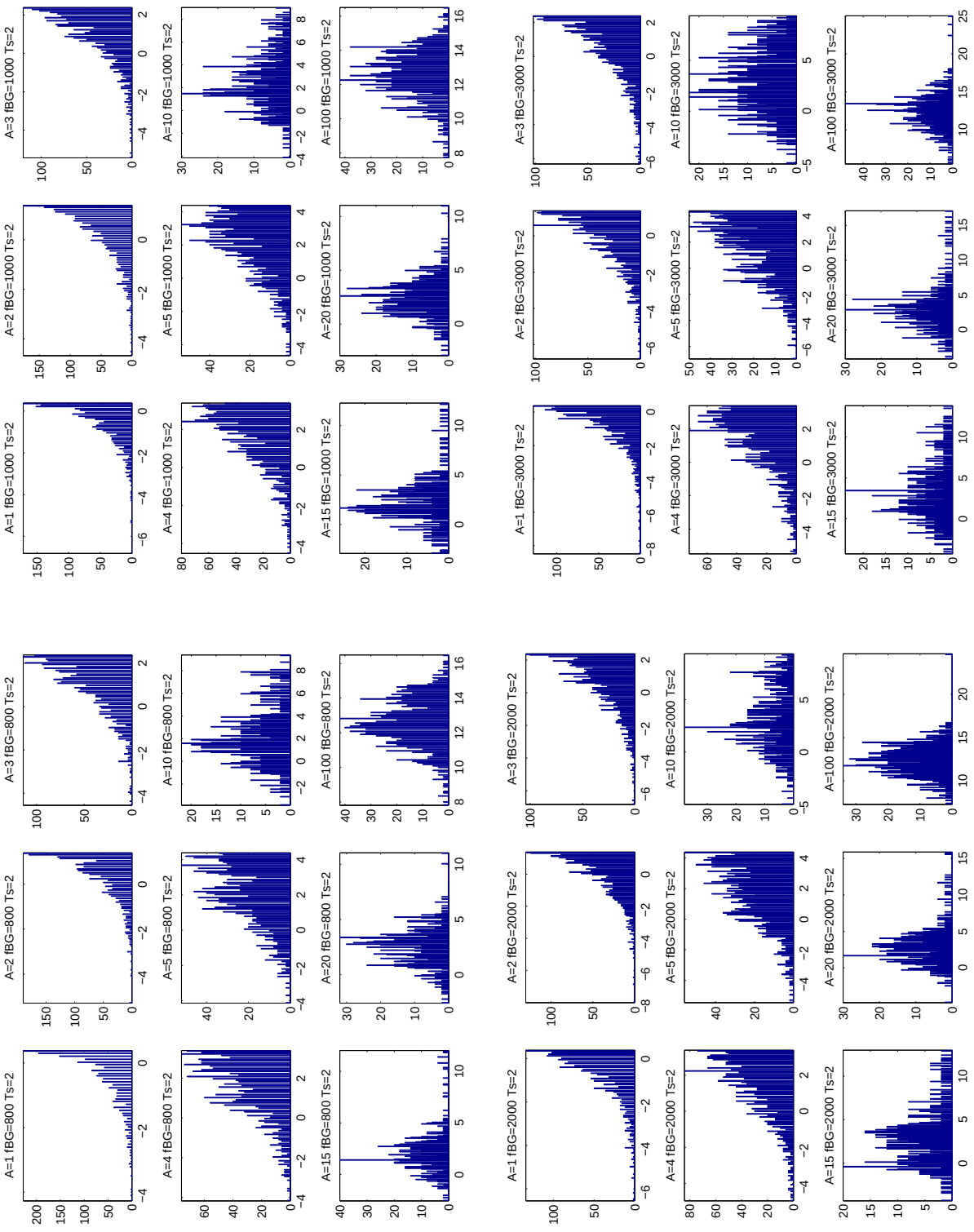

Figure B.19: Histograms of $\Delta A = A_{sim} - A_{rec}$ for 8 bits and 2 ns sampling. NSB frequency f_{BG} = 800 to 3000 MHz.

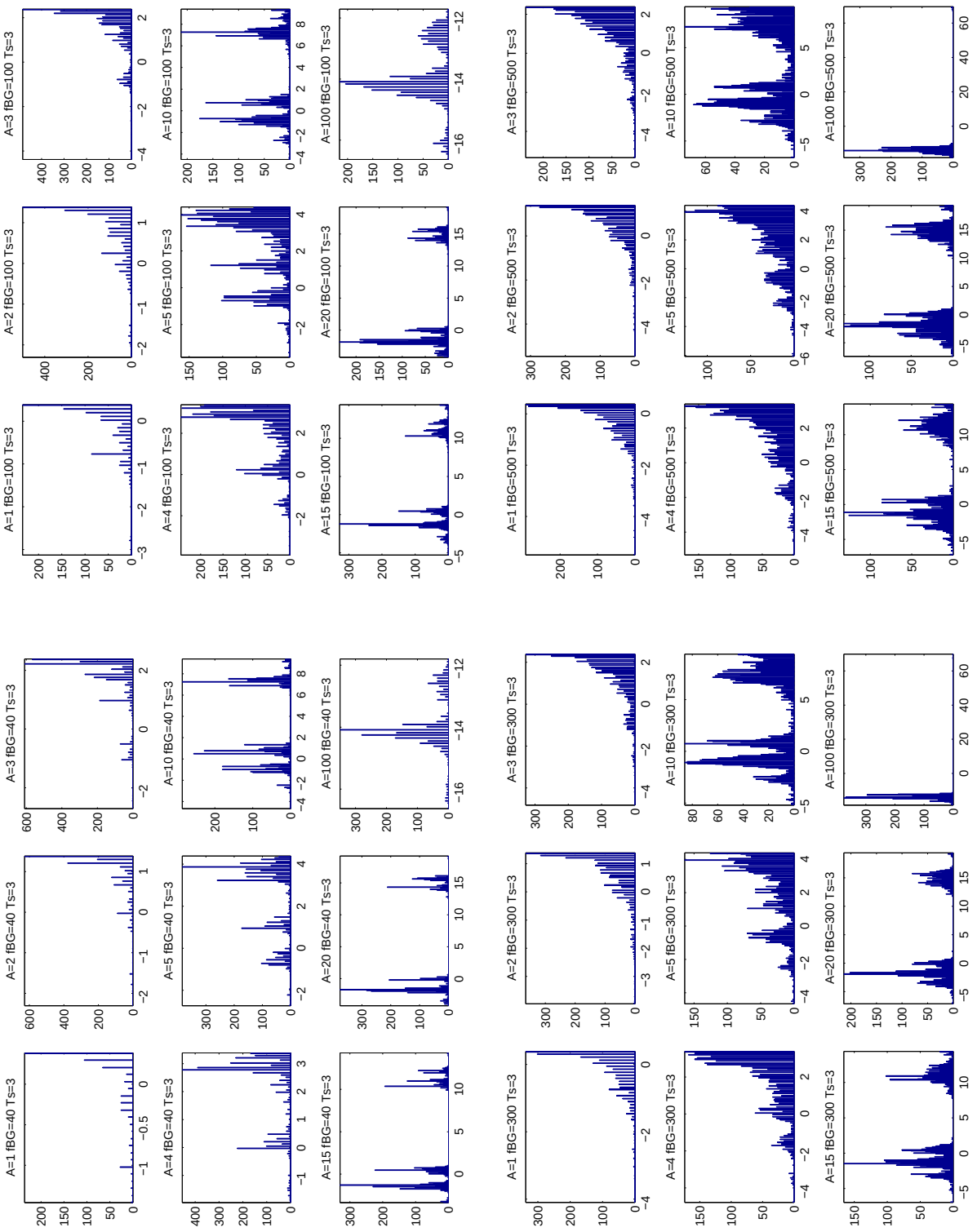

Figure B.20: Histograms of $\Delta A = A_{sim} - A_{rec}$ for 8 bits and 3 ns sampling. NSB frequency f_{BG} = 40 to 500 MHz.

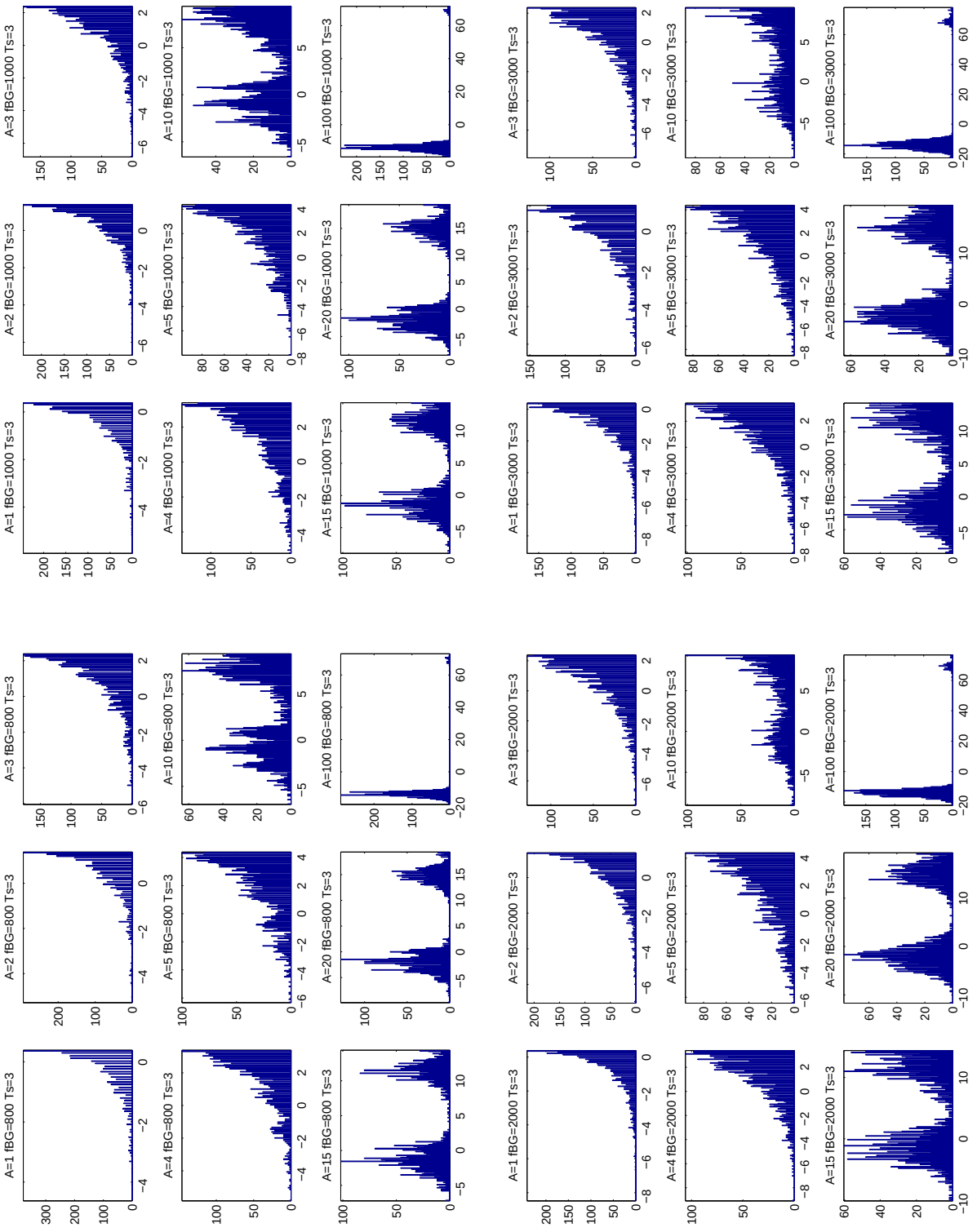

Figure B.21: Histograms of $\Delta A = A_{sim} - A_{rec}$ for 8 bits and 3 ns sampling. NSB frequency $f_{BG} = 800$ to 3000 MHz.

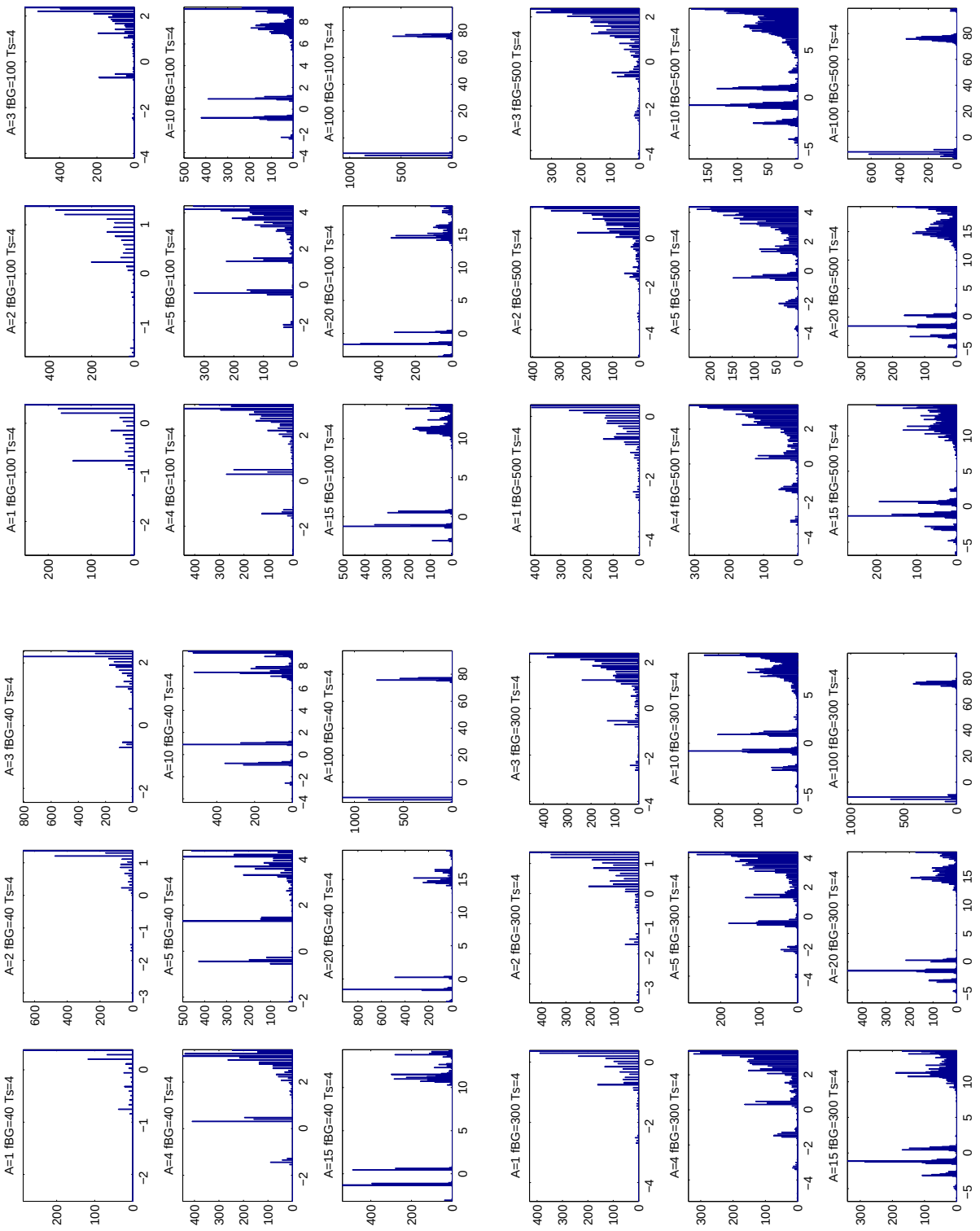

Figure B.22: Histograms of $\Delta A = A_{sim} - A_{rec}$ for 8 bits and 4 ns sampling. NSB frequency f_{BG} = 40 to 500 MHz.

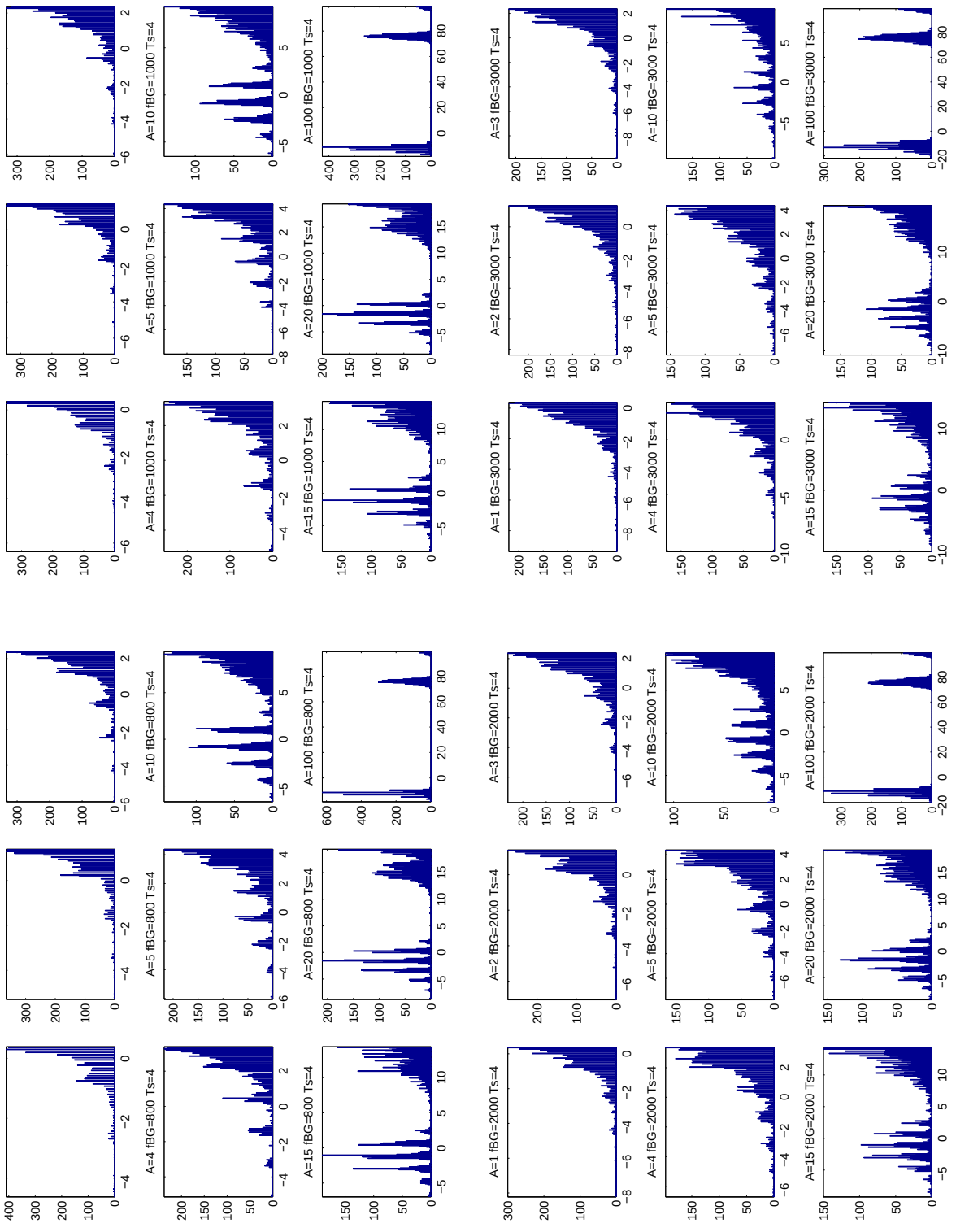

Figure B.23: Histograms of $\Delta A = A_{sim} - A_{rec}$ for 8 bits and 4 ns sampling. NSB frequency $f_{BG} = 800$ to 3000 MHz.

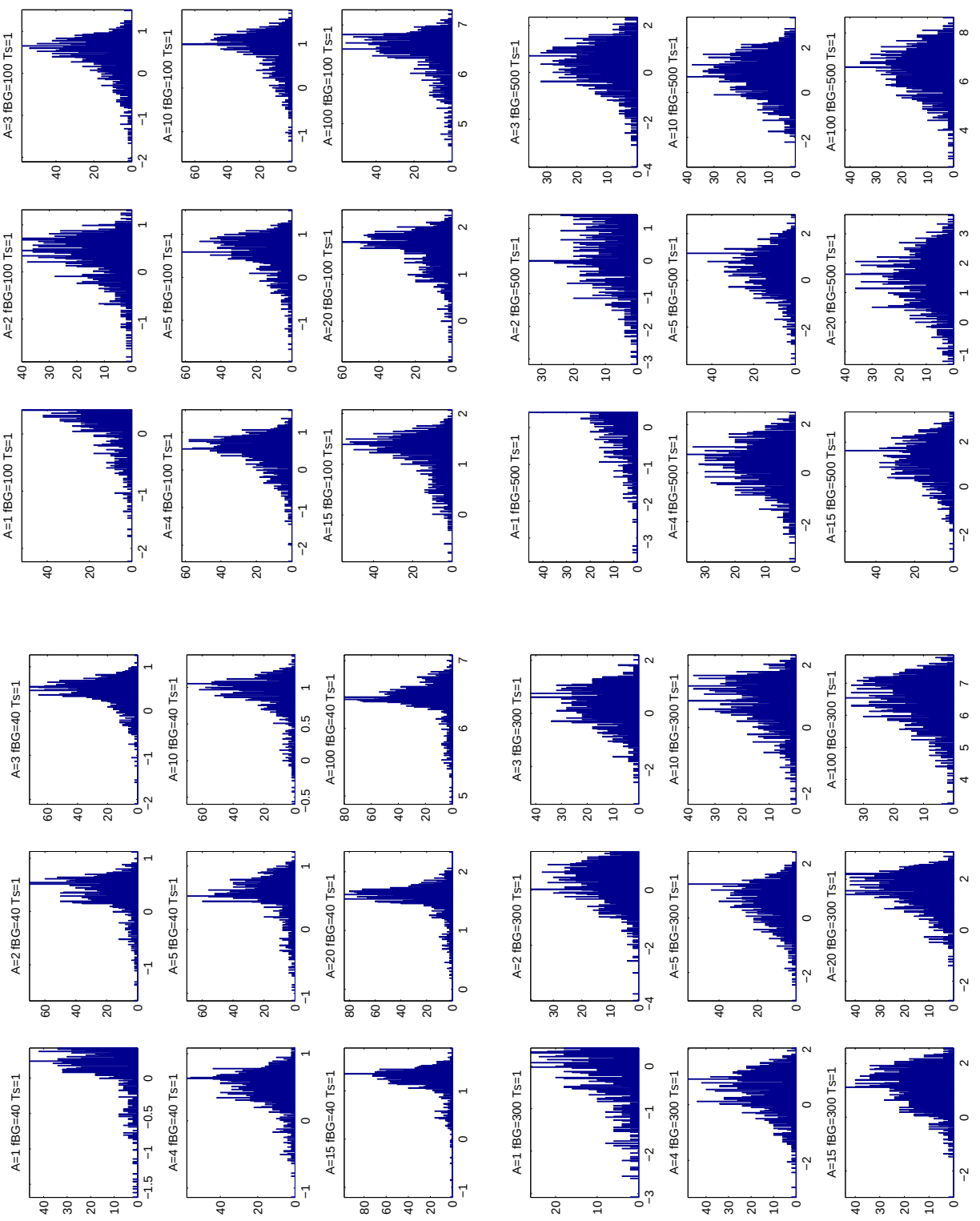

Figure B.24: Histograms of $\Delta A = A_{sim} - A_{rec}$ for 10 bits and 1 ns sampling. NSB frequency $f_{BG} = 40$ to 500 MHz.

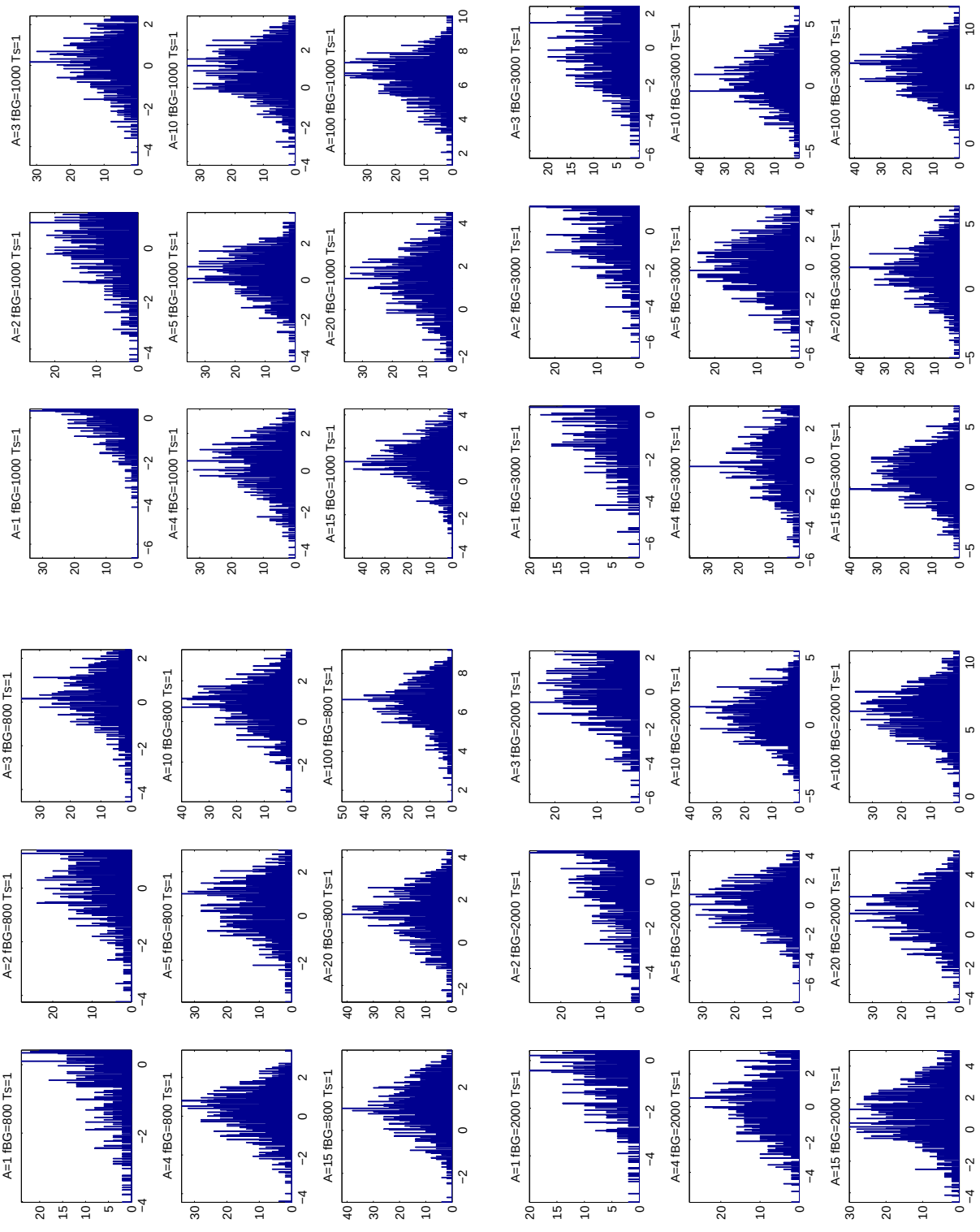

Figure B.25: Histograms of $\Delta A = A_{sim} - A_{rec}$ for 10 bits and 1 ns sampling. NSB frequency $f_{BG} = 800$ to 3000 MHz.

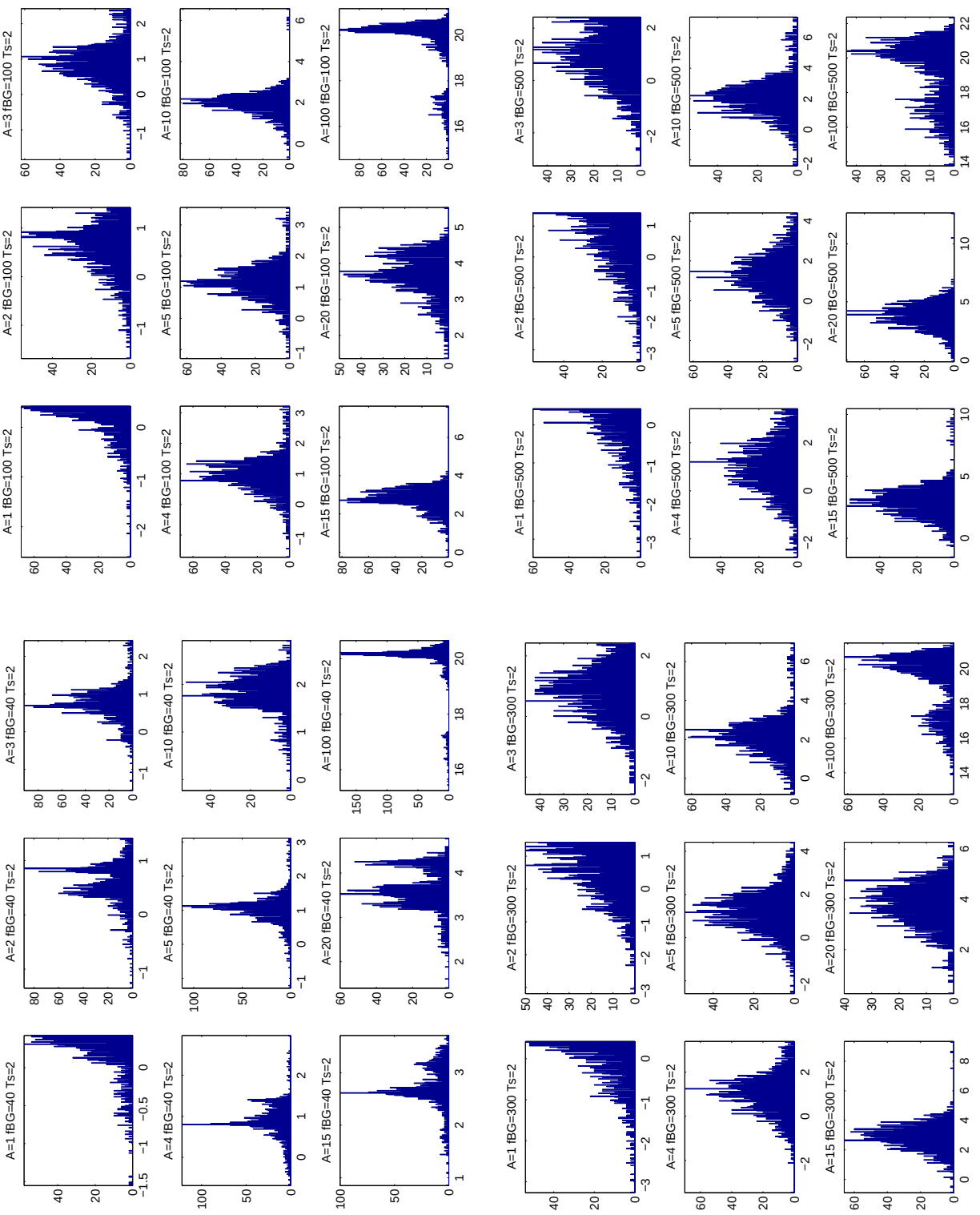

Figure B.26: Histograms of $\Delta A = A_{sim} - A_{rec}$ for 10 bits and 2 ns sampling. NSB frequency $f_{BG} = 40$ to 500 MHz.

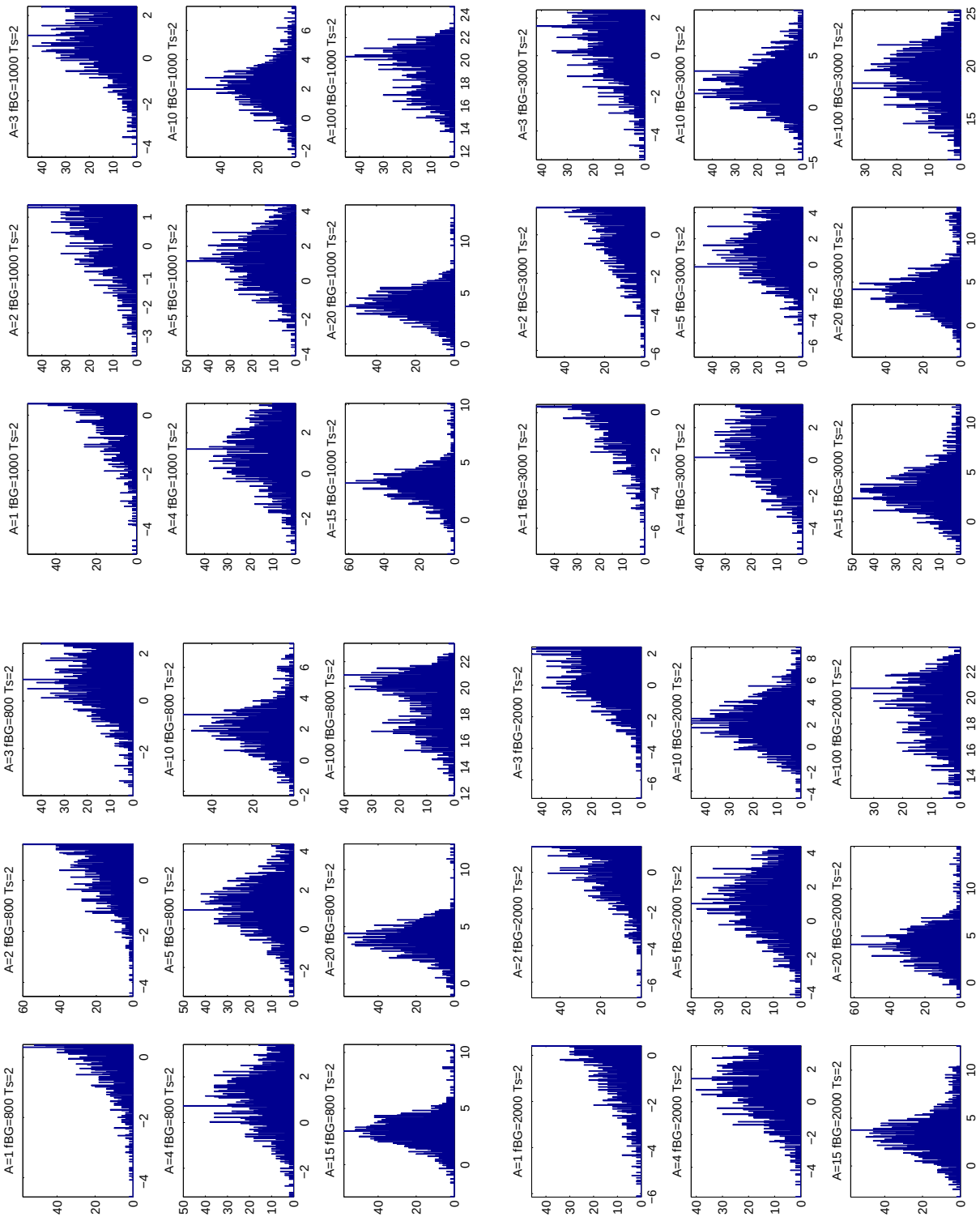

Figure B.27: Histograms of $\Delta A = A_{sim} - A_{rec}$ for 10 bits and 2 ns sampling. NSB frequency $f_{BG} = 800$ to 3000 MHz.

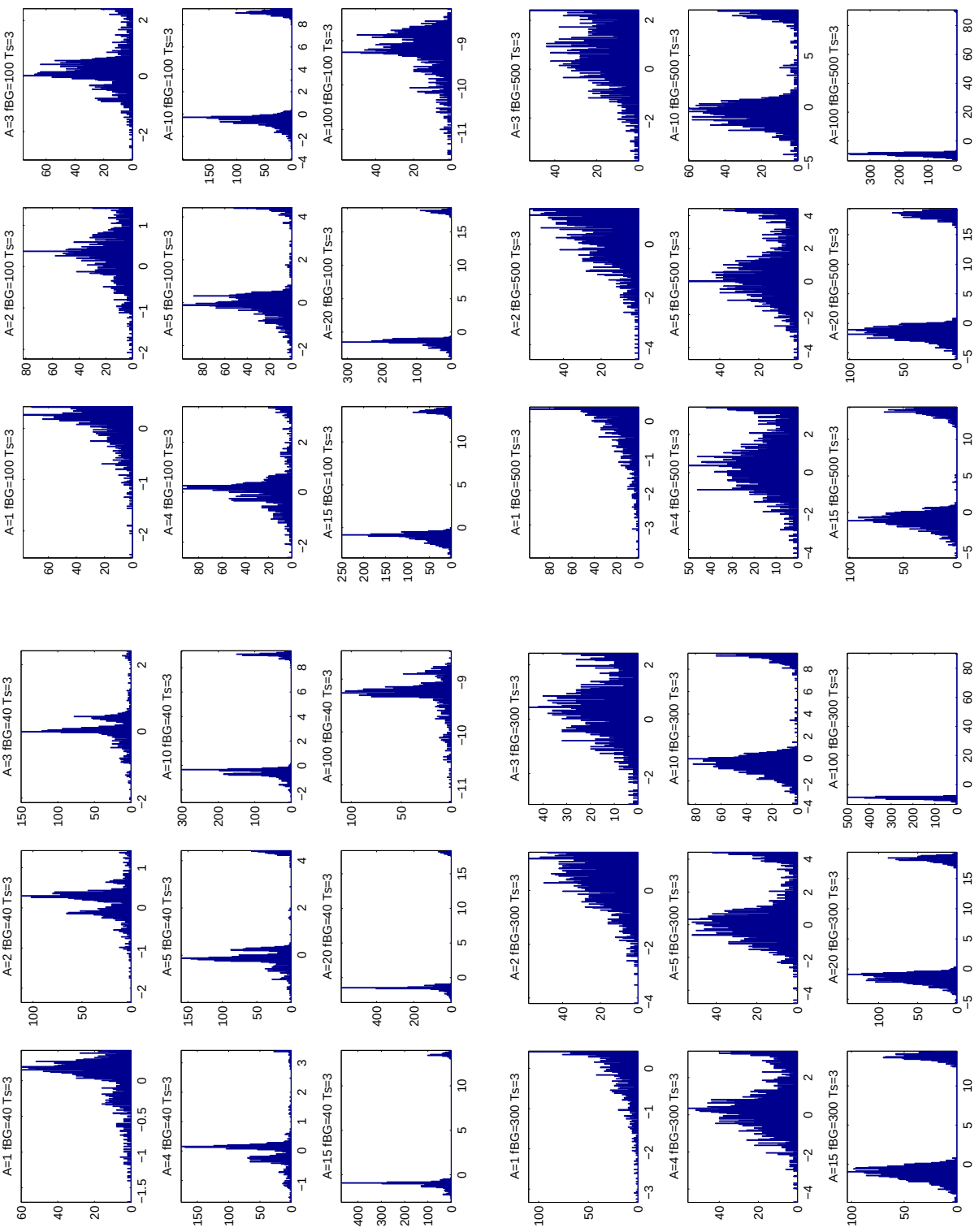

Figure B.28: Histograms of $\Delta A = A_{sim} - A_{rec}$ for 10 bits and 3 ns sampling. NSB frequency $f_{BG} = 40$ to 500 MHz.

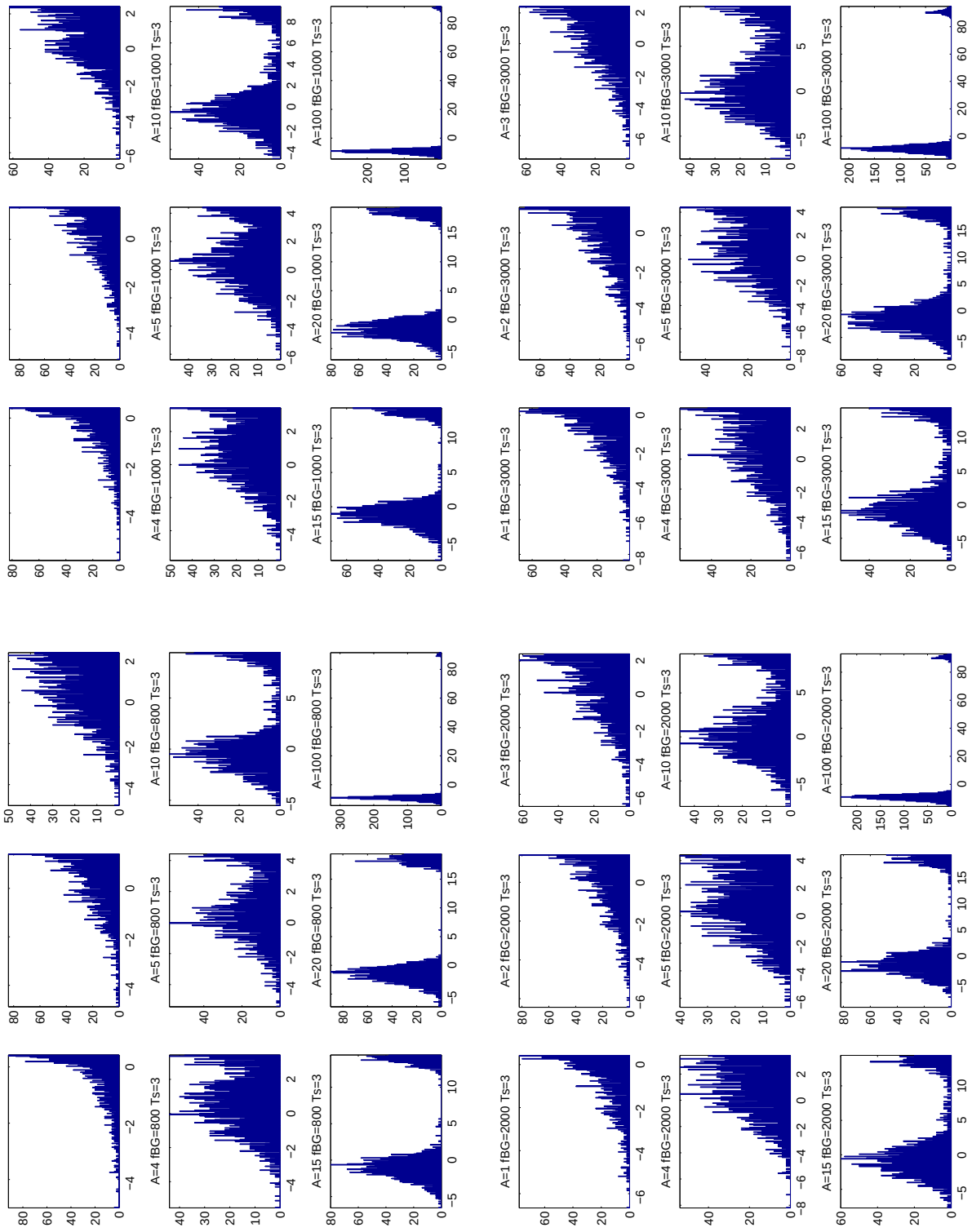

Figure B.29: Histograms of $\Delta A = A_{sim} - A_{rec}$ for 10 bits and 3 ns sampling. NSB frequency $f_{BG} = 800$ to 3000 MHz.

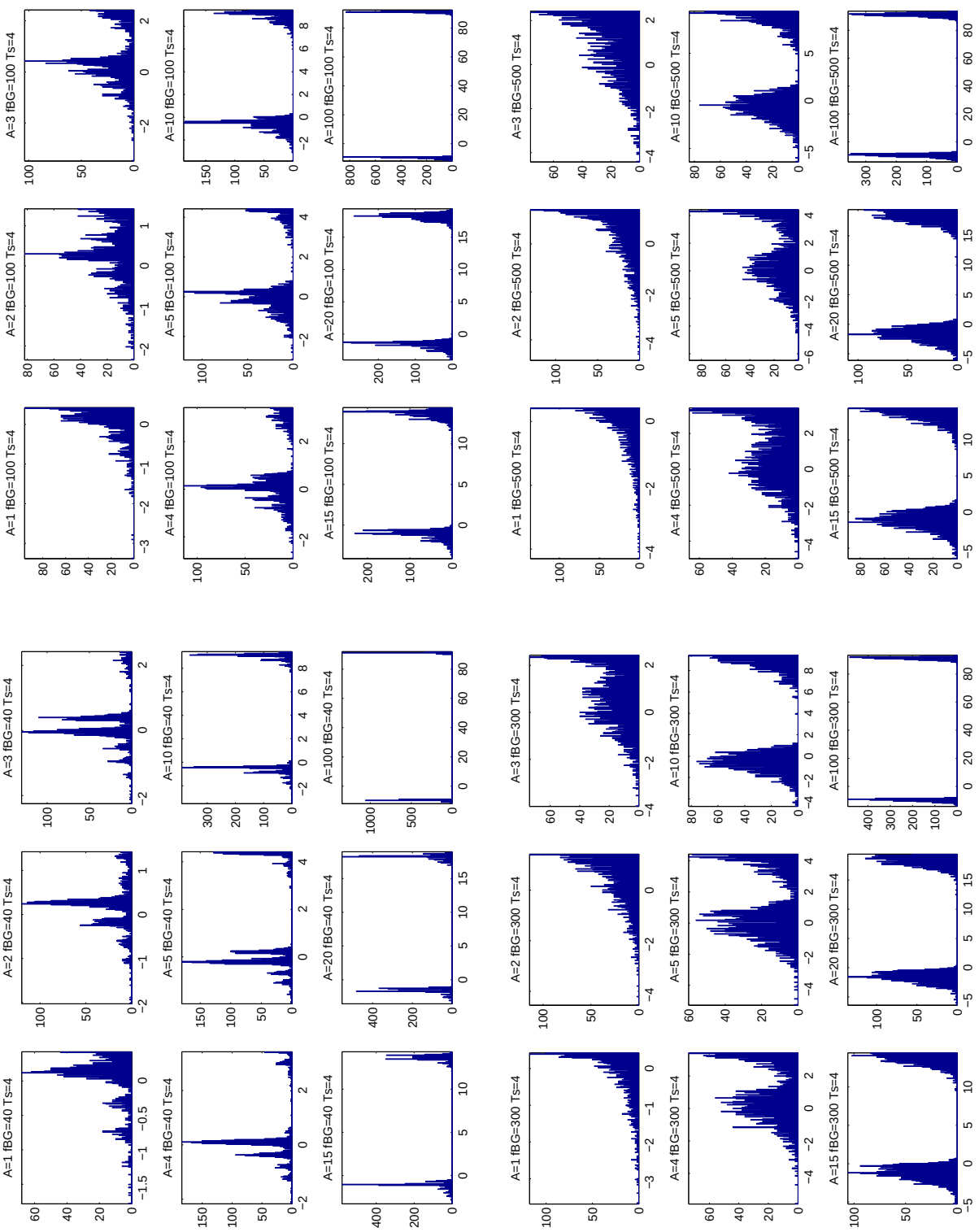

Figure B.30: Histograms of $\Delta A = A_{sim} - A_{rec}$ for 10 bits and 4 ns sampling. NSB frequency $f_{BG} = 40$ to 500 MHz.

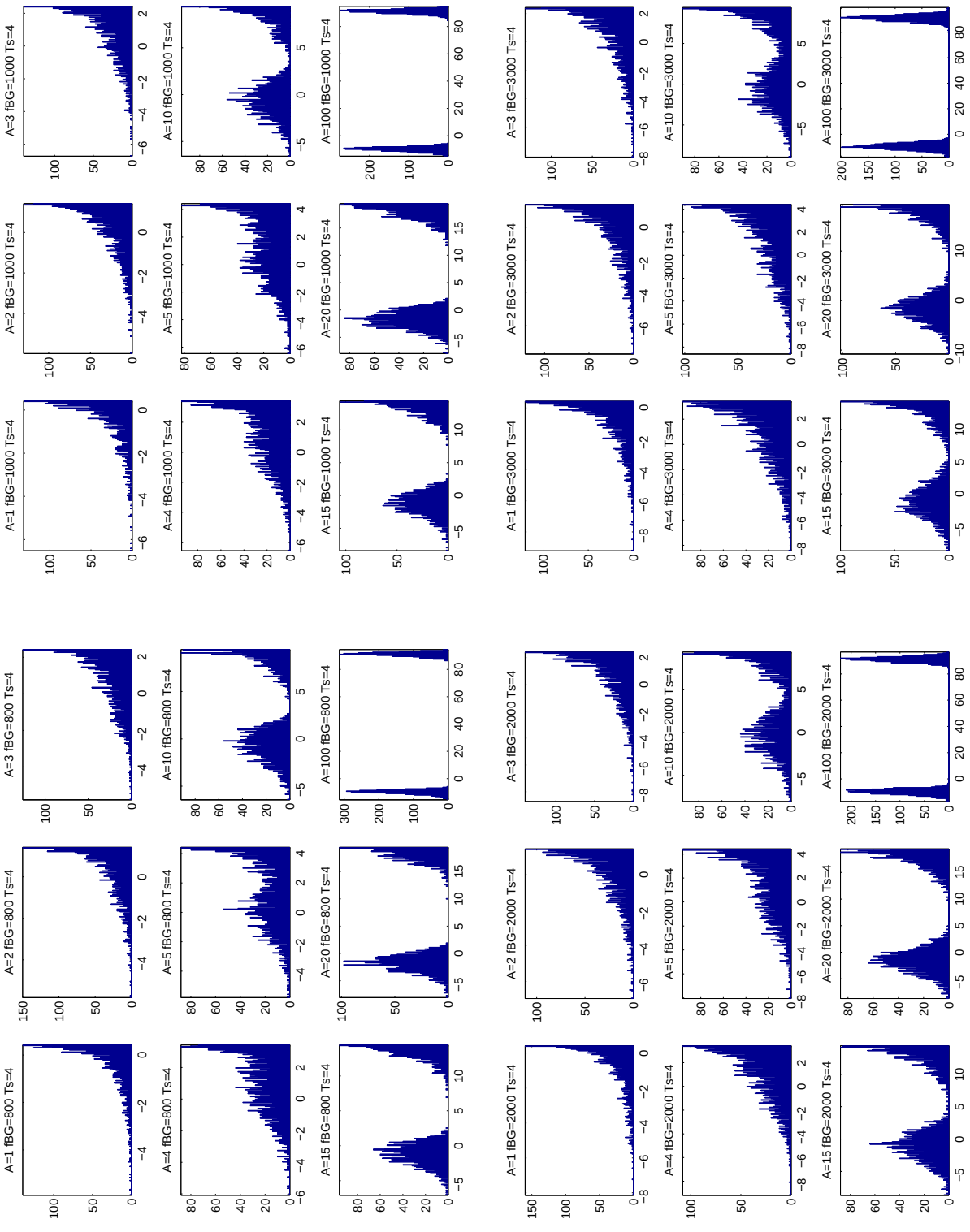

Figure B.31: Histograms of $\Delta A = A_{sim} - A_{rec}$ for 10 bits and 4 ns sampling. NSB frequency $f_{BG} = 800$ to 3000 MHz.

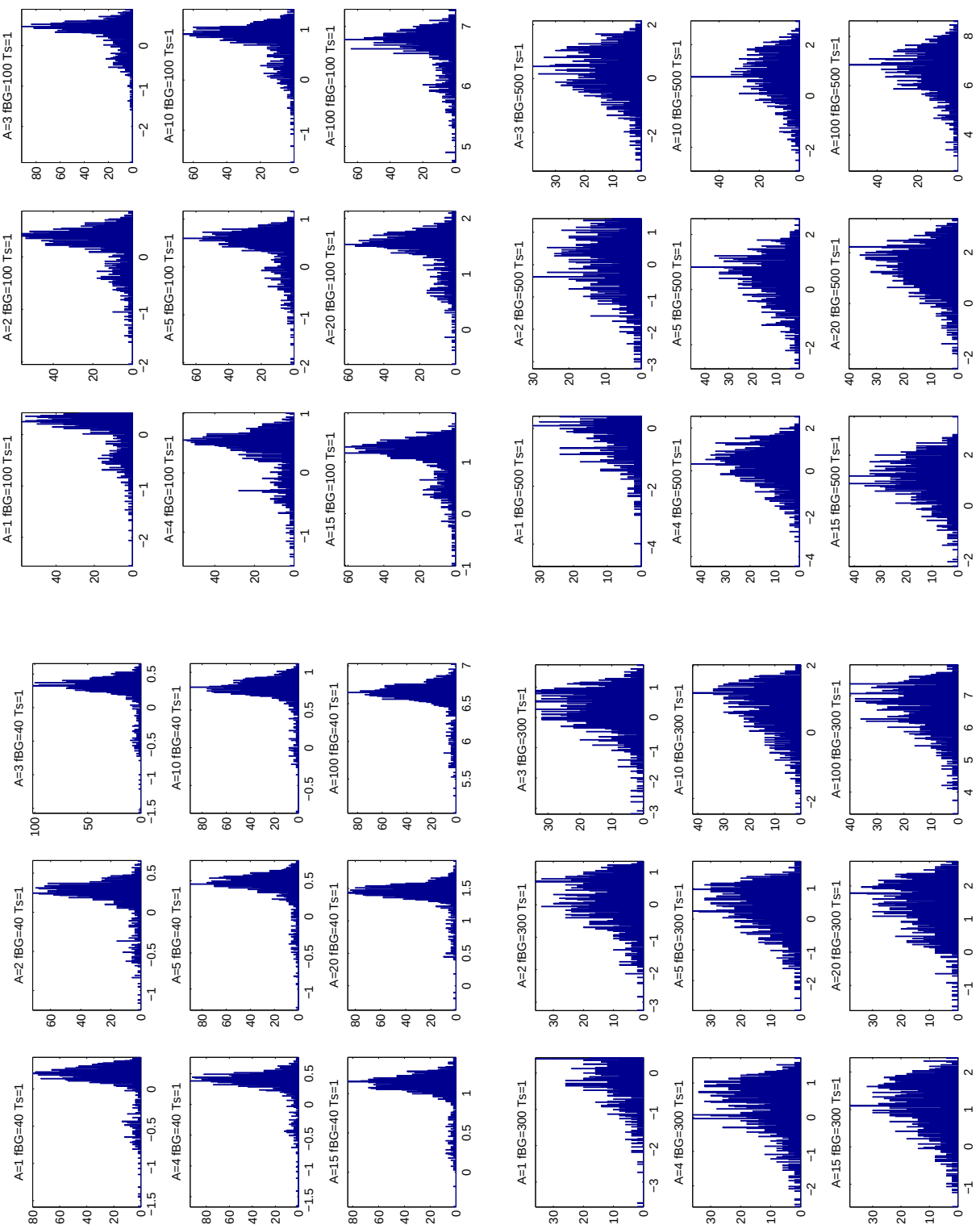

Figure B.32: Histograms of $\Delta A = A_{sim} - A_{rec}$ for 12 bits and 1 ns sampling. NSB frequency $f_{BG} = 40$ to 500 MHz.

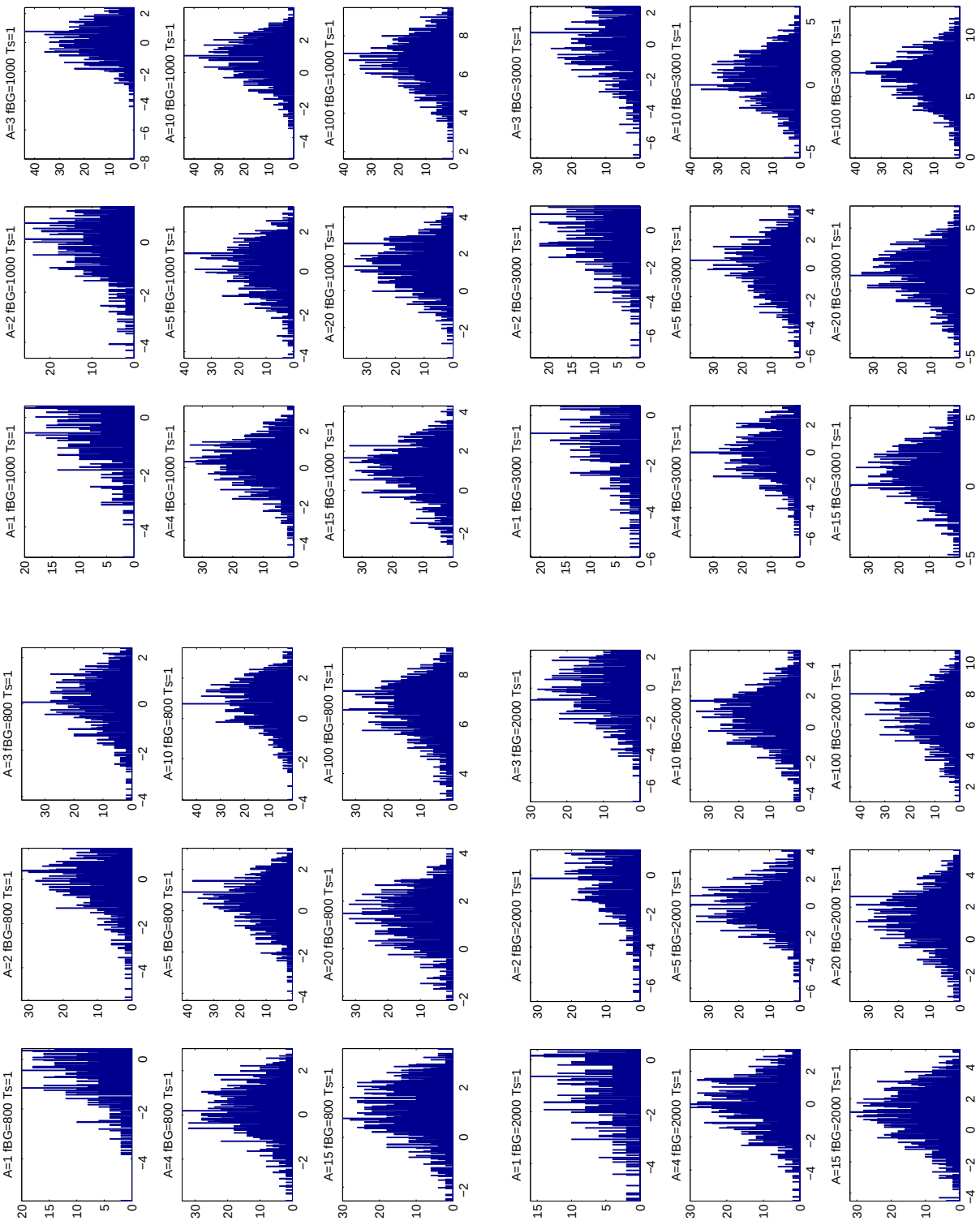

Figure B.33: Histograms of $\Delta A = A_{sim} - A_{rec}$ for 12 bits and 1 ns sampling. NSB frequency $f_{BG} = 800$ to 3000 MHz.

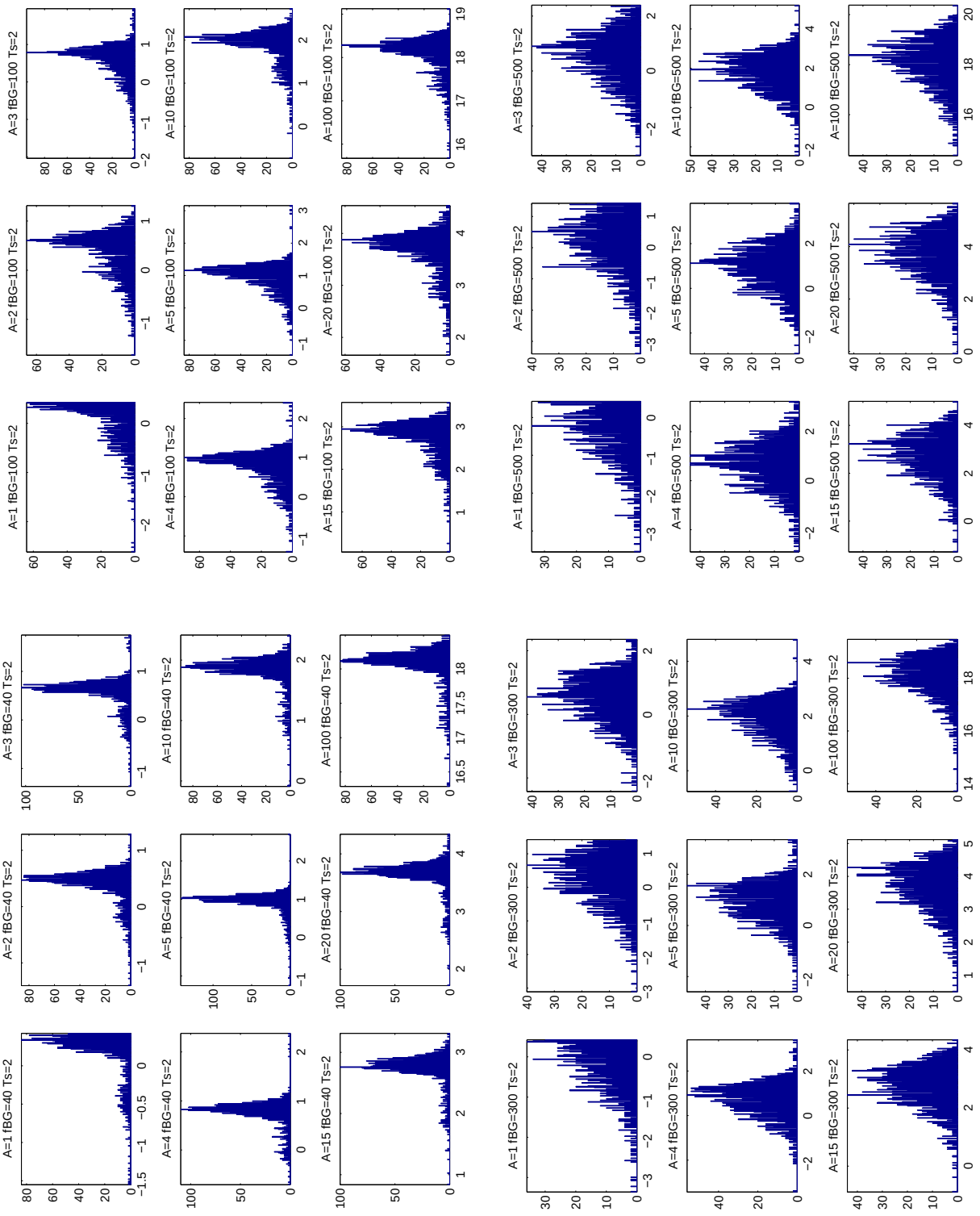

Figure B.34: Histograms of $\Delta A = A_{sim} - A_{rec}$ for 12 bits and 2 ns sampling. NSB frequency f_{BG} = 40 to 500 MHz.

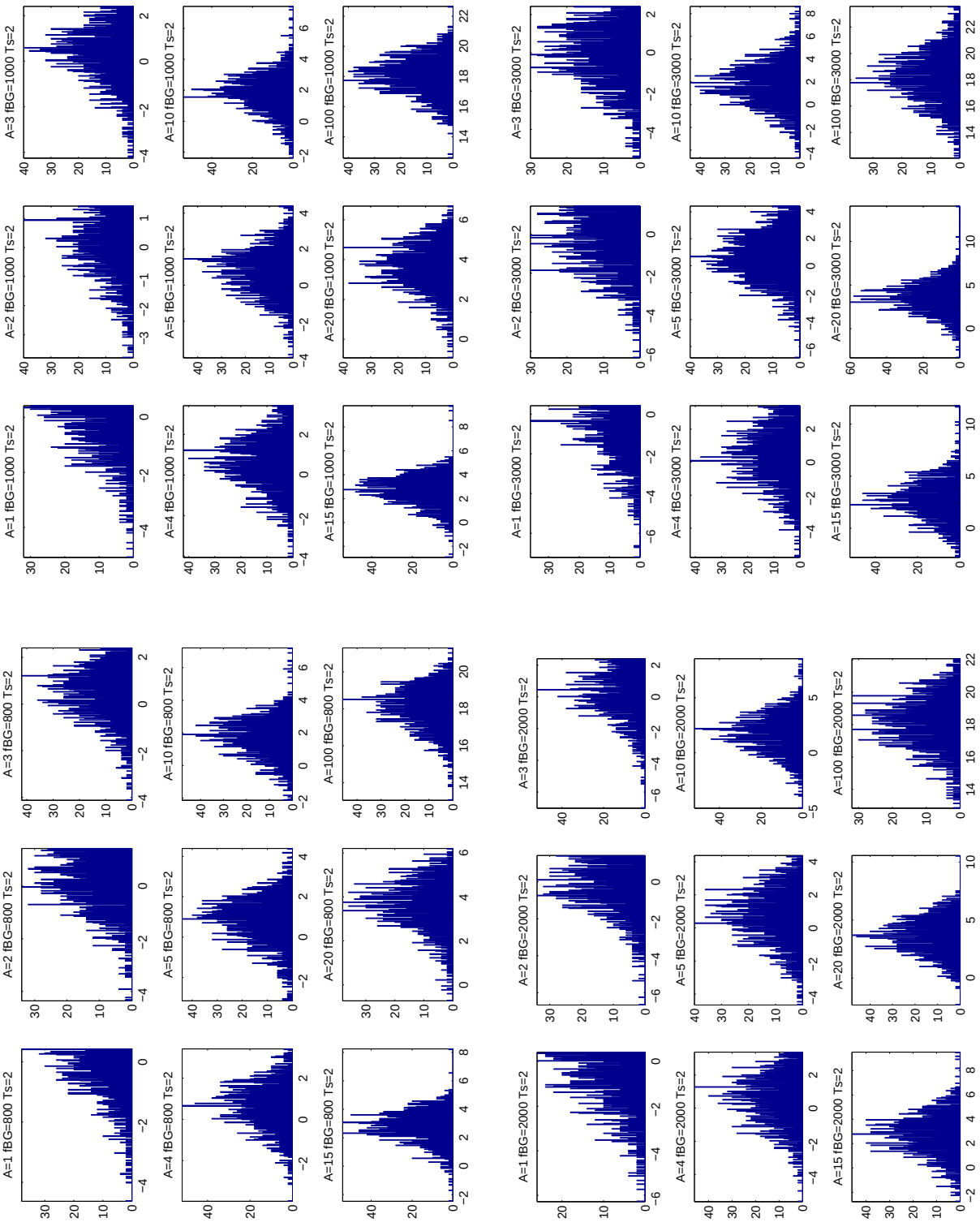

Figure B.35: Histograms of $\Delta A = A_{sim} - A_{rec}$ for 12 bits and 2 ns sampling. NSB frequency $f_{BG} = 800$ to 3000 MHz.

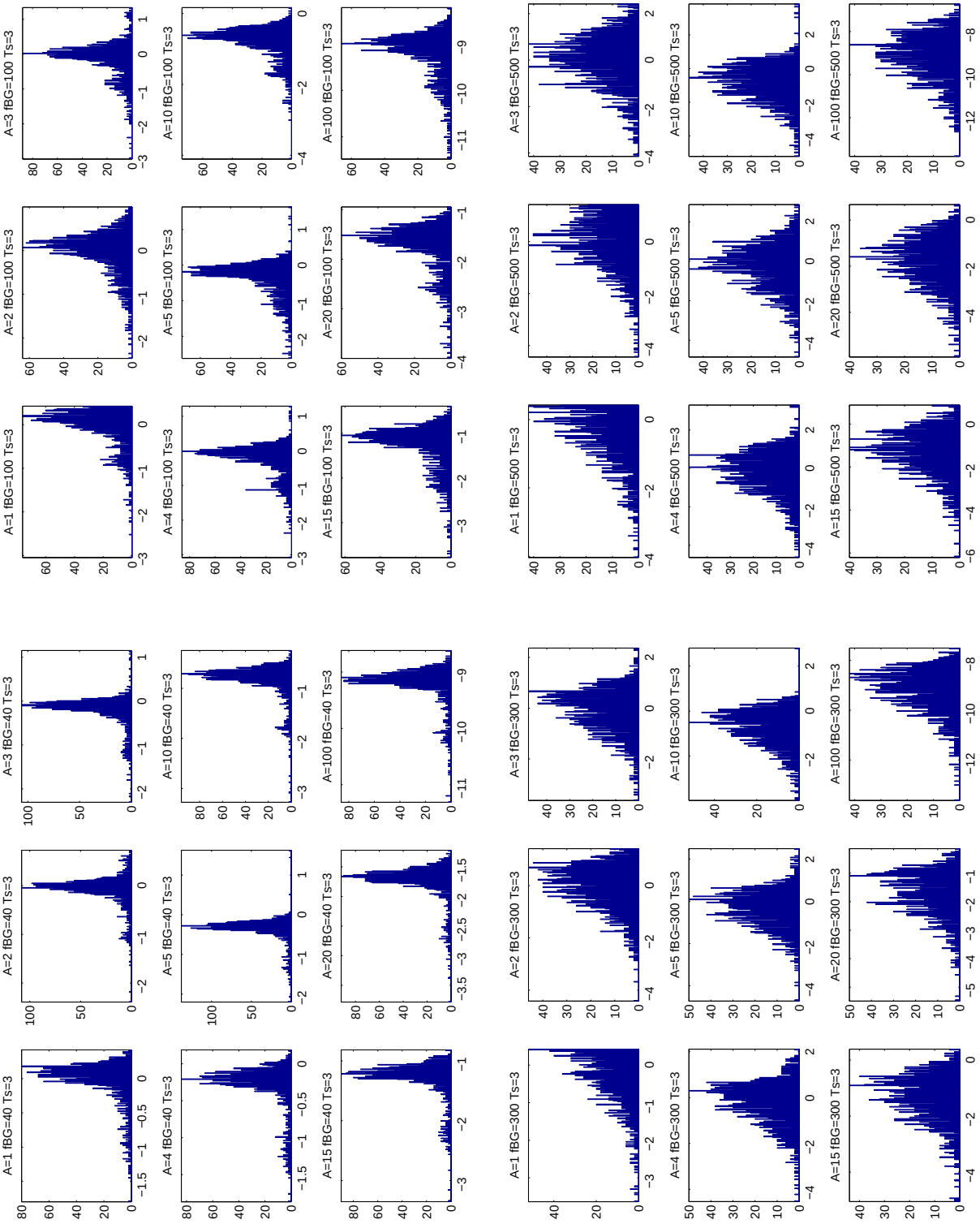

Figure B.36: Histograms of $\Delta A = A_{sim} - A_{rec}$ for 12 bits and 3 ns sampling. NSB frequency $f_{BG} = 40$ to 500 MHz.

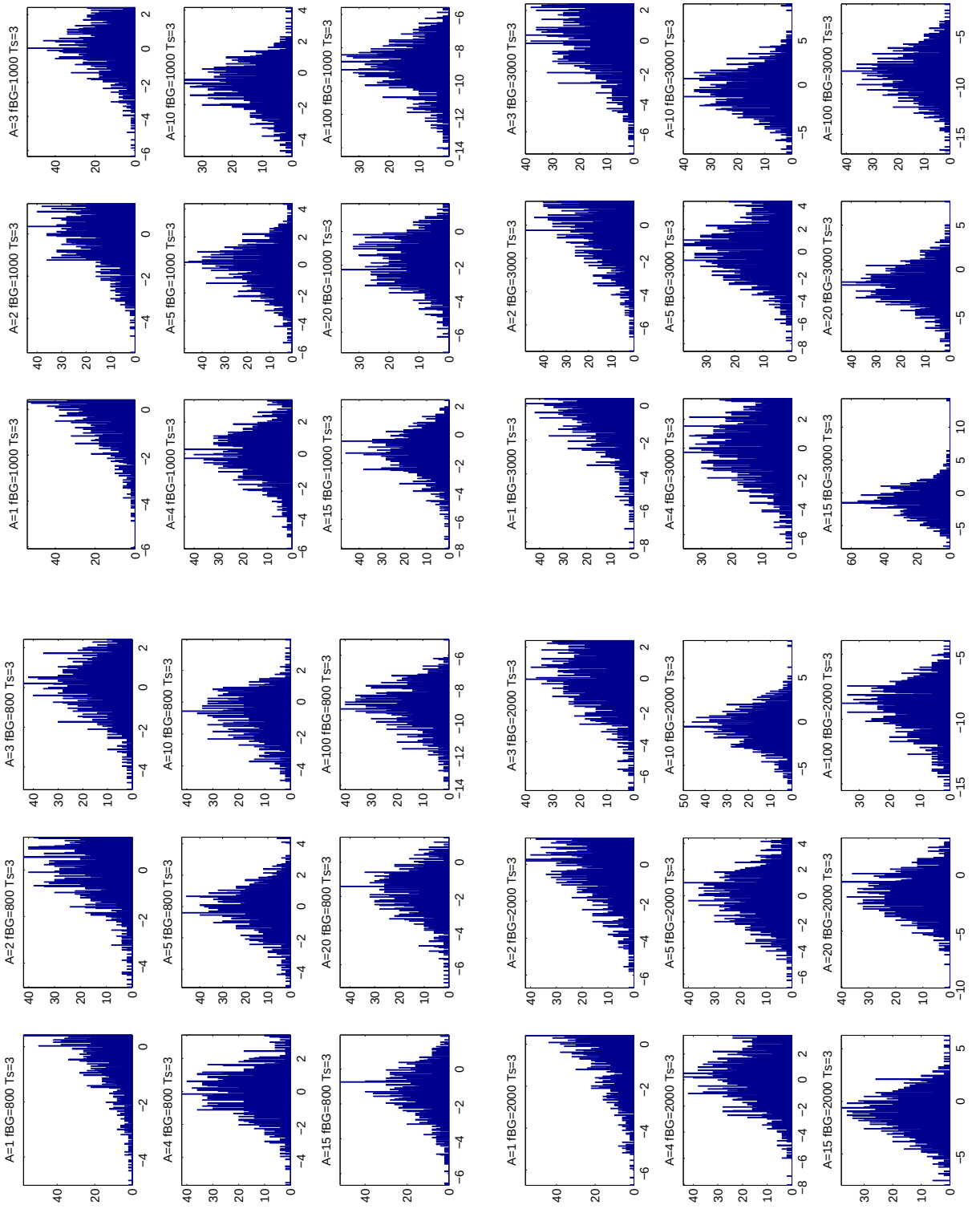

Figure B.37: Histograms of $\Delta A = A_{sim} - A_{rec}$ for 12 bits and 3 ns sampling. NSB frequency $f_{BG} = 800$ to 3000 MHz.

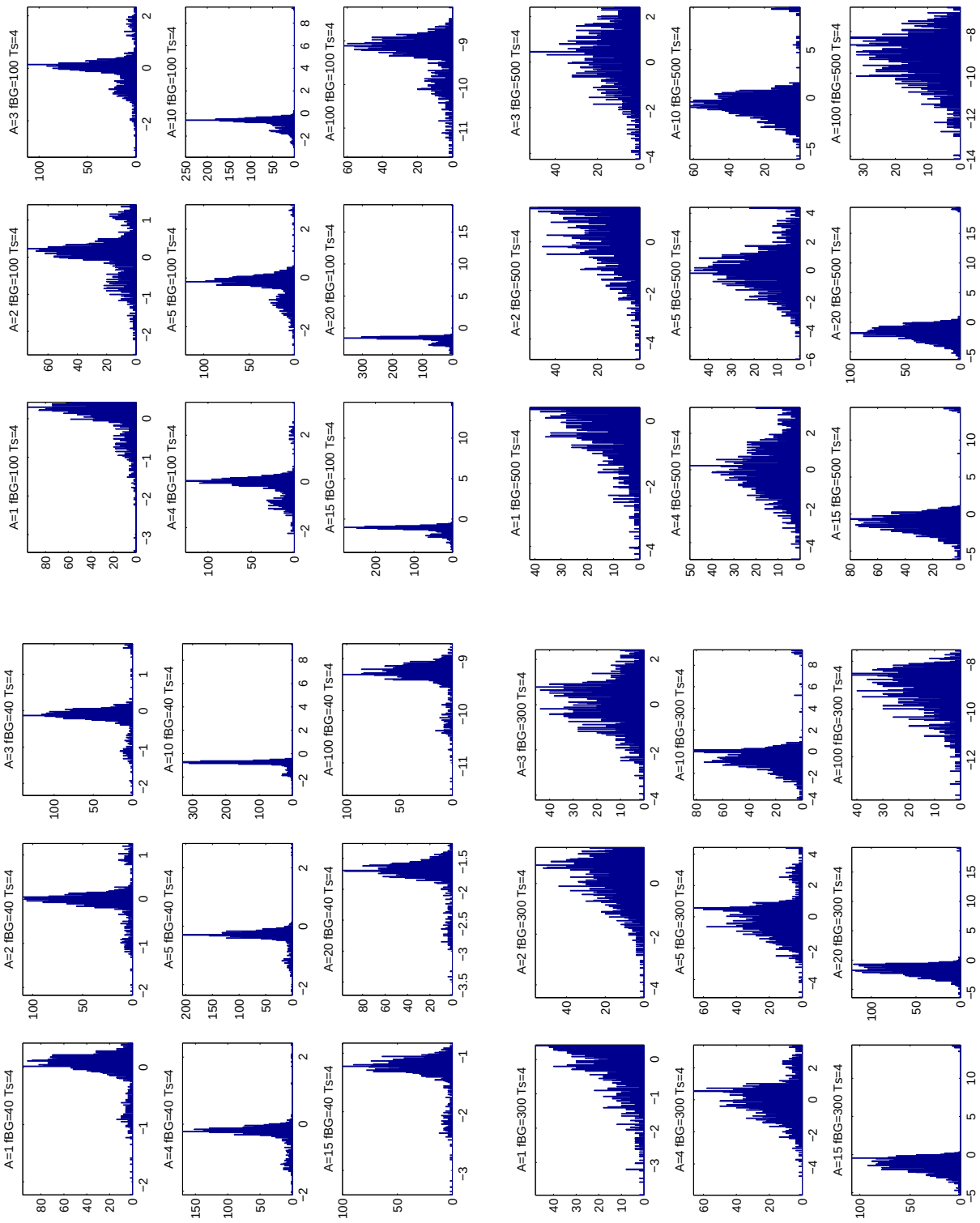

Figure B.38: Histograms of $\Delta A = A_{sim} - A_{rec}$ for 12 bits and 3 ns sampling. NSB frequency $f_{BG} = 40$ to 500 MHz.

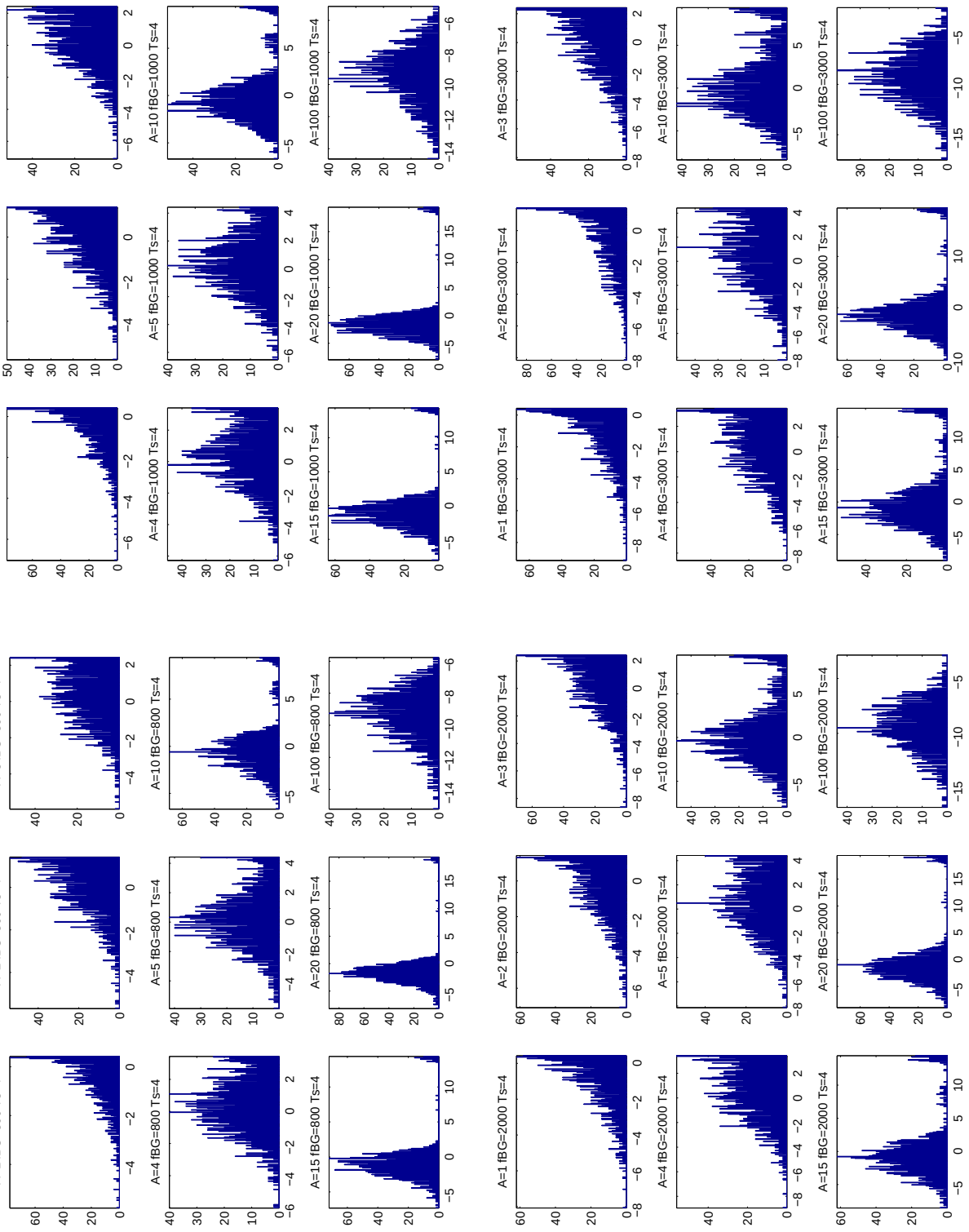

Figure B.39: Histograms of $\Delta A = A_{sim} - A_{rec}$ for 12 bits and 4 ns sampling. NSB frequency $f_{BG} = 800$ to 3000 MHz.

B.4 Amplitude difference $\Delta A = A_{sim} - A_{rec}$ vs. NSB frequency

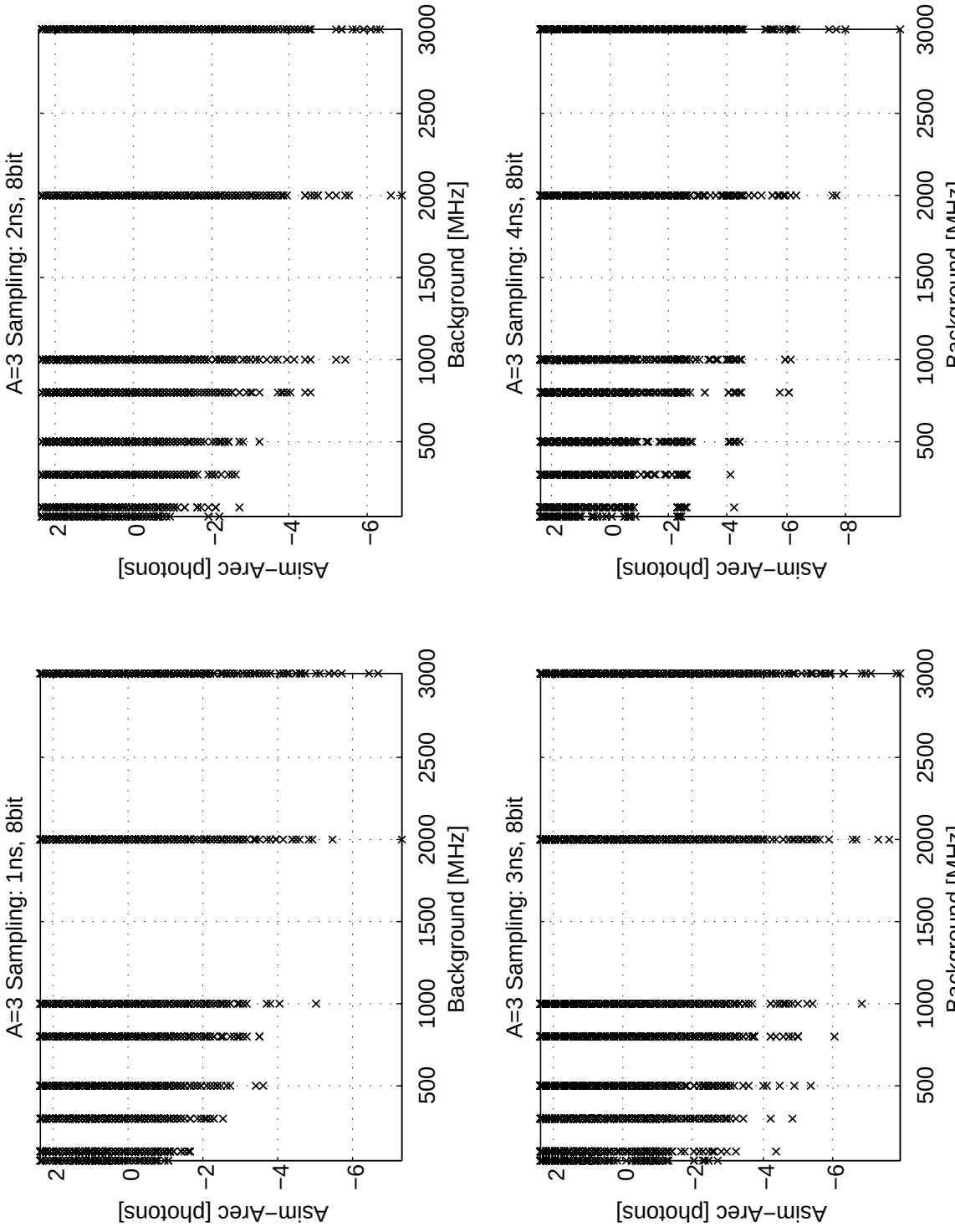

Figure B.40: Amplitude difference $\Delta A = A_{sim} - A_{rec}$ vs. NSB frequency for 8bit resolution and fixed $A_{sim} = 3$ photons and varying sampling time (1-4ns).

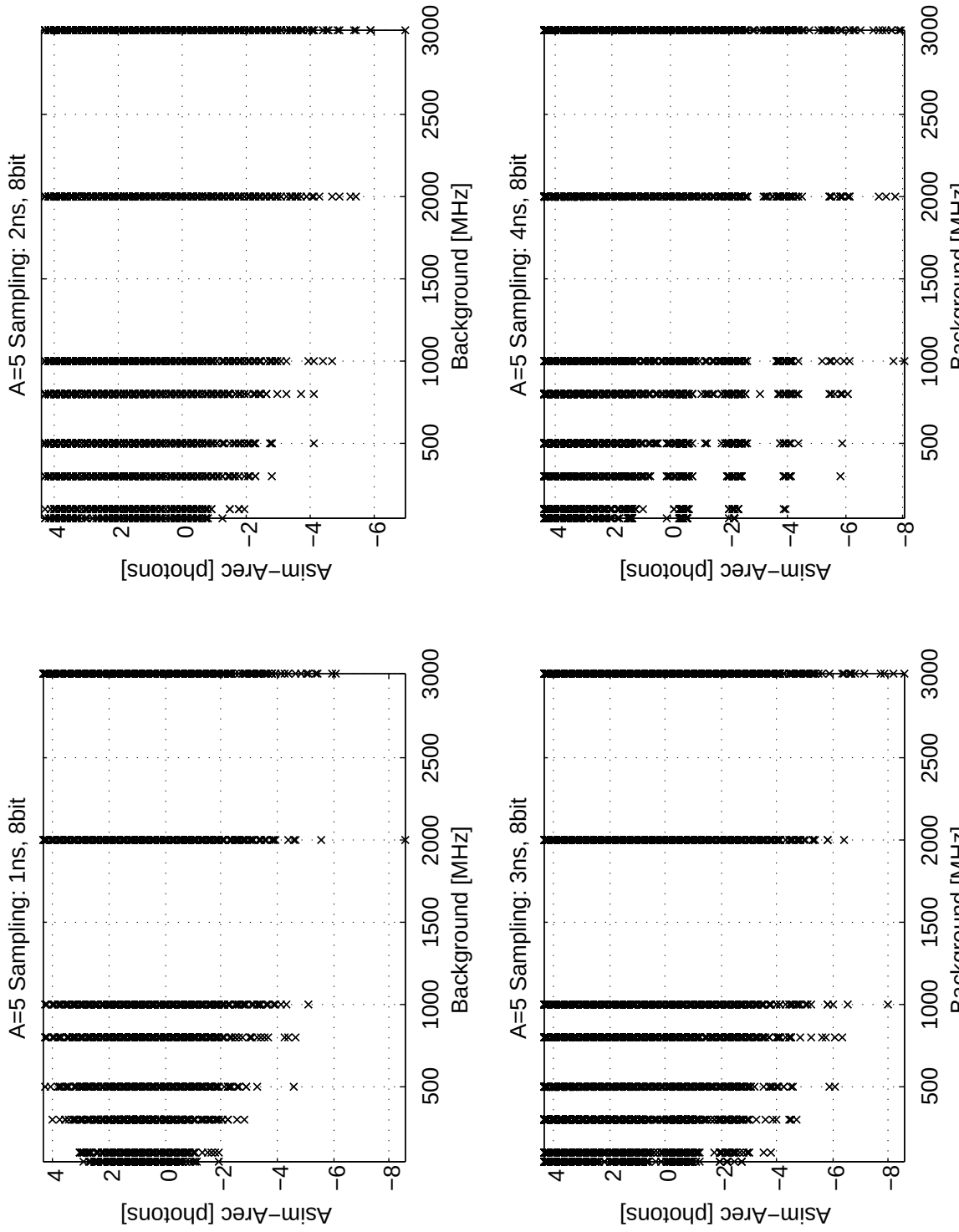

Figure B.41: Amplitude difference $\Delta A = A_{sim} - A_{rec}$ vs. NSB frequency for 8bit resolution and fixed $A_{sim} = 5$ photons and varying sampling time (1-4ns).

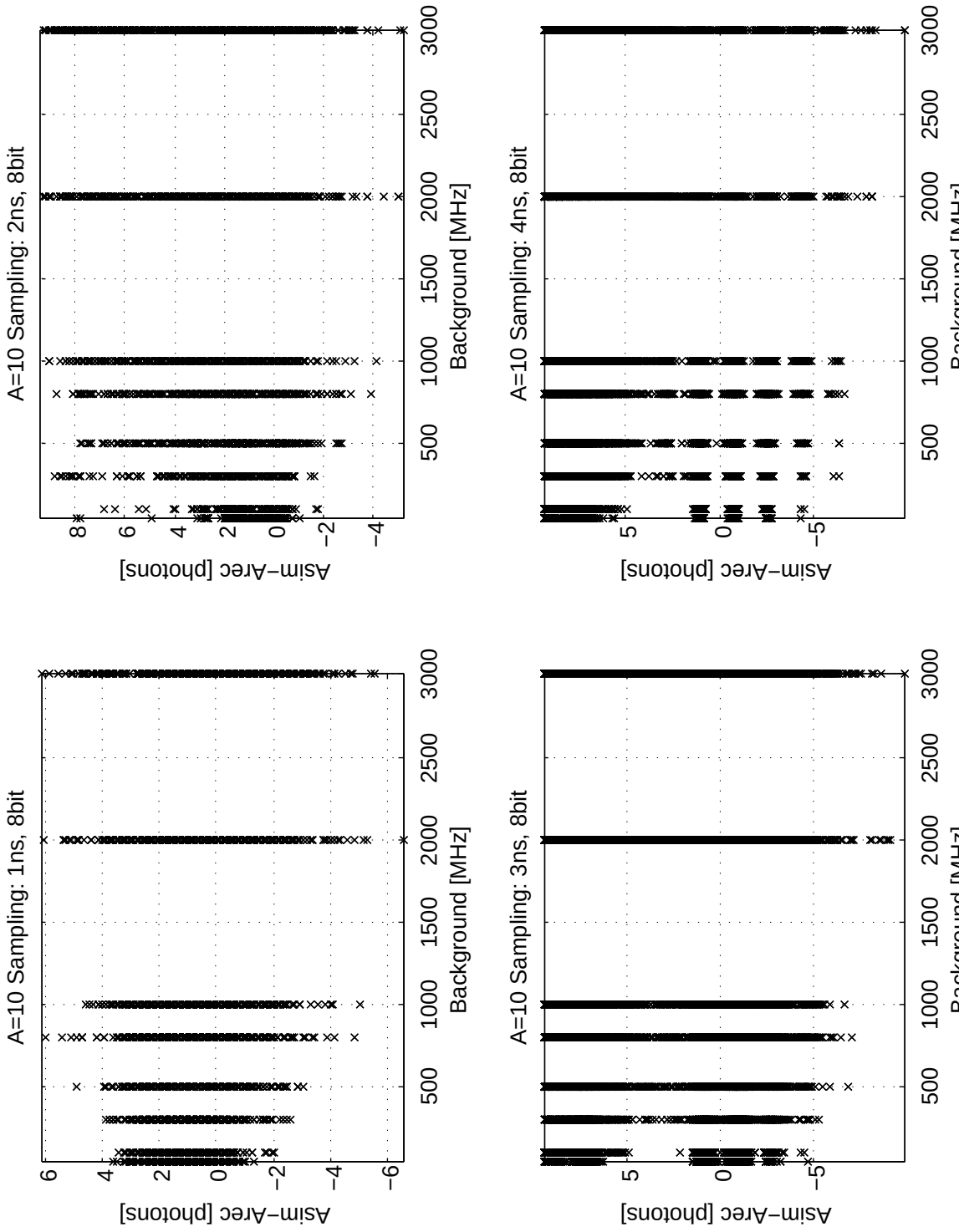

Figure B.42: Amplitude difference $\Delta A = A_{sim} - A_{rec}$ vs. NSB frequency for 8bit resolution and fixed $A_{sim} = 10$ photons and varying sampling time (1-4ns).

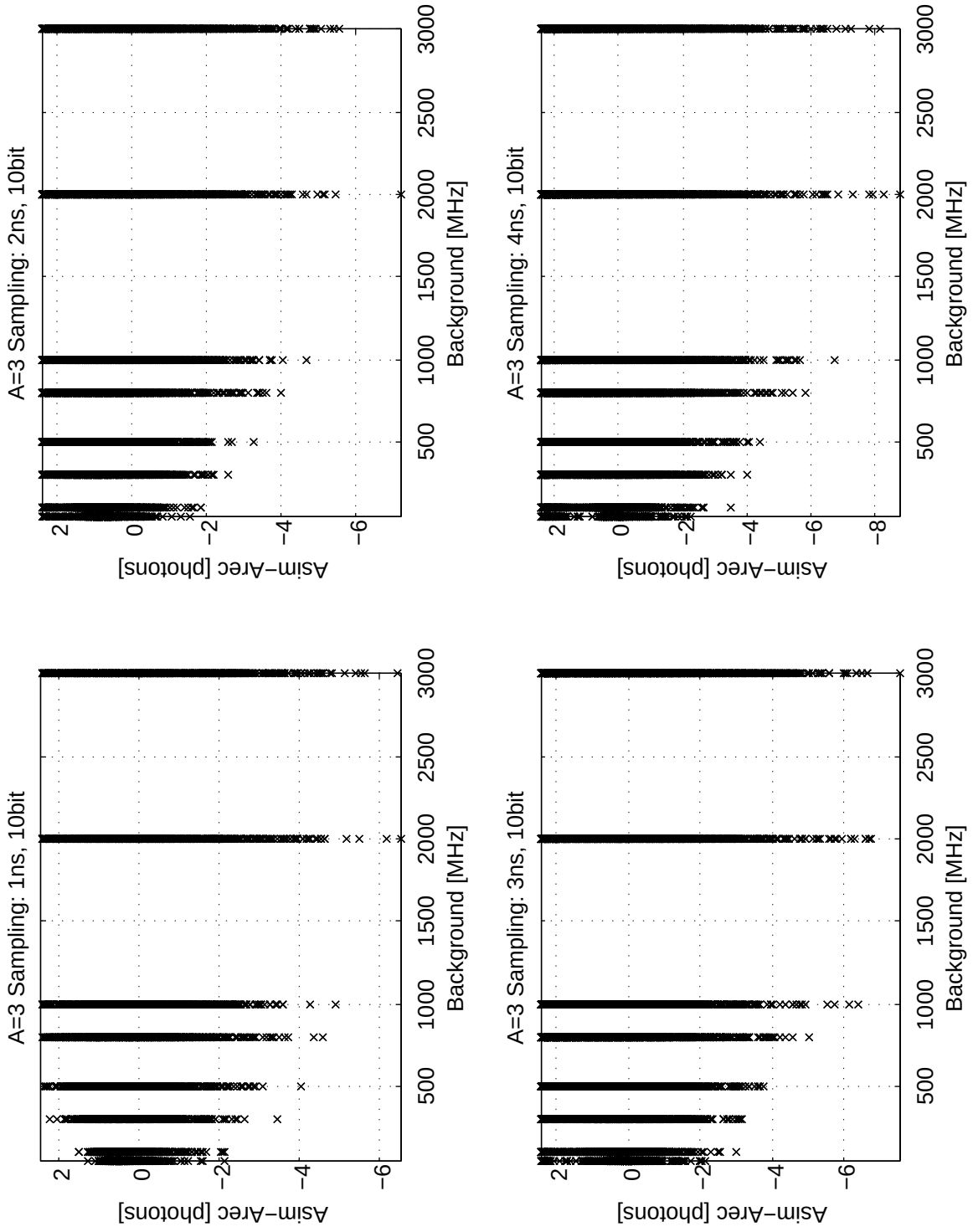

Figure B.43: Amplitude difference $\Delta A = A_{sim} - A_{rec}$ vs. NSB frequency for 10bit resolution and fixed $A_{sim} = 3$ photons and varying sampling time (1-4ns).

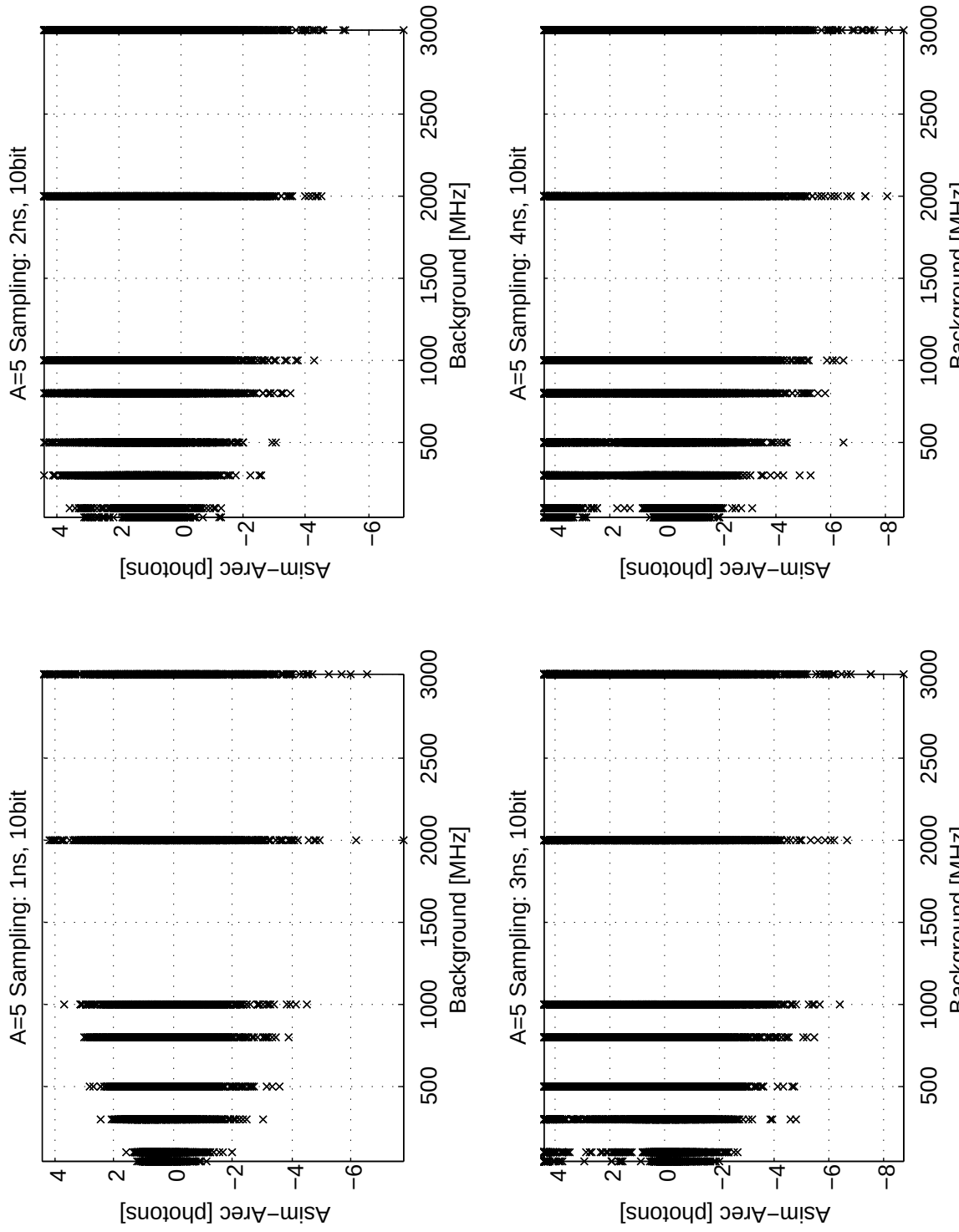

Figure B.44: Amplitude difference $\Delta A = A_{sim} - A_{rec}$ vs. NSB frequency for 10bit resolution and fixed $A_{sim} = 5$ photons and varying sampling time (1-4ns).

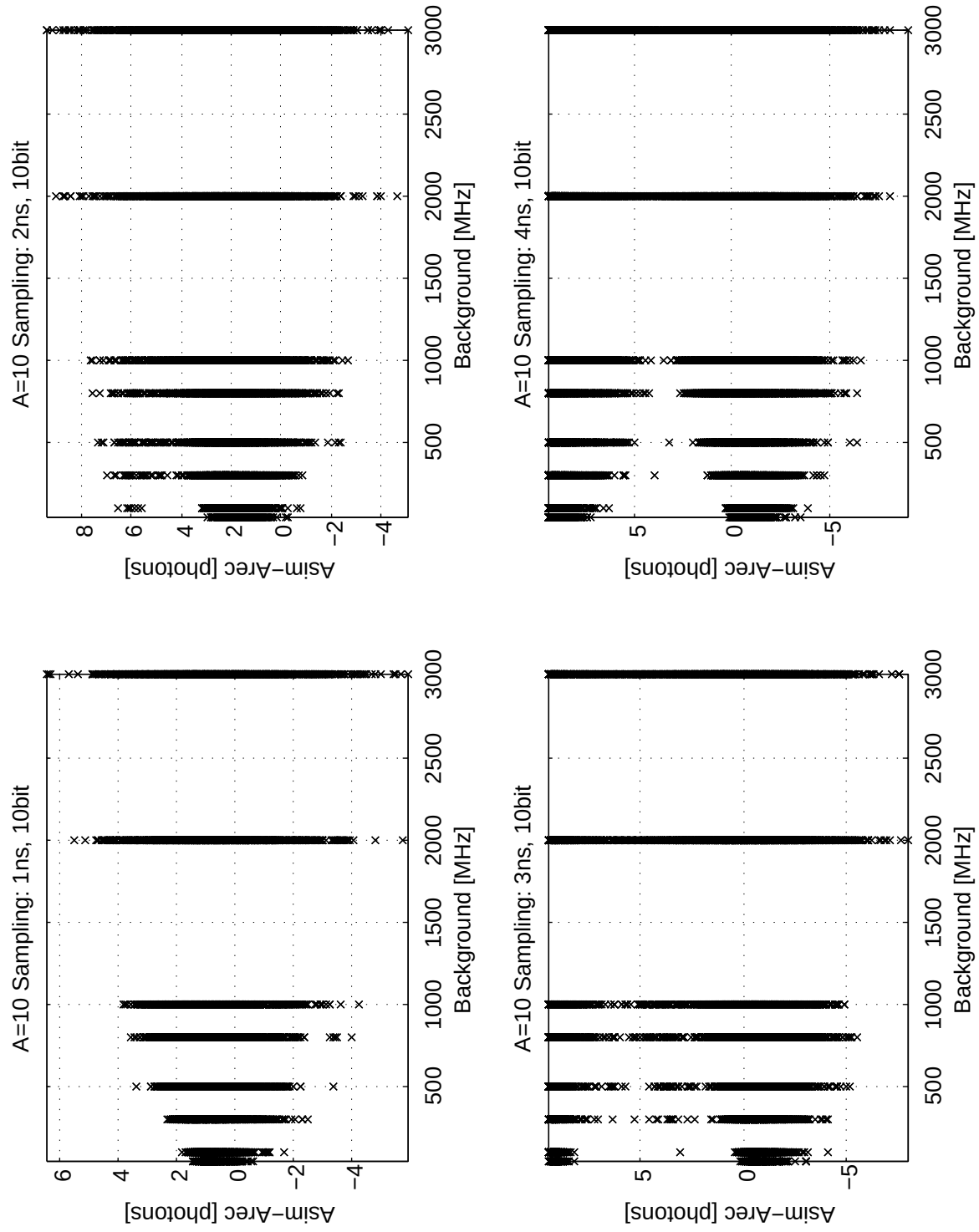

Figure B.45: Amplitude difference $\Delta A = A_{sim} - A_{rec}$ vs. NSB frequency for 10bit resolution and fixed $A_{sim} = 10$ photons and varying sampling time (1-4ns).

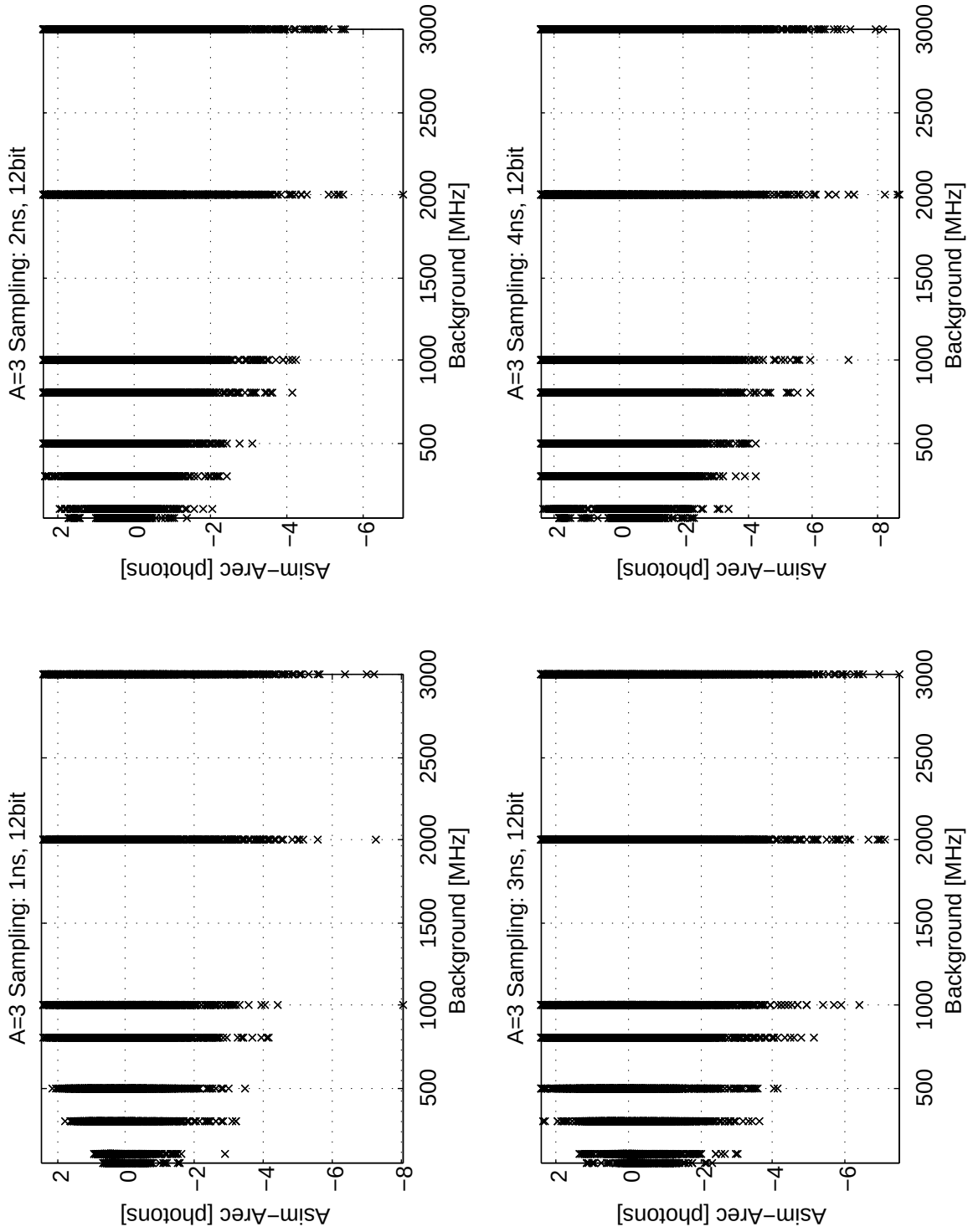

Figure B.46: Amplitude difference $\Delta A = A_{sim} - A_{rec}$ vs. NSB frequency for 12bit resolution and fixed $A_{sim} = 3$ photons and varying sampling time (1-4ns).

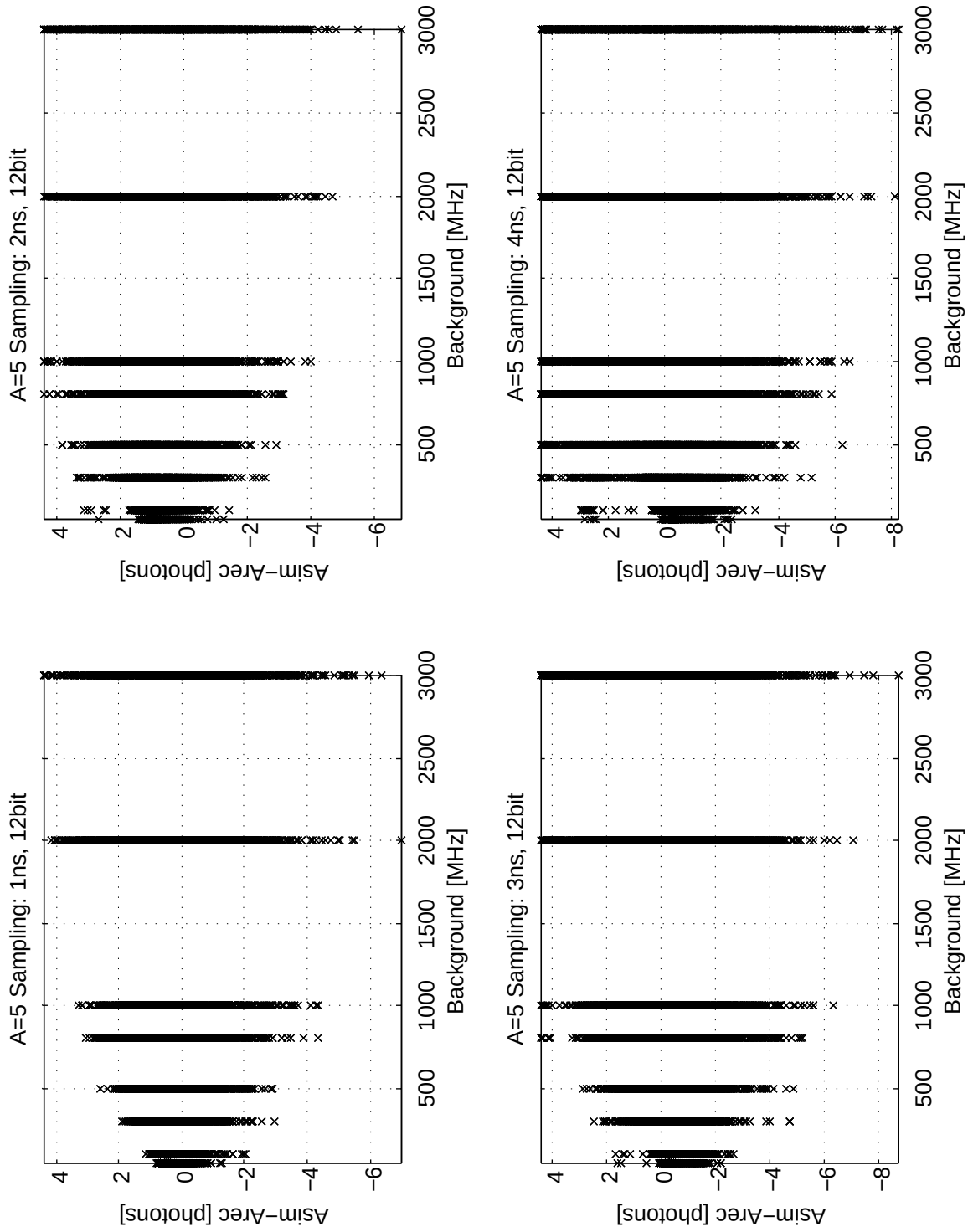

Figure B.47: Amplitude difference $\Delta A = A_{sim} - A_{rec}$ vs. NSB frequency for 12bit resolution and fixed $A_{sim} = 5$ photons and varying sampling time (1-4ns).

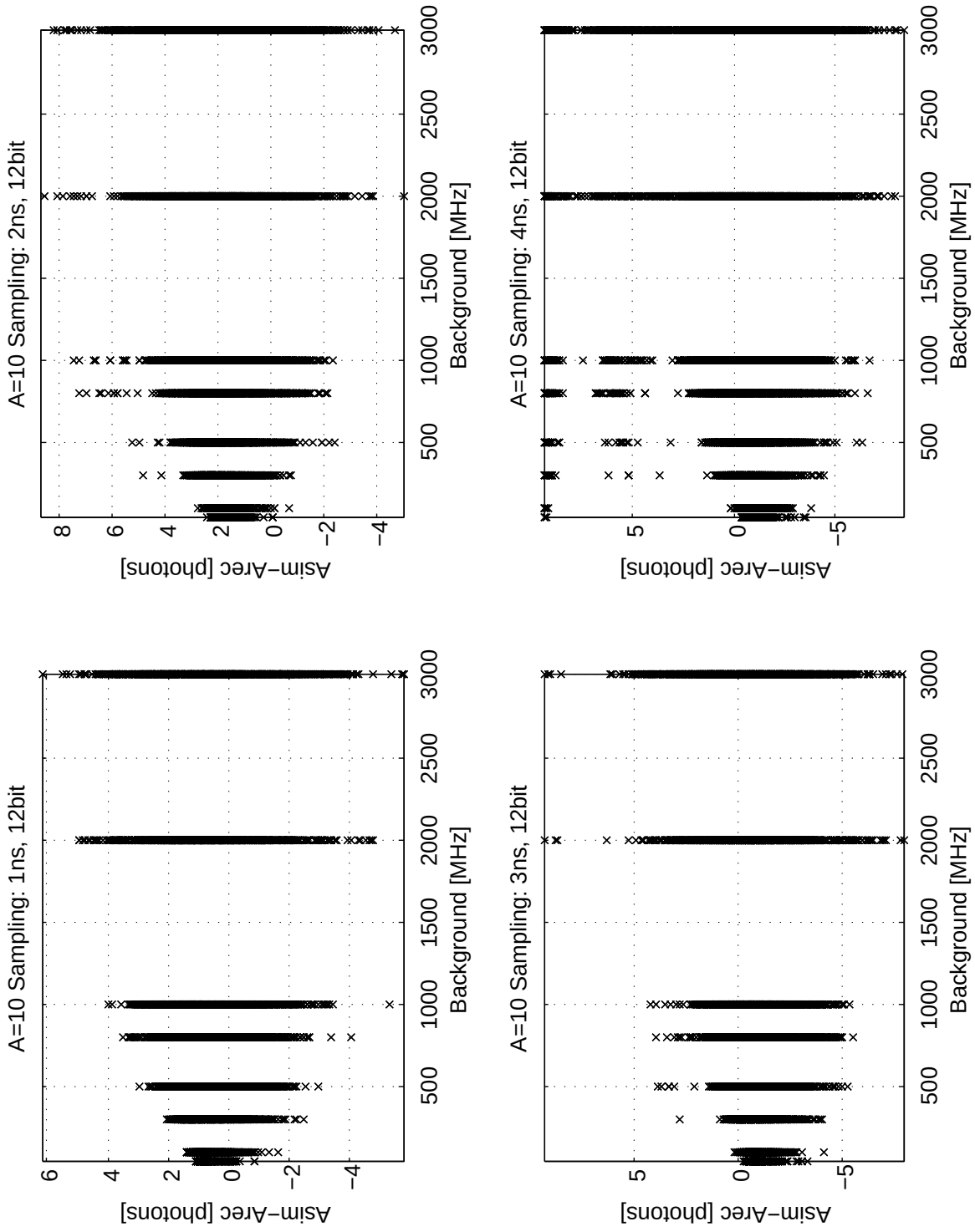

Figure B.48: Amplitude difference $\Delta A = A_{sim} - A_{rec}$ vs. NSB frequency for 12bit resolution and fixed $A_{sim} = 10$ photons and varying sampling time (1-4ns).

Bibliography

[1] CTA Paper of Swiss participation (ETH, PSI, Uni Genf). The Cherenkov Telescope Array Swiss participation and perspectives.

[2] CTA homepage. www.cta-observatory.org

[3] MAGIC telescope. wwwmagic.mppmu.mpg.de

[4] H.E.S.S. telescope. http://www.mpi-hd.mpg.de/hfm/HESS/

[5] CANGAROO telescope. http://icrhp9.icrr.u-tokyo.ac.jp/

[6] VERITAS telescope. http://veritas.sao.arizona.edu/

[7] Diego Tescaro. 2007, Timing analysis of the MAGIC telescope data after installation of the ultra-fast 2 GSamples/s FADC readout.

[8] Aharonian et al. Astronomy and Astrophysics 330, 351, 362, 417, 432, 437, 449 (2004-2006).

[9] T. C. Weekes. 2003, Very high energy gamma-ray astronomy, Institute of Physiscs Publishing Bristol and Philadelphia, ISBN: 0-7503-0658-0.

[10] Nicoleta Dinu. 01.12.2006, Presentation: Characteristics of the Silicon Photo Multiplier (SiPM) detectors, LPC - Clermont Ferrand
http://clrwww.in2p3.fr/semi/2006/sources/20061201.pdf

[11] Claudio Piemonte et al. 2007, Characterization of the First Prototypes of Silicon Photomultiplier Fabricated at ITC-irst, IEEE TRANSACTIONS ON NUCLEAR SCIENCE, VOL. 54, NO. 1, FEBRUARY 2007

[12] Claudio Piemonte. 2006, A new Silicon Photomultiplier structure for blue light detection, Nuclear Instruments and Methods in Physics Research A 568 (2006) 224-232

[13] W.T.Welford and R.Winston. 1989, The Optics of Nonimaging Concentrators. Academic Press.

[14] LASER COMPONENTS. Blue laser diode type LCS406020M5X, http://www.lasercomponents.com

[15] IC Haus. Blue laser diode driver iC-HKB, www.ichaus.de

[16] Photonique SA. GAPD preamplifier AMP_0611, http://www.photonique.ch/

[17] Hamamatsu. 2008, Datasheet of MPPC S10362-33-100C, mppc_kapd0002e03_datasheet.pdf, www.hamamatsu.com

[18] MATLAB from MathWorks. http://www.mathworks.com/

[19] G.W. Phillips. Nucl. Instrum. Methods 153 (1978), 449.

[20] http://ihp-pw1.ethz.ch/ibraun/.CT3/talks/WinstonCones4.pdf